Design, Packaging, and Reliability
of MEMS S&A Components and Systems

Submitted by

Dr. SB Park, Assistant Professor, Mechanical Engineering Department, SUNY
    Binghamton
Dr. Bahgat Sammakia, Professor and Director of IEEC, SUNY Binghamton

Dr. James Pitarresi, Professor, Mechanical Engineering Department, SUNY
    Binghamton

December 26, 2006

Contact:

SB Park
Assistant Professor
Mechanical Engineering Department
State University of New York at Binghamton
Email: sbpark@binghamton.edu, Phone: 607-777-3415

20070111112

REPORT DOCUMENTATION PAGE

Public reporting burden for this collection of information is estimated to average 1 hour per response, including the time for reviewing instructions, searching existing data sources, gathering and maintaining the data needed, and completing and reviewing this collection of information. Send comments regarding this burden estimate or any other aspect of this collection of information, including suggestions for reducing this burden to Department of Defense, Washington Headquarters Services, Directorate for Information Operations and Reports (0704-0188), 1215 Jefferson Davis Highway, Suite 1204, Arlington, VA 22202-4302. Respondents should be aware that notwithstanding any other provision of law, no person shall be subject to any penalty for failing to comply with a collection of information if it does not display a currently valid OMB control number. **PLEASE DO NOT RETURN YOUR FORM TO THE ABOVE ADDRESS.**

1. REPORT DATE *(DD-MM-YYYY)*	2. REPORT TYPE	3. DATES COVERED *(From - To)*
26-Dec-2006	Final Progress	-1-May-2005 - 30-Sept-2006

4. TITLE AND SUBTITLE
Design, Packaging and Reliability of MEMS S&A Components and

5a. CONTRACT NUMBER

5b. GRANT NUMBER
N00014-05-1-0688

5c. PROGRAM ELEMENT NUMBER

6. AUTHOR(S)
SB Park – Assistant Professor

Bahgat Sammakia -Professor

James Pitarresi - Professor

5d. PROJECT NUMBER

5e. TASK NUMBER

5f. WORK UNIT NUMBER

7. PERFORMING ORGANIZATION NAME(S) AND ADDRESS(ES)

The Research Foundation of
SUNY at Binghamton
P.O. Box 6000
Binghamton, New York 13902

8. PERFORMING ORGANIZATION REPORT NUMBER

9. SPONSORING / MONITORING AGENCY NAME(S) AND ADDRESS(ES)

Office of Naval Research
Ballston Centre Tower One
800 North Quincy Street
Arlington , VA 22217-5660

Office of Naval Research Boston
295 Summer Street Room 627
Boston, MA 02210-2109

10. SPONSOR/MONITOR'S ACRONYM(S)

11. SPONSOR/MONITOR'S REPORT NUMBER(S)

12. DISTRIBUTION / AVAILABILITY STATEMENT

13. SUPPLEMENTARY NOTES

14. ABSTRACT
Technology refinements to the packaging process, as well as assuring the highest possible yield of serviceable F/S&A systems, are specifically addressed. The primary objective of this research project is to provide a basic physics based understanding of the behavior and performance of Safe and Arm (S& A) systems. The research covers a broad range of activities ranging from basic materials characterization to overall system level models. The research is conducted as a collaborative effort between Binghamton University, (BU), the Bennington Micro technology Center (BMC), and the Indian Head Division of the Naval Surface Warfare (IHDIV). BU focused on applied research related to the materials properties, the mechanical and thermal behavior of the system and the overall system performance and reliability under field conditions. BMC focused on process and manufacturing issues and help with the implementation of design changes and the exploration of additional applications.

15. SUBJECT TERMS

16. SECURITY CLASSIFICATION OF:			17. LIMITATION OF ABSTRACT	18. NUMBER OF PAGES	19a. NAME OF RESPONSIBLE PERSON
a. REPORT	b. ABSTRACT	c. THIS PAGE			19b. TELEPHONE NUMBER *(include area code)*

Contents

Design, Packaging, and Reliability of MEMS S&A Components and Systems

Sub Task 1: Materials Characterization

Performer: Junghyun Cho, Seungbae Park, Harry Schoellor, and Jongman Kim
Organization: Dept. of Mechanical Engineering, SUNY Binghamton

1-1. Oxidation/Reduction Behavior of Pure Indium

Overview

This work focused on the study of oxidation and reduction of pure indium solder to subsequently develop a reflow processing window to be utilized in industry. Work began with a thermodynamic survey in which the Gibbs free energy of oxidation was calculated. From there, the effect of moisture and oxygen on the hydrogen reducing environment was investigated to develop an ideal processing environment.

Before beginning the oxidation experiments it was necessary to develop a polishing technique which would yield repeatable thickness measurements for ultra thin oxide layers. An electrochemical polishing approach was adopted because of its ability to produce an ultra smooth (< 10-nm roughness) finish. Spectroscopic ellipsometry was employed to measure the thickness of these ultra thin oxide layers. Ellipsometry is preferred because of its high resolution (5 angstrom) and non-destructive nature. For thicker oxide layers, measurements were estimated using dynamic nanoindentation.

To experimentally verify the theoretical thermodynamic calculations, oxide thickness verses temperature plots were constructed. From these plots several conclusions were drawn. First, there is little or no oxidation when indium is heat treated below the melting temperature. Second, based on the Arrhenius plot there is a sharp increase in the activation energy after crossing the melting temperature. Third, oxidation in inert environments seems to follow thermodynamic calculations. A cross over was seen from oxidation to reduction.

Reduction of thick indium oxide layers in a hydrogen environment seemed to be more difficult. Reduction environmental conditions close to thermodynamic equilibrium point showed very slow kinetics. Because indium oxide is so stable at high temperatures it was necessary to use extreme temperatures (350°C) to see any appreciable reduction.

From a kinetics standpoint it was seen that oxidation growth in air follows a logarithmic relationship. Indium solder heat treated at 145°C, 180°C, 220°C all showed this behavior which is based on the theory of electron flow from the metal to the oxide rather than diffusion of ions through the oxide lattice. Oxidation kinetics in an inert environment below the melting temperature showed little or no oxide growth, all falling within the range of the native oxide layer.

Complementing this oxidation and reduction study is a materials characterization of both indium and indium oxide. The mechanical properties, elastic modulus and hardness were measured using nanoindentation. Microstructure characterization was carried out using both optical microscopy and atomic force microscopy (AFM). Lastly,

X-ray diffraction (XRD) was used to verify the crystal structure of indium oxide before and after the melting temperature.

Thermodynamics

Oxidation begins when $\Delta G°$ of the reaction takes on a negative value due to the metal being unstable relative to the oxide formed at elevated temperatures. In Fig. 1-1 below it can be clearly seen that indium oxide is stable from $0°K$ to indium's boiling point ($2080°C$) meaning that indium oxide is always oxidizing at all relevant temperatures. The only way to make the oxide thermodynamically unstable is to introduce a reducing gas such as CO_2, or H_2.

To achieve thermodynamic equilibrium hydrogen gas is added to the environment until the ratio of moisture to hydrogen at a specific temperature is small enough to make $\Delta G° = 0$. Once $\Delta G°$ is zero more hydrogen is added to enter the reduction zone where the oxide is unstable relative to the metal. So it is immediately obvious that H_2O partial pressure plays a large role in determining whether an environment is reducing or oxidizing. Moisture should be reduced as much as possible and hydrogen increased to maximize the etching rate in reducing environments. It should be noted here that thermodynamics will only tell us whether the environment is reducing or oxidizing. No growth or etching rate information can be obtained from such a study.
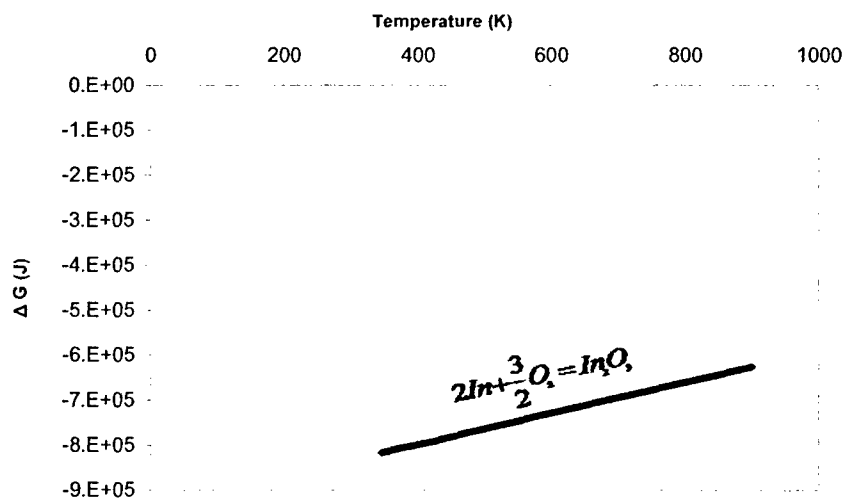
Temperature (K)

Fig. 1-1 Ellingham diagram for indium oxide, Gibbs free energy verses temperature.

The graph below (Fig. 1-2) of percent hydrogen verses temperature with moisture isobars, illustrates the effect of moisture on the thermodynamic location of the reduction zone. We can see that as the moisture content increases the reduction zone shifts further and further to the right. Therefore at higher moisture concentrations higher temperatures are needed to achieve reduction. For example at $200°C$ and 4% hydrogen, only environments with < 1ppm moisture are reducing. With 10ppm moisture and 4%

hydrogen the temperature would have to be increased to 300°C to enter the reduction zone. Since processing temperatures greater than 300°C are impractical because of component degradation, low moisture concentrations are imperative in the fluxless reflow of pure indium solder.
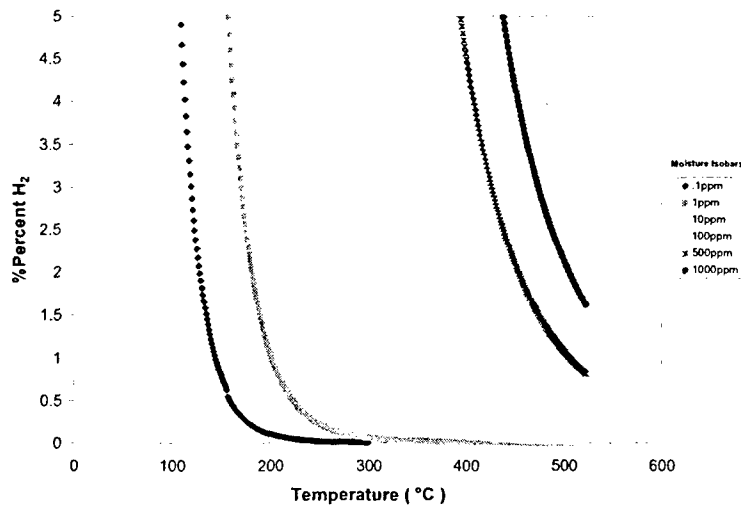

Fig. 1-2 Effect of moisture on the hydrogen reducing environment.
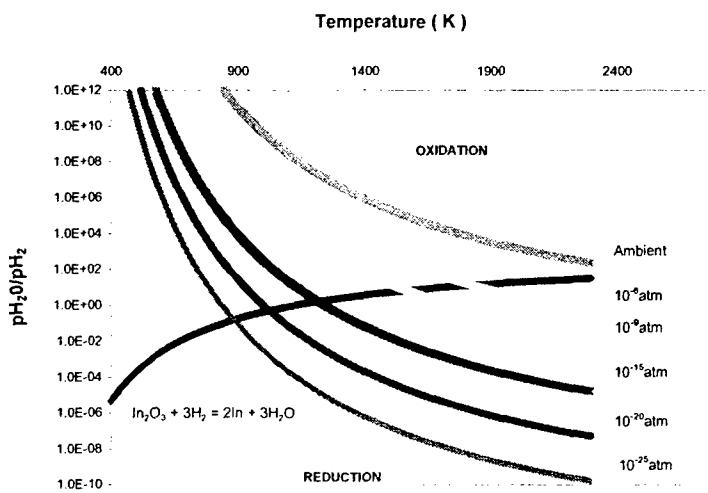

Fig. 1-3 Equilibrium moisture hydrogen ratio verses temperature with oxygen isobars.

In contrast the effect of oxygen partial pressure doesn't have much of an impact on the thermodynamic location of the oxidation and reduction zones. In Fig. 1-3 it can be seen that since the equilibrium oxygen partial pressure is so low (which correlates to a very small moisture to hydrogen ratio) changes in atmospheric oxygen partial pressures

in the range of 10^{-25} atm to air have little effect on the overall moisture to hydrogen ratio. This is due to the logarithmic relationship between the moisture and hydrogen ratio and temperature.

Kinetics

To this point we've only discussed whether a reaction is oxidizing or reducing, now we must discuss the rate at which these reactions occur. There are several kinetics models for oxidation which functionally describe how the oxides grow. These models can be narrowed down to three main categories, parabolic, inverse logarithmic, and logarithmic.

Parabolic growth rate kinetics can be most easily described as when the diffusion of ions through oxide is the rate controlling mechanism. Wagner's oxidation equation below shows the oxides growth dependence on time.

$$d^2 = A_1 e^{-Q/kT} t + A_2 \qquad (1)$$

where d is oxide thickness, Q is activation energy, k is a rate constant, t is time and A_1 and A_2 are constants. Cabrera and Mott's theory of oxidation says that the growth of an oxide layer follows an inverse logarithmic relationship. Here the rate controlling mechanism is the flow of metal ions. Growth of the native oxide layer on many metals such as copper, iron and indium can be described by this mechanism.

Finally there is Uhlig's theory electron transport which is governed by a logarithmic growth rate. Figure 1-4 shows the initial stages of oxidation where first oxygen is physically adsorbed on the metal surface, attached only by weak van der Waals bonds. Subsequently the oxygen molecules are chemisorbed with the oxygen molecules acting as the electron acceptor and the metal acting as the electron donor. Lastly that metal-oxide complex is sublimated to form the oxide lattice.
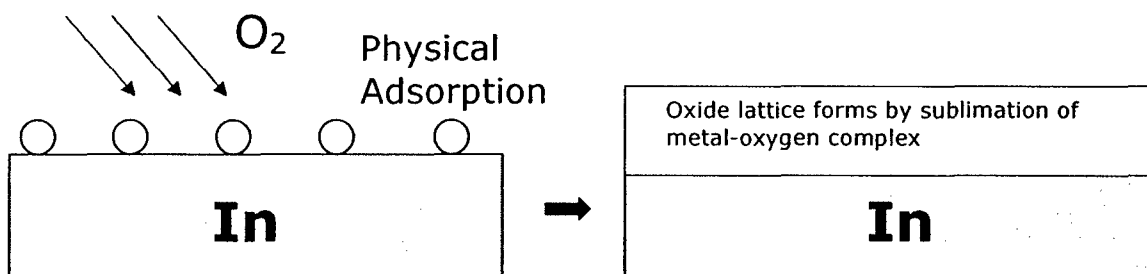

Fig. 1-4 Illustration of oxidation process.

Here the rate controlling mechanism is the follow of electrons from the metal to the oxide. When enough electrons have passed into the oxide layer a space charge layer develops across the oxide which slows down the rate of electron transport. This

translates into slower growth rates for the oxide film, after initial oxidation. The governing equation is shown below.

$$d = k_0 \ln\left(\frac{t}{\tau} + 1\right) \qquad (2)$$

where d is oxide thickness, t is time, τ is a time constant, and k_0 is an initial oxide thickness that depends on τ.

Experimental Procedure

Sample surface preparation is a very important step in oxidation experiments. Surface roughness, purity, and microstructure all impact the oxidation behavior of the material. For repeatable oxide thickness measurements it is necessary to create a sample with an ultra smooth surface condition. Samples with a rough surface will have greater oxidation because of the increased surface area.

Creation of a smooth surface finish for indium initially proved to be quite difficult. Traditional mechanical polishing of indium produces a poor surface finish because of indium's ductility at room temperature. Silicon carbide as well as silica slurry particles embed on indium's surface. This obviously would impact the oxidation behavior, kinetics, mechanical response, etc.

To solve this problem we adopted an electrochemical polishing (ECP) approach. To implement this approach we built an electrochemical polisher (seen in Fig 1-5 below) which consisted of a rectifier, anode, cathode, and a beaker for the electrolyte solution. The electrolyte solution was a 3:1 ethanol to nitric acid bath which had to be maintained at 0°C because the solution becomes unstable at room temperature.

ECP has many benefits over traditional mechanical polishing. First, ECP only takes a fraction of the time mechanical polishing takes. To mechanically polish indium to a scratch free surface takes well over an hour because of the many steps involved, whereas ECP only takes 2-5 minutes. Secondly, ECP produces a much smoother finish compared to mechanical polishing because material is removed from the peaks at a much faster rate than the valleys. Third, ECP is a stress free polishing technique. Unlike mechanical polishing where residual stresses develop on the surface, ECP does no mechanical work on the surface. Finally, ECP produces a hygienically clean debris free surface finish. As mentioned earlier, particles embedded in the sample surface due to mechanical polishing will affect the oxidation behavior.
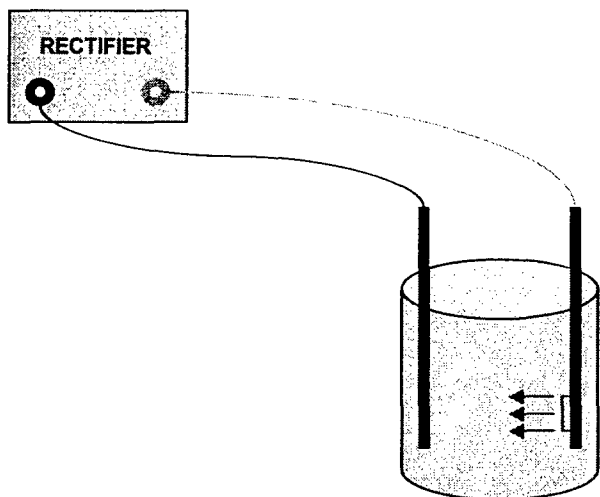
Fig. 1-5 Illustration of our electrochemical polisher.


(a)

(b)

(c)

(d)

(e)

(f)
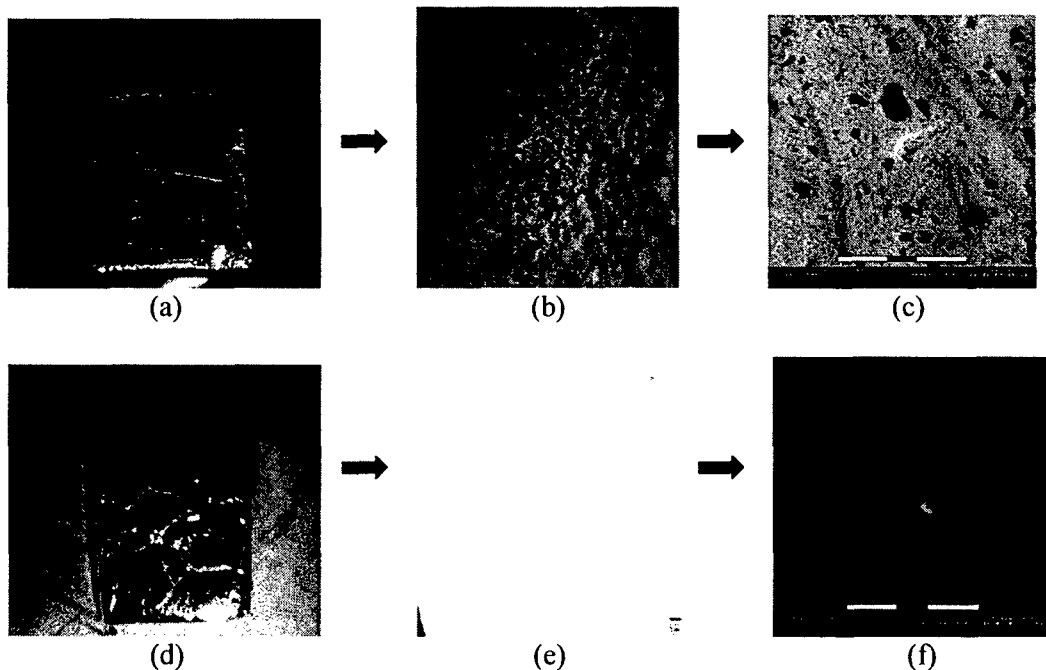
Fig. 1-6. Optical and SEM images of indium mechanically polished (a) (b) (c) , and electrochemically polished (d) (e) (f).

The images shown above in Fig.1-6 show a side by side comparison of indium mechanically polished and electrochemically polished. As we can see in images (a), (b), and (c) mechanical polishing produces a poor surface finish. Silicon carbide particles cover the sample surface, making repeatable thickness measurements near impossible. However in images (d), (e), (f) we see an ultra smooth surface finish where grain boundaries are exposed.

Sample Preparation and Temperature Measurements

First the samples were cut by razorblade into 50mm x 5mm strips. Then these strips were ECP in a 3:1 ethanol to nitric acid solution for 5 minutes at approximately 4 volts. Immediately after polishing, the samples were rinsed in distilled water for 2 minutes and then dried and stored in a nitrogen environment. Before oxidation the samples were cut into 5mm x 5mm squares. Oxidation was carried out by placing the samples on a glass slide which was placed on a hot plate. The temperature of the solder was monitored by a K-type thermocouple which was placed about 1mm from the sample surface.

Thickness Measurements through an Ellipsometer (< 40nm)

After the samples were thermally oxidized thickness measurements were carried out using NanoFilm's EP3 Spectroscopic Ellipsometer. Ellipsometry is an especially useful technique because of its nondestructive nature with little or no special preparation needed other than a relatively smooth sample surface. As demonstrated in Fig. 1-7, ellipsometry measures the thickness of thin films by reflecting known polarized light onto the sample. This polarized light reflects off both the thin film and the thin film-substrate interface resulting in a different polarization of the light. This change in polarization is analyzed in terms of s and p light which can be converted to the familiar ellipsometry variables Ψ and Δ via the following equation:

$$\frac{R_P}{R_S} = \tan \psi e^{i\Delta} \qquad (3)$$

, where R_p is the reflected p-light, and R_s is the reflected s-light.

A sample plot of Δ verses wavelength is shown in Fig. 1-8. In the plot Δ measured via ellipsometry is compared to Δ calculated theoretically from the index of refraction and extinction coefficient for indium-indium oxide system. The mean square error in this plot is then plotted verses film thickness to derive the film thickness.
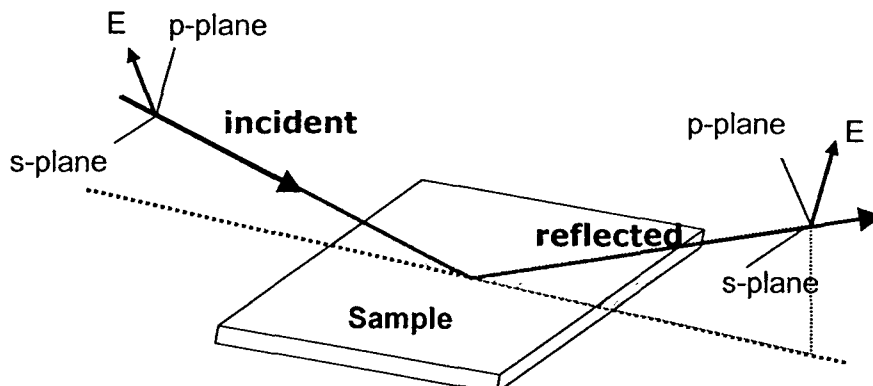

Fig. 1-7 Illustration of the ellipsometry measurement technique.

Indium Melted at 400°c (AOI 60°)
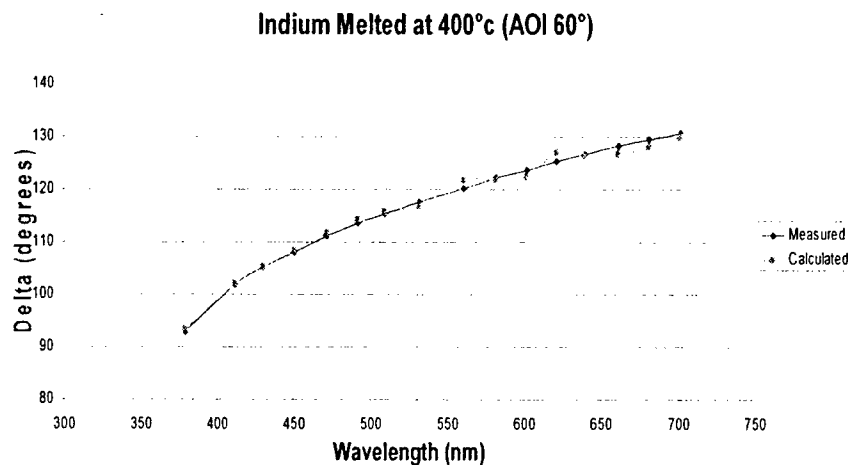
Fig. 1-8 Plot of Δ calculated and measured verses wavelength

Nanoindentation (thickness measurements > 40nm)

Nanoindentation like other hardness tests involves the penetration of the sample with an indenter. However, in nanoindentation a new depth sensing parameter, contact depth (h_c), is introduced (Fig. 9). The contact depth, the depth to which the sample is in contact with the indenter, is measured by extending the slope of the upper portion of the unloading curve to the x-intercept as below:

$$h_c = h_{max} - \varepsilon \frac{P_{max}}{S},$$

(4)

where ε is the geometric constant.
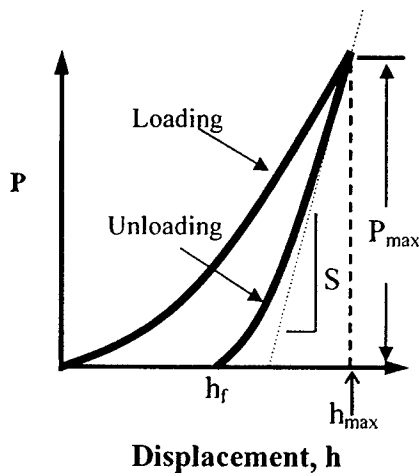
Fig. 1-9. Load (P) vs. displacement (h) plot for a typical nanoindentation loading and unloading cycle.

The area function then uses this contact depth to estimate the projected contact area. Contact area can be used to determine the hardness, H and reduced modulus, E_r of a sample from the following equations:

$$H = \frac{P}{A} \qquad , \qquad (5)$$

where P is load and A is the projected contact area, and:

$$E_r = \frac{\sqrt{\pi}}{2\beta} \frac{S}{\sqrt{A}} \qquad , \qquad (6)$$

where S is contact stiffness and β is an indenter constant. To obtain Young's modulus from the reduced modulus the follow equation can be used:

$$\frac{1}{E_r} = \frac{1-v^2}{E} + \frac{1-v_i^2}{E_i} \qquad , \qquad (7)$$

where subscript i indicates for diamond indenter, and v is Poisson's ratio.

Technical Results and Data

Oxidation and Reduction

The first oxidation experiment was the measurement of oxide thickness verses temperature in both air and in an inert environment. All samples for this experiment were heat treated for two hours. A plot of the results for the samples oxidized in air can be in Fig. 1-10.

Oxidation of Pure Indium in Air
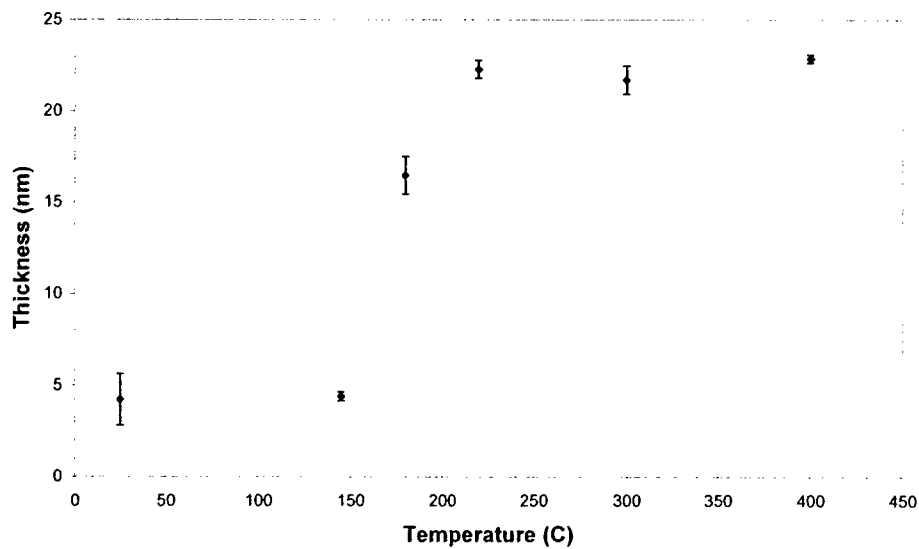
Fig. 1-10 Thickness verses temperature in air.

Several important points can be derived from this plot. First, there is little or no oxidation before the melting point (156°C). This means indium can be stored at elevated temperatures (below T_m) without significant oxidation. However, at and above T_m there is a significant increase in oxide layer growth which shows asymptotic behavior after 200°C. So, from the oxidation point of view there is no significant difference if we choose a reflow temperature of 180°C or 200°C or even 220°C. They all show similar oxidation behavior.

Conversely, oxidation in an inert environment depends heavily on temperature in that range. The samples in the plot below (Fig. 1-11) were heat treated in a glove box with $O_2 < .1$ ppm, $H_2O = 0.1$-0.3ppm, $H_2 = 0.6\%$. Here we can see how the oxidation behavior follows thermodynamic predictions. In Fig. 1-2 we see that at 0.1-0.3ppm moisture content only 0.5-0.6% hydrogen is needed to create a reducing environment. The chart below seems to agree with this prediction. Indium is oxidizing in the temperature range from 20°C-160°C. However after 160°C (i.e. after crossing into the reduction zone) the oxide thickness seems to be decreasing. Samples were also heat treated at 200° C and 300° C at this condition but measurements of these films were difficult because their shape became spherical.

Inert Heat Treatment
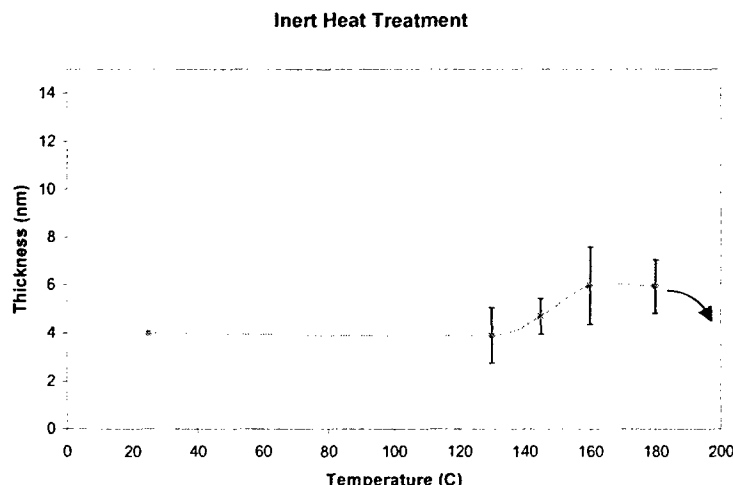
Fig. 1-11 Thickness verses temperature in glove box: $O_2 < .1$ppm, $H_2O = 0.1$-0.3ppm, $H_2 = 0.6\%$

We have tested several different conditions (oxidizing, reducing, slightly oxidizing) to confirm the validity of thermodynamic oxidation/reduction map. These data are marked as symbols on the map, and showed good correlation between experimental observations and theoretical predictions (Fig. 1-12).
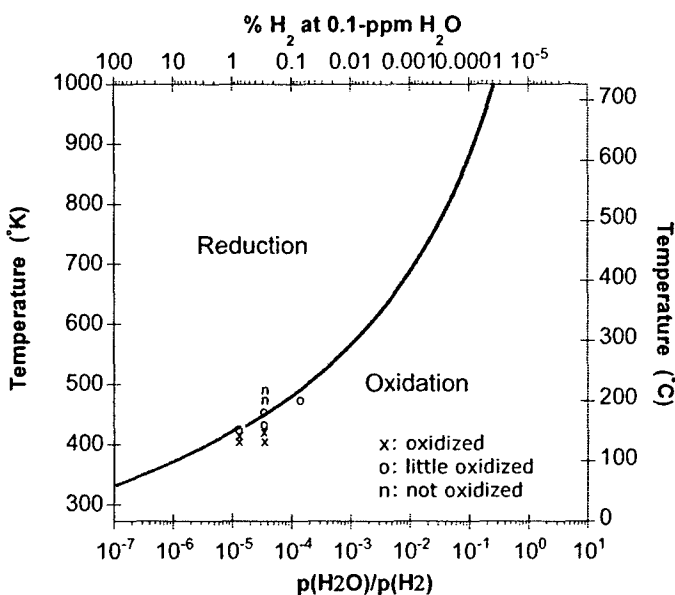
Fig. 1-12. Oxidation/reduction map: Effect of hydrogen on In_2O_3 stability and transition temperature. Symbols indicated experimental observation of indium samples at specific conditions.

Kinetics of Oxidation

The growth rate kinetics of indium was investigated in both air and inert environments. Samples were prepared and oxidized from 5 to 120 minutes at three different temperatures in air (Fig. 1-13). After curve fitting all three kinetics curves to the three kinetics mechanisms described above, the logarithmic rate law showed the best fit, all with correlation coefficients greater than 0.9. The primary reason for such a fit is the asymptotic behavior of the curves after 60 minutes. This can be explained by the space charge layer limiting the flow of electrons after 60 minutes.
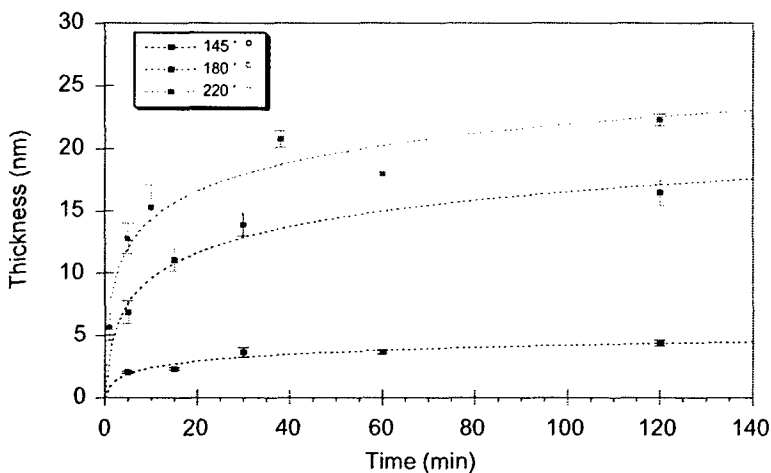

Fig. 1-13. Growth kinetics of indium in air at 145°C, 180°C, and 220°C.

Another supporting piece of evidence for logarithmic oxidation is the initial activation energy barrier when oxygen is chemisorbed onto the surface of indium. Theoretical calculation from the Rideal and Wansbrough-Jones relation:

$$\Delta E = \Phi - K \qquad (8)$$

where ΔE is the activation energy, Φ is the work function, and K is the electron affinity of the oxygen atom. Theoretical calculation of the activation energy for initial oxidation is .52eV. As seen in the graph (Fig. 1-14) the experimental value of this energy is .65eV (62.6 kJ/mol), which is quite consistent with the calculation.
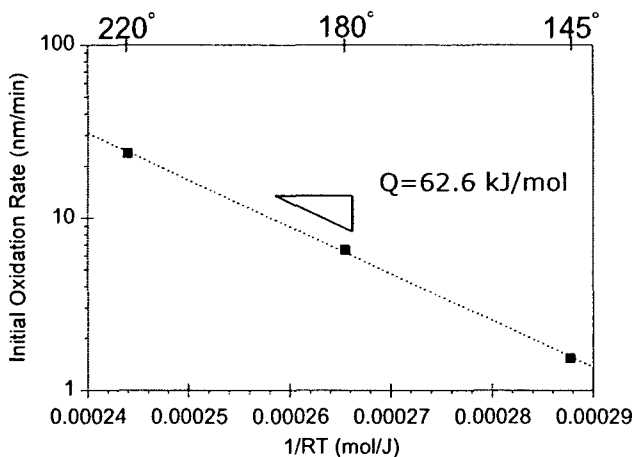

Fig. 1-14 Initial activation energy experimentally determined to be 62.6 kJ/mol (.65eV).

Oxidation kinetics experiments were also carried out in the glove box (Fig. 1-15). The preliminary results from this experiment are shown in the plots below. It seems there is no discernable pattern in these results since all the values fall within the range of the native oxide layer. So it would be safe to assume the growth kinetics are very slow in such an environment ($O_2 < .1$ppm, $H_2O = 2.3$ppm, $H_2 = 4\%$).
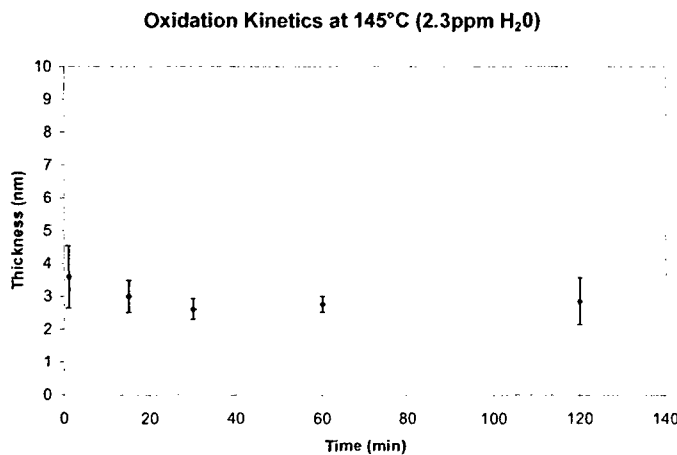
**Fig. 1-15.** Growth kinetics of indium in glovebox ($O_2 < .1$ppm, $H_2O = 2.3$ppm, $H_2 = 4\%$) at 145°C.

Reduction

Reduction of indium oxide from a pure indium substrate proved to be quite a difficult task due to indium oxides stability at high temperatures. We first attempted to reduce indium oxide using argon plasma cleaner to bombard the oxide with ions. Preliminary results from this experiment shown in Fig. 1-16, where an etching rate of 5.3 nm/hr was observed at 270 watts.
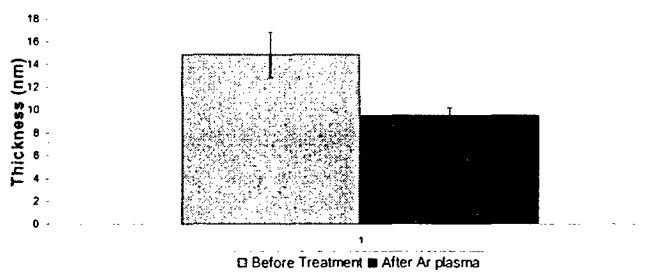

Fig. 1-16. Reduction of indium oxide via an argon plasma cleaner.

Reduction was also attempted by adding hydrogen to the glove box environment to make indium oxide unstable relative to indium at oxygen partial pressures much greater than the equilibrium oxygen partial pressure. Figure 1-17 shows a thermodynamic map where samples are oxidized at conditions left of the equilibrium curve, and reduced at conditions to the right of the curve. Many experiments were preformed in the reduction zone with no noticeable reduction of the oxide layer. Only a harsh reducing environment showed a reduction in the oxide layer. With the temperature set to 350°C, H_2 = 4.5%, O_2 < .1ppm, and H_2O = 7ppm the oxide layer was reduced from 21nm to 15nm after 6 hours, yielding an etching rate of 1nm per hour, as shown in Fig. 18. This clearly demonstrates the need for very low moisture levels so the temperature can be reduced into an acceptable range.
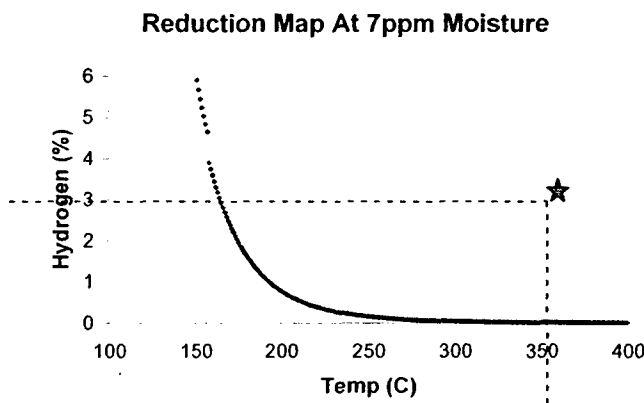

Fig. 1-17 Thermodynamic map of indium oxide reduction at 7ppm moisture.

Hydrogen reduction of Indium Oxide
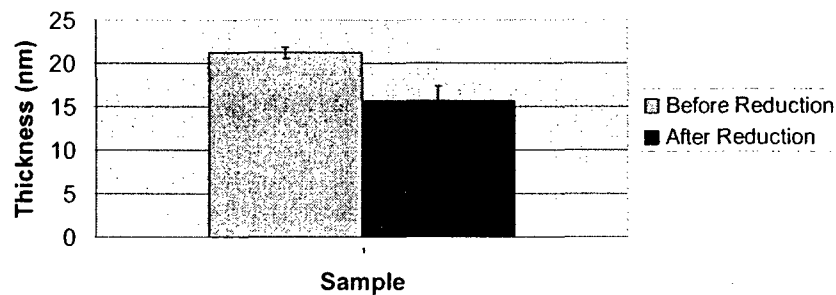
Fig. 1-18. Reduction of indium oxide via a 4.5% hydrogen gas.

Figure 1-19 shows the sample coupons before reduction experiments (i.e., 21 nm thick oxide on indium) and after reduction experiments (i.e., 15 nm thick). After being exposed to reducing environment, the coupon became more rounded, indicating that oxide layer gets somewhat removed.


(a)   (b)
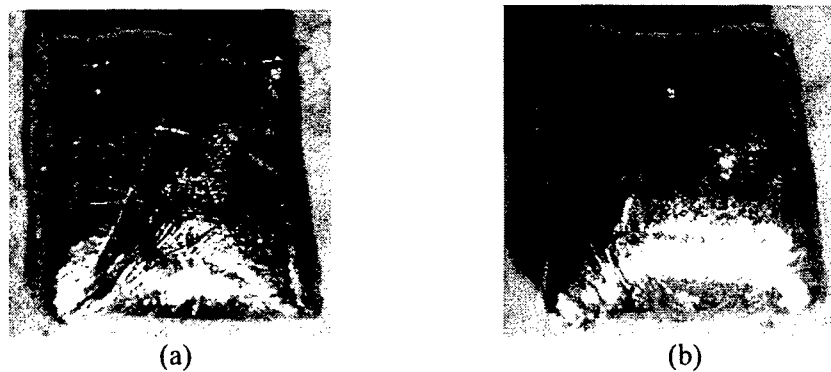
Fig. 1-19 (a) Sample before reduction (b) sample after reduction.

Thickness measurements via Nanoindentation

Dynamic nanoindentation superimposes a sinusoidal load on top of a quasi-static load to obtain contact stiffness measurements continuously as a function of displacement. Given the material system indium-oxide/indium there is an obvious change in the contact stiffness as the indenter travels past the film into the substrate. This allowed us to estimate the thickness of several films grown at higher temperatures. Figure 1-16 shows both the dynamic and quasi-static nanoindentation plots where there is a sudden displacement burst as the indenter travels past the oxide. Figure 1-20 (a) and (b) show this behavior at a displacement around 100 nm whereas Fig. 1-20 (c) and (d) show this behavior at around 800 nm.

Indium Melted at 500°C For 1hour

Quasi-Static Load Control (500°C)

(a)

(b)

Quasi-Static Load Control (600°C)

Indium Sample Melted at 600°C

(c)

(d)
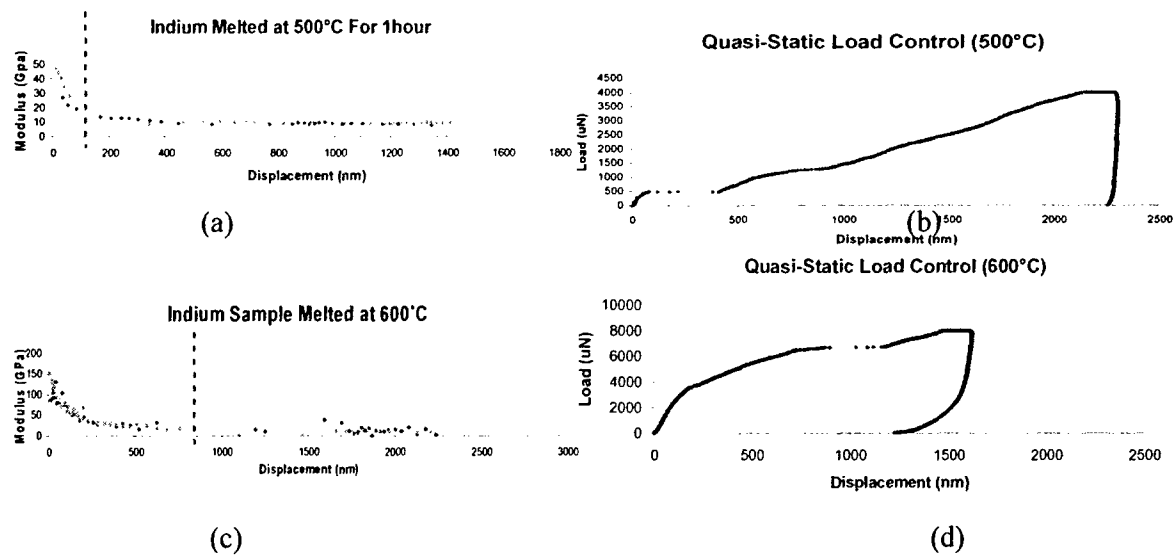
Fig. 1-20 Dynamic and quasi-static nanoindentation results for indium heat treated at 500°C and 600°C respectively.

Materials Characterization

NanoDMA Estimation of Elastic Modulus on Indium

NanoDMA Estimation of Hardness for Indium

(a)

(b)

Indium Melted at 1000°C

Indium Melted at 1000°C

(b)

(d)
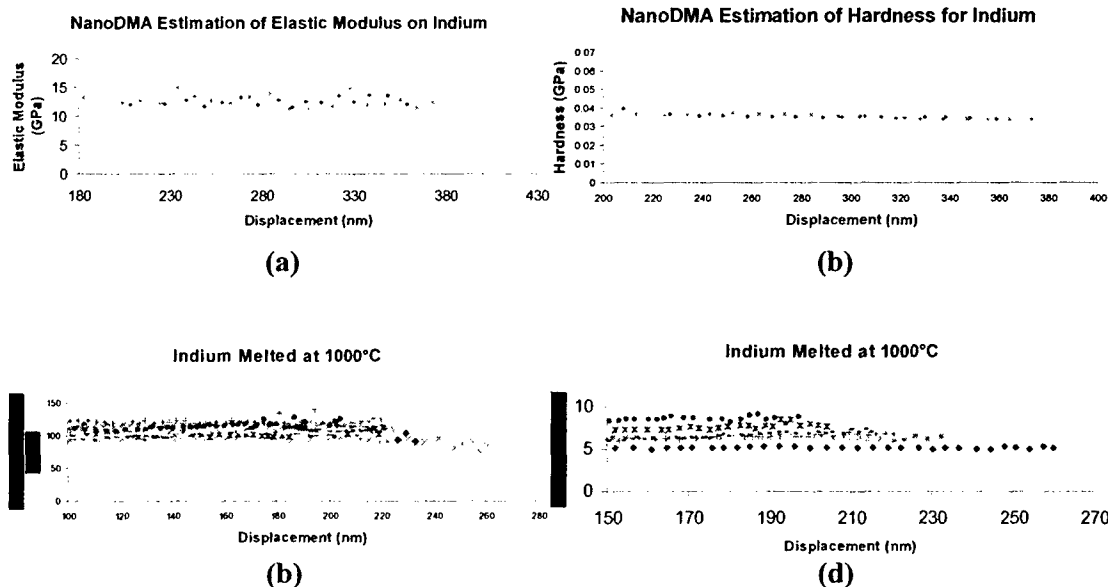
Fig. 1-21 (a) elastic modulus of indium; (b) hardness of indium; (c) elastic modulus of indium oxide; (d) hardness of indium oxide. (note that thick indium oxides were grown from melting at high temperatures)

Materials characterization of both indium and indium-oxide where carried out using nanoindentation, optical microscopy, AFM, SEM, and XRD. Results from the mechanical characterization using dynamic nanoindentation are shown below.

The elastic modulus of indium was measured to be 12.4 ±.34 GPa, and the hardness was 39.7 ± 1.2 GPa. The modulus of indium oxide was measured to be 105.85 ± 7.6 GPa and the hardness 6.64 ± .96 GPa (Fig. 1-21). Microstructural characterization of indium oxide annealed at 1000 °C was preformed using AFM. From Fig. 1-22 we can see that the microstructure is composed of oval grains 200-300 nm in size. The grains of indium seen earlier are much larger 2-4 mm.
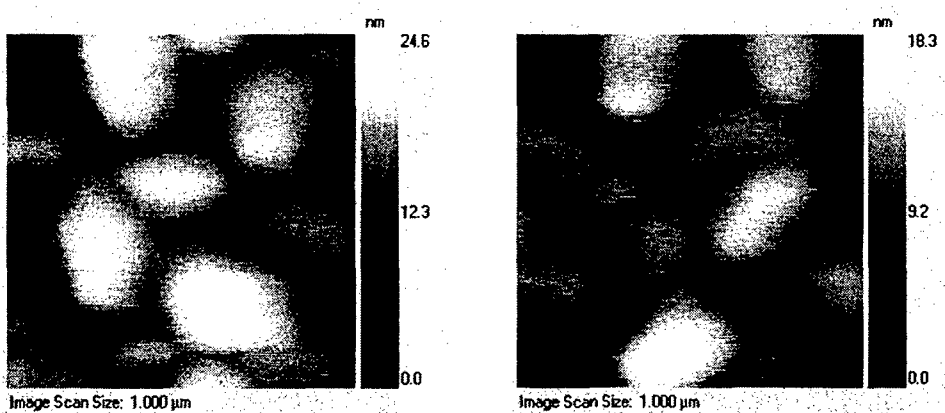

Fig. 1-22 AFM images of indium oxide annealed at 1000 °C.

X-ray Diffraction (XRD) Analysis

The crystal structure of the TGO grown on indium samples was analyzed using X-ray diffraction. Samples below and above the melting temperature were tested to determine any changes in the crystal structure of indium oxide. Below are the resulting X-ray intensity verses 2θ plots. It can be seen from these plots, that below the melting temperature no crystalline phase of indium oxide was detected.
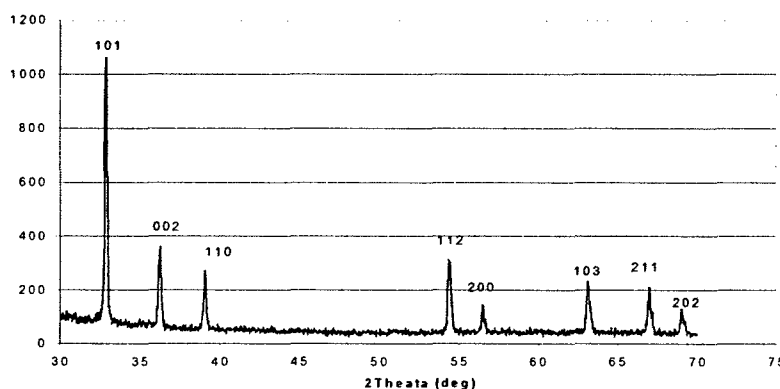

Fig. 1-23 XRD plot of intensity verses 2theata for the sample annealed at 153°C for 4 hours. The peaks labeled are from pure indium metal (substrate).

Figure 1-23 represents the XRD plot of indium annealed at 153°C for 4 hours. Here the peaks only correspond to the crystal structure of the pure indium. Therefore, it is believed that indium oxide grown below the melting temperature is of an amorphous nature. Conversely, when indium was annealed above the melting temperature a cubic indium oxide crystal structure was detected. Below in Fig. 1-24 the peaks correspond to a cubic crystal structure for indium oxide when the sample was annealed for four hours at 200°C. When treated above the melting temp the sample begins to flow resulting in a rough, deformed surface. This may also explain the excess "noise" in the plot.
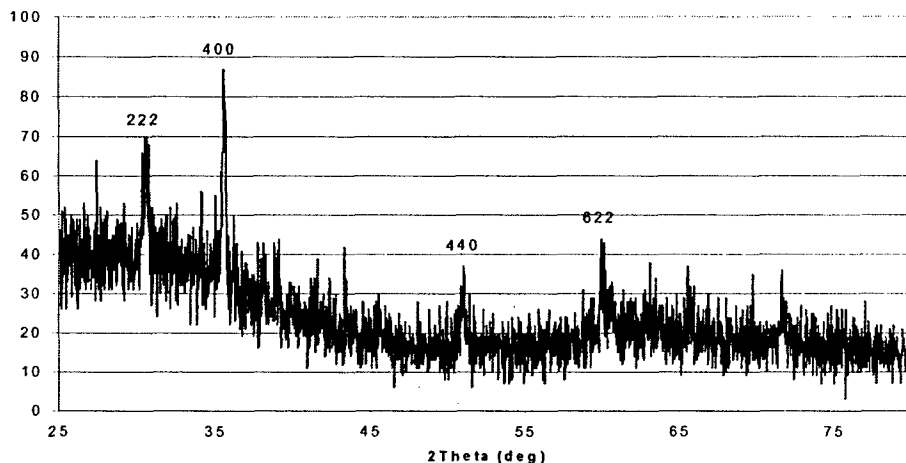

Fig. 1-24 XRD plot of intensity verses 2-theata for the sample annealed at 200C for 4 hours. The peaks labeled are from indium oxide (film).

Conclusion

There are several conclusions that can be made regarding the creation of a solder reflow processing window. From the thermodynamics point of view the four main parameters, temperature, oxygen content, moisture content and hydrogen content can be precisely controlled to produce a reducing or inert (reducing but very slow etching rate) environment. Our calculations revealed that moisture is a critical parameter in the creation of a reducing environment. Reducing the moisture to the lowest possible levels shifts the equilibrium curves to the left which lowers the temperature and hydrogen content needed to create the reducing environment. We also observed that oxygen content is not a critical parameter for producing a reducing environment. Shifting the oxygen content from 1ppm to 500ppm will not shift the location of thermodynamic equilibrium.

With regards to the kinetics investigation, we found that the growth rate is controlled by a logarithmic relationship. In the growth rate equation the parameters τ and k_0 reveal the initial onset of oxide growth k_0 in time τ. If the reflow time can be held below τ significant oxidation can be avoided. We also saw that that there is little or no oxidation samples when samples were heat treated in the glove box below the melting

temperature. This means samples can be stored in the glove box with no significant additional oxidation (other than native oxide).

As for the reduction of indium oxide in a hydrogen environment, we found the kinetics to be very slow in regions close to thermodynamic equilibrium. Only very harsh conditions (T > 350°C) reduced the oxide. However by further reducing the moisture content, the service temperature should also be reduced into an acceptable range. In this case, pre-reflow conditions for an extended period prior to joining may enable to remove initial oxides formed on the surface of indium. More experiments are warranted to quantitatively verify the reduction kinetics. Using the attached thermodynamic program (see Appendix A) will guide the search for proper reflow environments.

Appendix A.

Thermodynamic Reflow Code (MATLAB Program):

```
%Harry Schoeller
%Thermodynamic Program
%This program determines whether your environment will oxidize or reduce
%indium solder

Y = input('Welcome To The Indium Solder Reflow Environment Calculator:  Run (1) or
Exit (2):  ');
while Y == 1,
Z = input('\nWhich parameter would you like to hold constant pH20 (1), pH2 (2), pH20
and pH2 (3):  ');
if Z == 1,
    P = input('Enter the total pressure of the system (atm):  ');
   pH201= input('Enter the pH20 (ppm):  ');
   p021= input('Enter the p02 (ppm):  ');
    T1 = input('Enter the reflow temperature (C):  ');
    p021 = p021* (10^-6);
    pH20 = pH201*(10^-6);
    T = T1 + 273;
    if T <= 430,
       G = 183300 - 151.5*T;
    else
       G = 189300 - 168.1*T;
    end
    H = (pH20/(exp(G/(-8.3144*T))^(1/3)))*100;
    if H > 100,
       fprintf('Indium oxide cannot be reduced with this moisture/temperature
combination, please increase temperature or reduce moisture content');
    else
    fprintf('Your environment needs at least %4.4f percent hydrogen gas to reduce
indium oxide', H);
    end
```

```
        Y = input('\nWelcome To The Solder Reflow Environment Calculator: Run (1) or
Exit (2): ');
elseif Z == 2
    P = input('Enter the total pressure of the system (atm): ');
    pO21= input('Enter the pO2 (ppm): ');
    H= input('Enter the percentage of hydrogen gas: ');
    T1 = input('Enter the reflow temperature (C): ');
    T = T1 + 273;
    if T <= 430,
        G = 183300 - 151.5*T;
    else
        G = 189300 - 168.1*T;
    end
    pH20 = ((H/100)* (exp(G/(-8.3144*T))^(1/3)));
    pO21 = pO21* (10^-6);
    ppm = pH20/(.00001);
     fprintf('Your environment should contain less than %4.4f ppm H2O to reduce indium
oxide', ppm);
        Y = input('\nWelcome To The Solder Reflow Environment Calculator: Run (1) or
Exit (2): ');
elseif Z == 3
    P = input('Enter the total pressure of the system (atm): ');
    pO21= input('Enter the pO2 (ppm): ');
    pH201= input('Enter the pH20 (ppm): ');
    H= input('Enter the percentage of hydrogen gas: ');
    pH20 = pH201*(10^-6);
    pO21 = pO21* (10^-6);
    H1 = H/100;
    T = (-22767.7/(log((pH20/H1)^3)-20.2));
    T2 = T - 273;
    fprintf('Your reflow temperature should be at least %4.2f C  to reduce indium oxide',
T2);
    Y = input('\nWelcome To The Solder Reflow Environment Calculator: Run (1) or Exit
(2): ');
end
end
```

1-2. Wettability/Solderability

Sample preparation

Indium solderability was assessed by wetting angle measurement and joint strength measurement with a single lap shear test. Indium oxide thickness was taken of an experimental parameter to affect the solderability. The indium oxide was grown at different temperatures(25 °C, 145 °C, 160 °C and 200 °C) for 2 hours on a hot plate. The measured oxide thickness is listed in the table 1-1.

Table 1-1 Indium oxide thickness vs. temperature (2 hours annealing)

Temp(°C) Oxide thickness	25	145	160	200
AVG (nm)	4.0	5.2	13.9	16.9

Before the indium solderability test, the shape of indium-bonding substrate(6.5 by 28 mm) and size of bonding pad were manufactured on the silicon wafer by micro-fabrication process in Figure 1-25. Au and titanium were then deposited on the several silicon wafers. In the region except for indium bond area(3.5 by 3.5 mm), Au and titanium were clearly removed by chemically dissolving method in Figure 1-26. The deposited thickness of Au layer is 0.5 um, and that of titanium is 0.04 um. Titanium was used to improve the adhesion of indium to the silicon substrate, and Au was used to protect the titanium from oxidation in air.
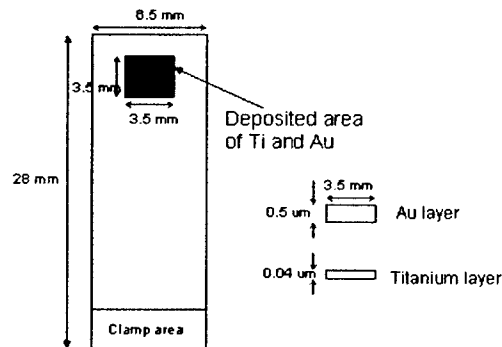

Fig. 1-25 Silicon substrate design   **Fig. 1-26** Detailed size of silicon substrate

Wetting angle measurement

The indium for wetting angle measurements was melt on the Au-deposited silicon wafer using hot plate(200 °C for 2 min.) in an air and in a glove box. The atmosphere condition in a glove box was controlled by the concentration of moisture, nitrogen and hydrogen gas. The glove box can be operated at $H_2O < 1$ ppm, $O_2 < 0.1$ ppm, and $H_2 < 5$

%. After the wetting was formed, wetting angles were measured by Wyco surface profiler and were determined at the interface of indium and the Au layer on the substrate.

Pure indium(with 4 nm oxide thickness) wetting shapes at an ambient condition and in a controlled environment($O_2< 0.1$ ppm, $H_2O< 1$ ppm, and $H_2=1.5$ %) are compared with each other in Figure 1-27(a) and (b). The wetted indium in an air ambient condition is just melted on the Au layer in Figure 1-27(a), but the wetted indium in a controlled glove box environment shows the pronounced spreading after melting on a hot plate at 200 °C, as shown in Figure 1-27(b). After all, the indium wetted in a controlled glove box environmental condition shows better wetting than that in an air ambient condition.


(a) In an air ambient condition   (b) In a controlled environment
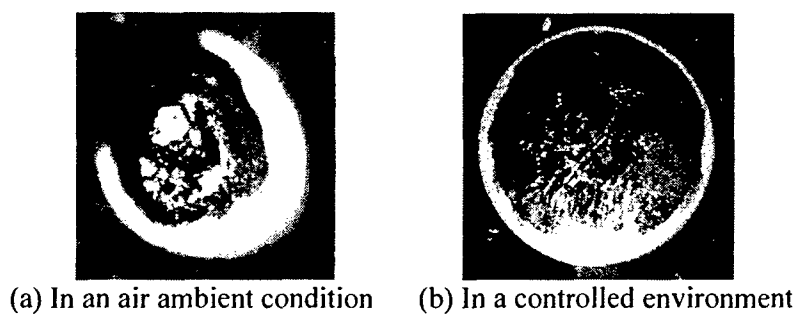
Fig. 1-27 Wetting shapes of indium

Figure 1-28 shows wetting angle measurements with initial indium oxide thickness quantitatively. In a case of 4 nm thickness indium oxide, indium wetting angle on Au layer is about 15 degree. The wetting angle was increased to 30 degree at 17 nm thickness indium oxide.
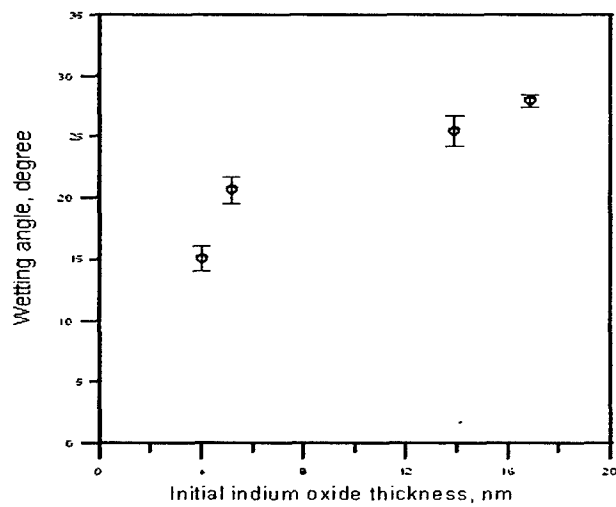

Fig.1-28 Wetting angle variation with initial oxide thickness in a controlled environment

Joint strength measurement

Indium was reflowed on the Au layer between a pair of silicon substrates for single lap shear joint test at different environments. The test geometry is shown in Figure 1-29. First of all, indium reflow for bonding was performed on the hot plate using a specially designed fixture(Figure 1-30) in an air. The reflow condition of indium is around 230 °C for 10 minute in an air ambient condition.
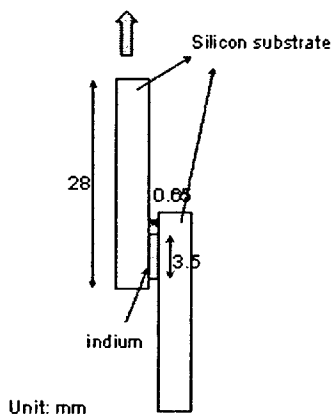

Fig.1-29 Test geometry for joint shear test
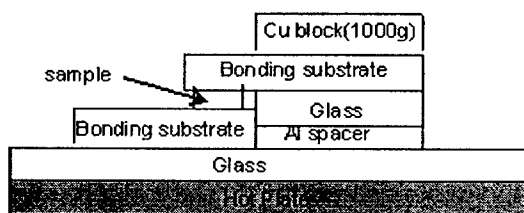
Fig.1-30 Design of test fixture for joint shear test

Figure 1-31 shows a real joint test sample with 4 nm oxide thickness before joint test. Indium was embedded and reflowed to each Au layer between two silicon substrates. After performing indium joint failure test by single lap shear, the failure was dominated by interfacial mode failure between indium and the substrate, as shown in Fig.1-32. The 40 time magnified view of Fig.1-32 shows a lot of void traces formed at the interface between indium and the substrate in Figure 1-33.

Fig.1-31 Real bonded sample for joint test
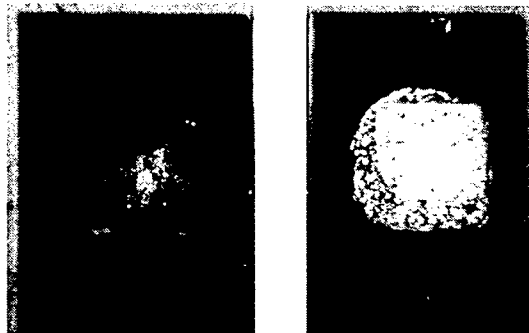
Fig.1-32 Interfacial failure between indium and bond substrate
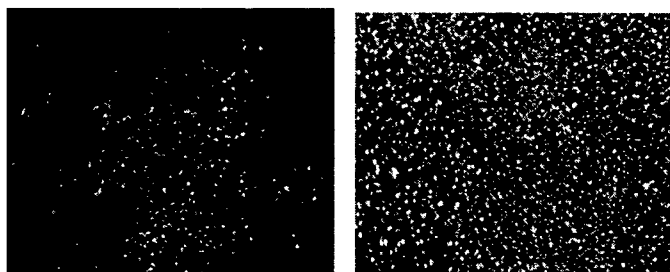

Fig.1-33 Magnified view(40 X) of indium failure site in Figure 8

Figure 1-34 shows one of representative curves which were tested for indium with a 4 nm oxide thickness in an air reflow condition. The reflow temperature of indium is 230 °C. The indium joint strength by a single lab shear is 1.35 Mpa with standard deviation of 0.2 Mpa at a strain rate of 0.5 mm/sec.

Figure 1-35 shows the joint strength variation with the change of initial oxide thickness. As initial oxide thickness is increased, indium joint strength is decreased to below 1.0 Mpa due to the existence of void defect and of much thicker indium oxide.

Environmental condition in a glove box can be controlled by the concentrations of hydrogen and moisture in Figure 1-36, which is drawn by thermodynamic calculation for indium oxidation phenomena. An oxidizing condition is reached below each line corresponding to the moisture concentration. On the above line, the condition will be in a reduced environment. On the line, the atmosphere is in an inert environment.
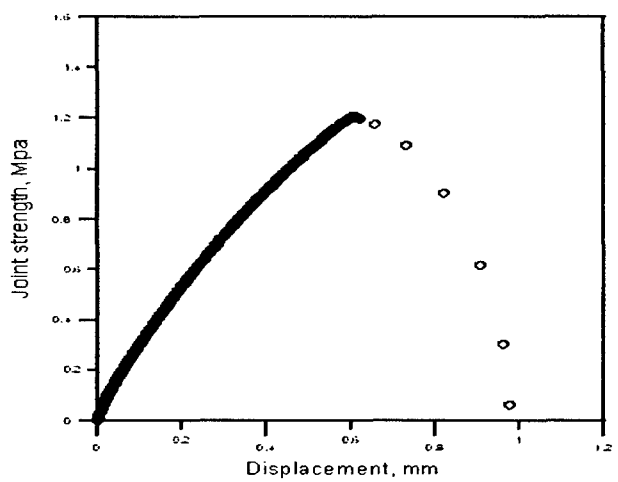
**Fig.1-34** Indium joint strength with 4 nm initial oxide thickness in an air reflow condition(230 °C for more than 5 minutes)
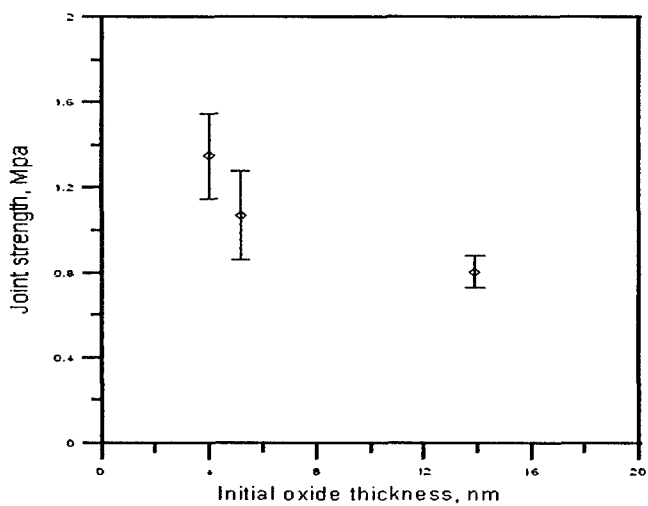

Fig.1-35 Indium joint strength with initial oxide thickness in an air reflow condition (230 °C for more than 5 minutes)
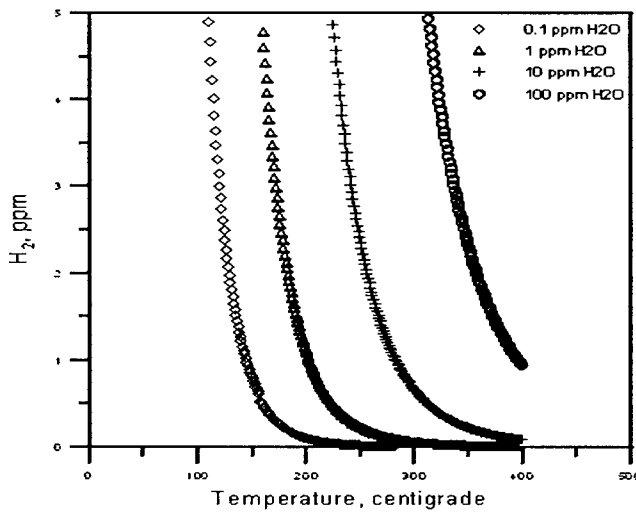
Fig.1-36 Moisture effect on the environmental condition in a glove box

Figure 1-37 shows indium joint strengths with initial different oxide thicknesses. The joint strength was dropped with the increase of initial oxide thickness. Those tested samples were made by using specially designed fixture(Fig.3.6) at controlled oxidizing glove box condition(H_2O < 6 ppm, O_2 < 0.1 ppm, and H_2 < 4 %). The reflow condition for indium bonding on the substrate was 160 ~ 170 °C for 5 minutes. The joint strength is measured by tensile loading at 2 mm/sec strain rate.
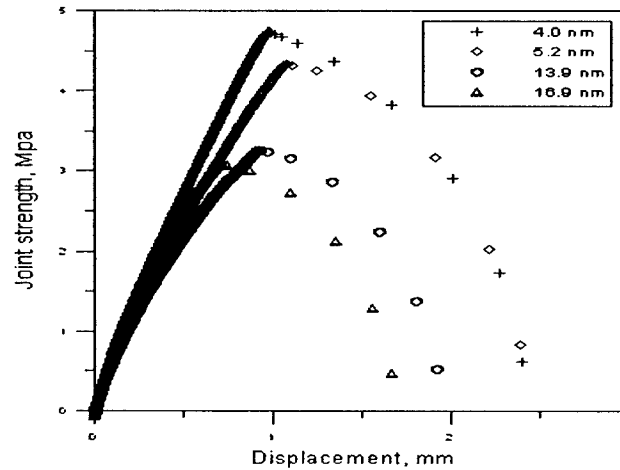
Fig.1-37 The comparison of indium joint strengths with initial different oxide thickness at controlled environmental glove box condition

Figure 1-38 is plotted to compare indium joint strength made at a controlled environment with that of an air ambient environment. There is a big difference of joint strength depending on the environmental conditions that the samples were prepared. Those testing results are obtained by the samples which are made with the same specially designed fixture. The fixture was designed to apply hot pressure on indium when it was

melt. In order to obtain the indium joint strength on Au layer without pressure, indium was put to be melt on the deposited area of Au on the silicon substrate without any pressure, and then tested by die shear load at 2 mm/sec strain rate using Dage bond tester. The die shear load results are also added to the Fig.1-38.
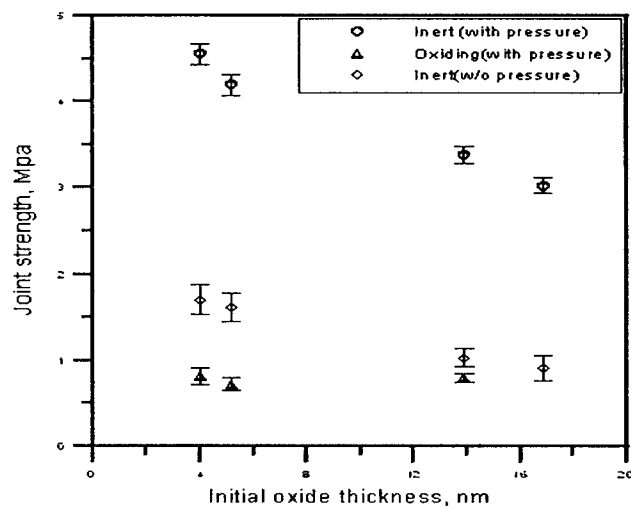
Fig.1-38 The variation of indium joint strength at different environmental condition and indium bond condition

Figure 1-39 shows the trace of indium bond site after joint failure test. The Au and titanium were observed at one side of bond substrate and the indium was remained at the other side substrate.

(a) Top substrate   (b) Bottom substrate
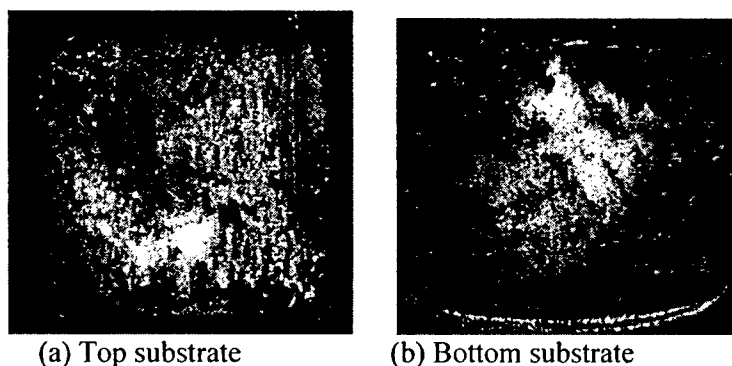
Fig.1-39 View of bonded surface after joint failure at the controlled environmental glove box condition

Sub Task 2: Thermo-mechanical Analyses

Performer – Bahgat Sammakia / Bill Infantolino / Harita Machiraju
Organization – IEEC - Binghamton University

Introduction

The objective of the thermal analysis was to obtain the temperature distribution of the complete S&A chip package which consists of the SOI (silicon on insulator) chip bonded to the kovar carrier. The boundary conditions were estimated based on the models provided by Indian Head. The model prepared based on the design information received, was called the base case model. The temperature distribution for the base case model was obtained. A set of parametric studies and design changes were studied in order to reduce the power requirements for the actuators. The base case model was used as a reference for all the parametric studies performed. A computational fluid dynamics model was also prepared to determine the pressure rise due to the air temperature increase within the sealed package.

The S&A chip consists of three sets of micro actuators – arming, flow sensor and g-sensor actuators, on its device layer (as shown in Figure 2-1). The micro actuators, when powered, provide the necessary displacement to perform a specific function, e.g., move an optical fiber. The micro-actuator is essentially a beam which deflects when heated due to thermal expansion.

A three dimensional model was prepared to perform the thermal analysis. The initial model was a single beam model which was done to gain an understanding of the temperature distribution in the beam and the effects of various types of heat transfer on the beam temperature. It was also done to compare the numerical results to known analytical solutions with similar boundary conditions.
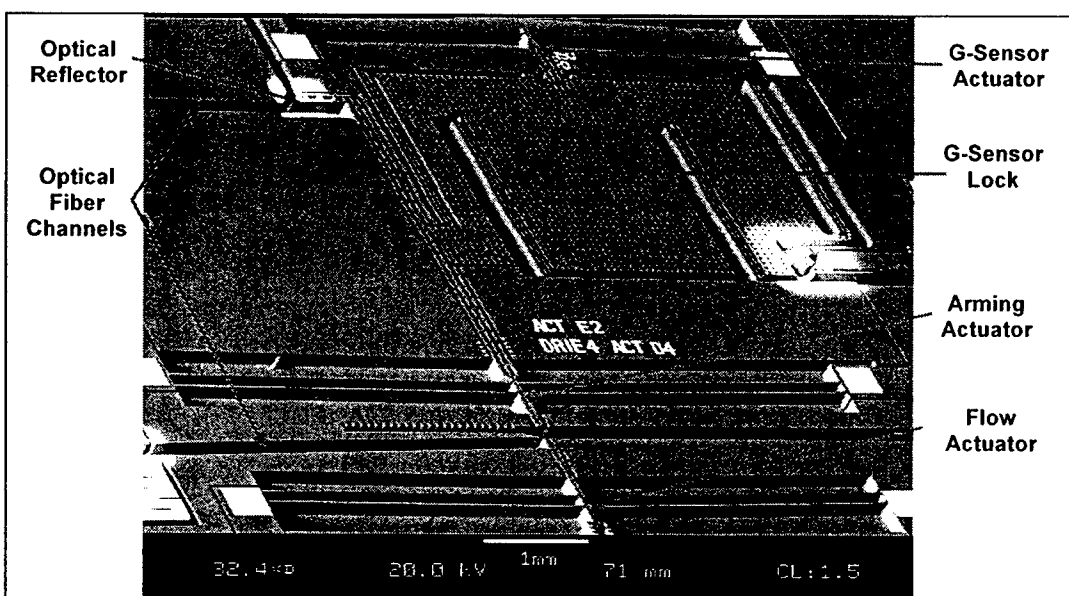

Fig. 2-1: S&A chip with the three sets of actuators

2-1. Thermal analysis of a micro beam

Description of model:
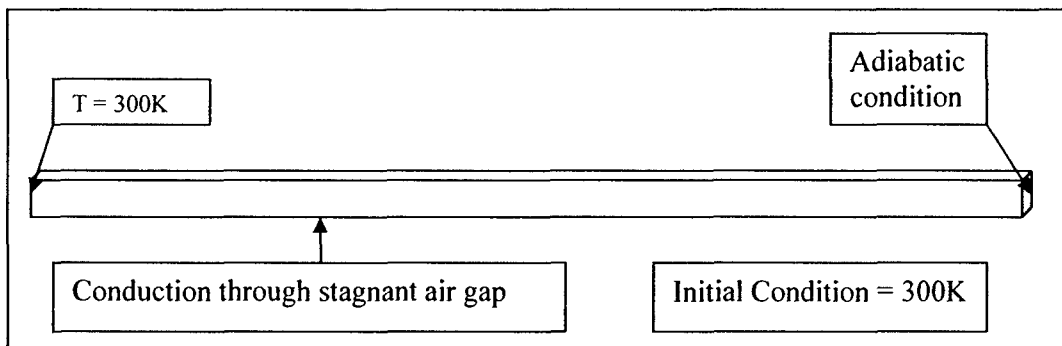
Fig. 2-2: One half of the micro-cantilever beam with symmetry loading conditions

The beam in the initial model, shown in Figure 2-2, was considered to be attached to one anchor at each end. Since these anchors are relatively large masses compared to the beam itself and the time for the analysis is relatively short, the anchors were assumed to be at a constant temperature. The power input to the actuator was assumed to generate heat uniformly within the whole beam. The heat generation is not, however, extended to the anchors. Only half of the beam was modeled due to symmetry.

The length of the beam modeled was 5500 microns, the height of the beam, 125 microns and the width of the beam, 10 microns, based on the inputs provided at that time. The numerical software used for performing the analysis was ANSYS and the element type used for the beam was SOLID 70 (3D Thermal element). The material properties for this analysis are shown in Table 2.

Material Property	Material	Value
Thermal Conductivity (W m^{-1} K^{-1})	Silicon	145
	Air	0.03
Emissivity	Silicon	0.7
Density (kg m^{-3})	Silicon	2330
Heat Capacity (J kg^{-1}K^{-1})	Silicon	729.614

Table 2-1: Material properties used for this analysis

Mesh Convergence Study:

The conduction through the stagnant air gap at the base of the beam results in the removal of a significant amount of heat. However the temperature gradient along the height of the beam due to this effect was small. The gradient was high toward the ends of the beam. Therefore, the number of elements in the region close to the constant temperature end is higher than in the center of the beam. The results of the mesh convergence study are shown in Figure 3. With the help of this study, the optimum number of elements to be used for the analysis was determined.
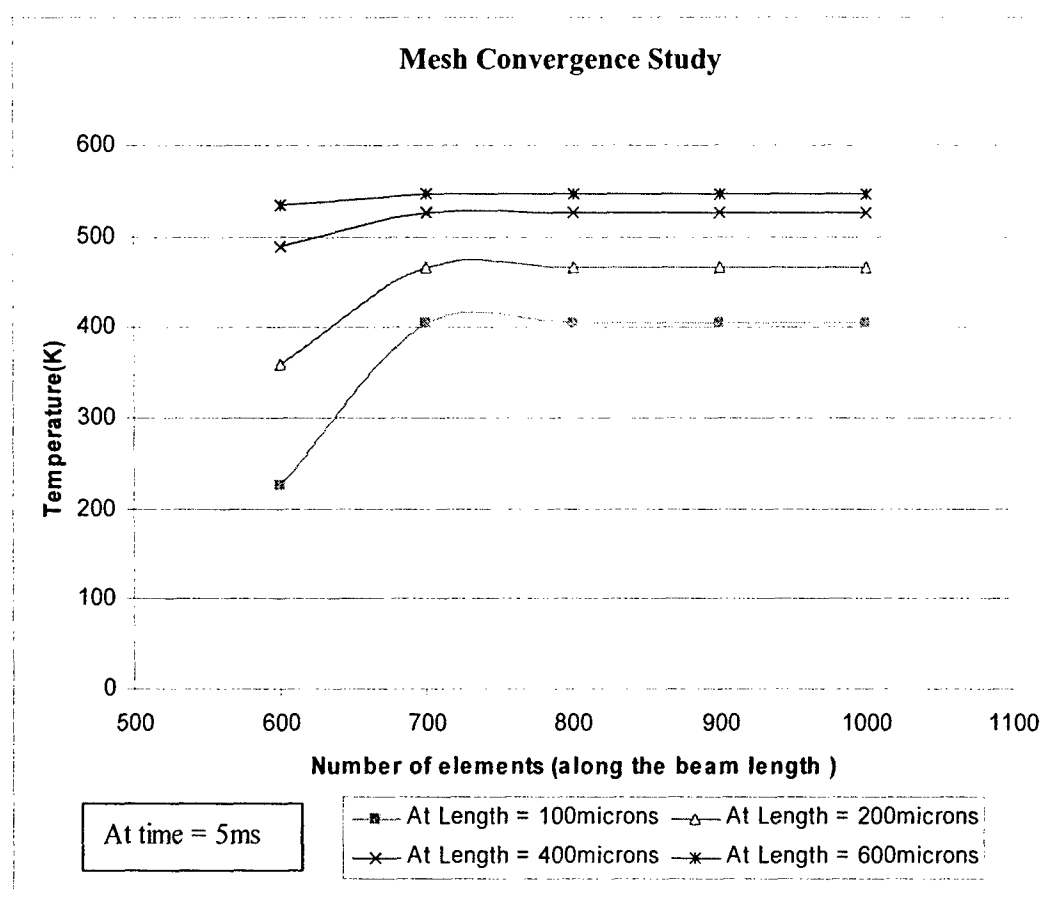
Fig. 2-3: Mesh convergence plot for a power input of 5 Watts and time period of 5 milliseconds.

Comparison of numerical model temperature profile to analytical solution:

The first case was modeled with boundary conditions which allowed comparison to a known analytical solution for verification of the analysis. Only half of the beam was modeled since the beam and loading conditions were symmetric. The beam was subjected to a fixed temperature at one end and an adiabatic condition to simulate the symmetry at

the other end. A power input of 5 Watts was applied. A transient analysis was performed and the maximum temperatures were determined for various times.

The maximum temperatures reached in the system are shown in Figure 4. Note that many temperatures are above the melting point of silicon and are calculated from the finite element model only for comparison to the analytical model.

Maximum Temperature Vs Time
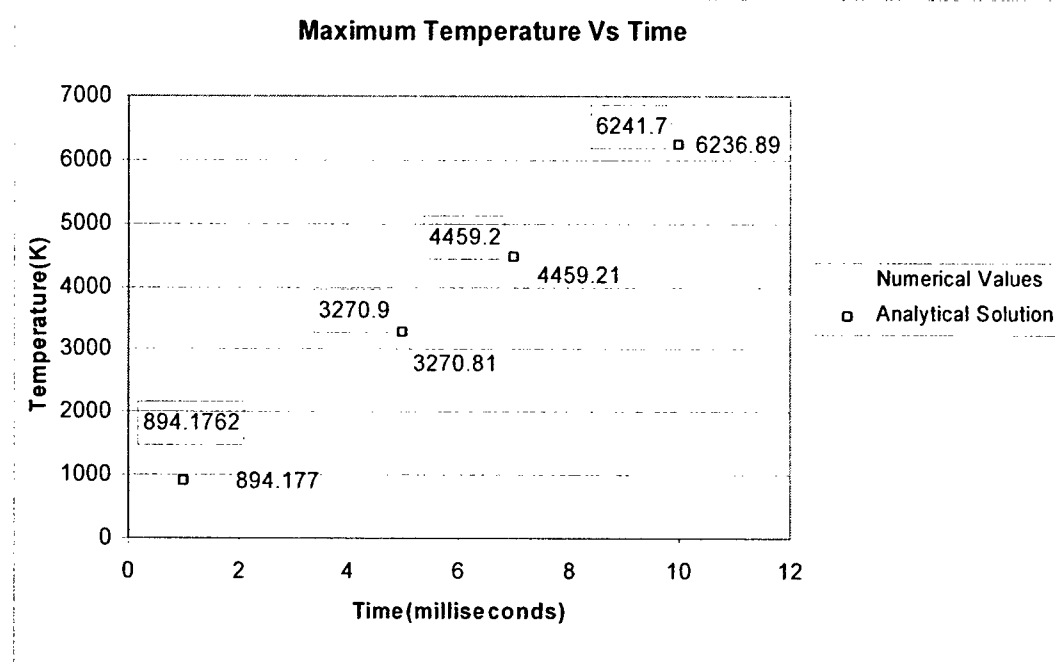
Fig. 2-4: Comparison of analytical and numerical solution for single beam model – fixed temperature at one end.

The results for the above case were verified using the analytical solution with the same loading conditions. The expression for the temperature distribution in a semi-infinite solid with a fixed temperature condition at one end and an adiabatic condition at the other end [1] is given by

$$v = \left(a + \frac{\alpha t\, A_o}{k} + \frac{A_o x^2}{2k} \right) erf\left(\frac{x}{2\sqrt{\alpha t}} \right) + \frac{A_o x}{k} \left(\frac{\alpha t}{\pi} \right)^{1/2} e^{-\frac{x^2}{4kt}} - \frac{A_o x^2}{2k} \qquad (1)$$

where   a = Initial temperature (K)
         α = Thermal diffusivity (sec m^{-2})
         t = Time (seconds)
         A_o = Heat generation rate (W m^{-3})
         k = Thermal conductivity (W m^{-1} K^{-1})
         x = Position along the beam (m)

Figure 2-5 shows good agreement between the analytical solution and the finite element model. Calculated temperatures shown in Table 2-2 at various positions along the beam are compared to the model results. For example, when

a=300K
$\alpha = k/\rho C = 145 / (2330 * 729.614) = 8.5294e\text{-}5 \ m^2/sec$
t = 10 milliseconds
$A_o = 5W/volume = 1.0101e12 \ W/m^3$
$K = 145 \ W \ m^{-1} \ K^{-1}$

The results show that the error is approximately 1 % for a range of nodal positions.

Nodal Position(microns)	ANSYS(K)	Analytical(K)	Error %
100	697.381	705.5165	1.153127
200	1338.56	1354.8	1.198701
400	2430.89	2462.2	1.271627
600	3310.64	3355	1.322206
800	4016.49	4071.1	1.341406

Table 2-2: Base case results - comparison with analytical solution.

2-2 Thermal analysis of the S&A chip package

Description of the package/model:

The S&A chip is prepared on an SOI (silicon-on-insulator) wafer. This consists of a device layer and a handle layer with an insulator in between. The actuators are fabricated using DRIE on the device layer (125 microns). The handle layer is a 400 micron thick layer of silicon. The two layers are separated by a thin layer of silicon-dioxide (2 microns). The S&A chip consists of three actuators - the flow sensor, arming and the g-sensor actuator on the device layer. The device layer is attached to a top chip with indium solder joints (10 micron standoff). The handle layer is attached to the base of the kovar carrier with a gold-tin eutectic bond. A clear picture of the actual package is shown in Figure 2-5. The carrier is attached to the aluminum enclosure through a circuit board sandwiched between thermal pads. The enclosure is then bolted to the torpedo wall. The placement of the package in the enclosure was determined from the models (Pro-E) provided by Indian Head. The S&A chip package and its surroundings are shown in Figure 2-6.

A 3-D finite element model was prepared for the thermal analysis of the S&A chip package. The software used for the analysis was ANSYS 9.0. The model prepared was called the base case model and was used as a reference for several parametric studies.
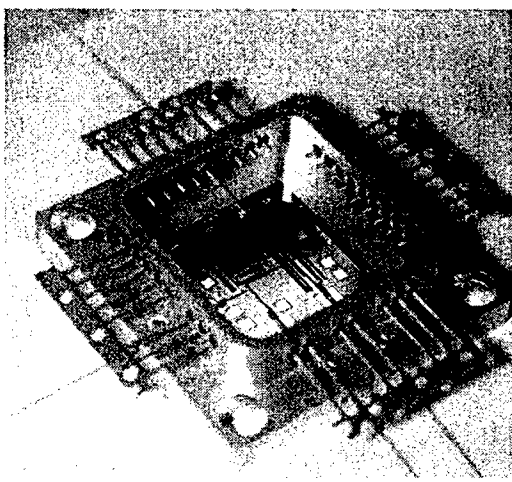
Fig. 2-5: S&A chip package without the lid
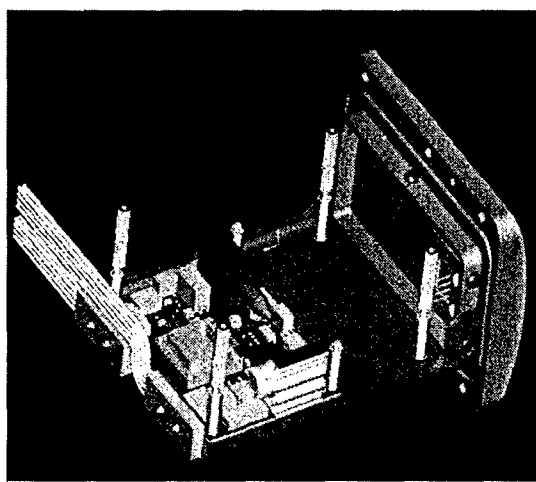

**Fig. 2-6**: S&A chip package placed in enclosure and bolted to torpedo wall
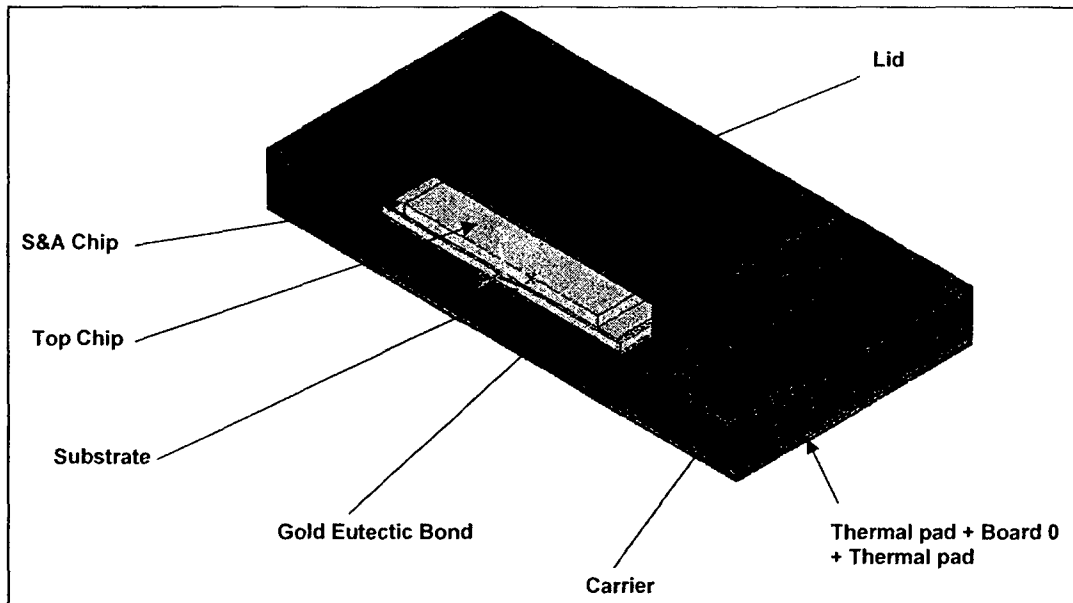
Fig. 2-7: Section view of the package

Based on the inputs provided, the base case model of the S&A chip package included the following parts.

- Lid - Kovar
- Carrier – Kovar
- Top Chip – Silicon
- S&A Chip package – Silicon
- Solder joints (Top chip)– 100In
- Chip to carrier bond – AuSn

- Thermal Pad (Thermaflo TCP – 8020TPL220)
- Aluminum fuze body
- Aluminum fuze cap

(Dimensions taken from AUTOCAD and Pro-E models sent by IHD)

The section view of the package can be seen in Figure 2-7. The 2 micron layer gap between the device layer and handle layer of the SOI wafer was included in the model in the form of a contact resistance. The effect of introducing contact elements instead of physical elements was studied using 2-D models. This was mainly done because of meshing restrictions. The results showed that the difference in the temperature profile between the two cases was less than 0.5 %. The thermal conductance of air was used as the characteristic property for the contact elements below the actuators and the thermal conductance of silicon-dioxide was used for the elements below the rest of the device layer. The thermal conductance of air also included the effect of conduction from the sides of the beam calculated in the form of a shape factor. The other parts of the package modeled as contact elements were the chip to carrier bond (Au-Sn), thermal pad, section of board zero and the conduction of heat through the air gap between the S&A chip and the top chip.
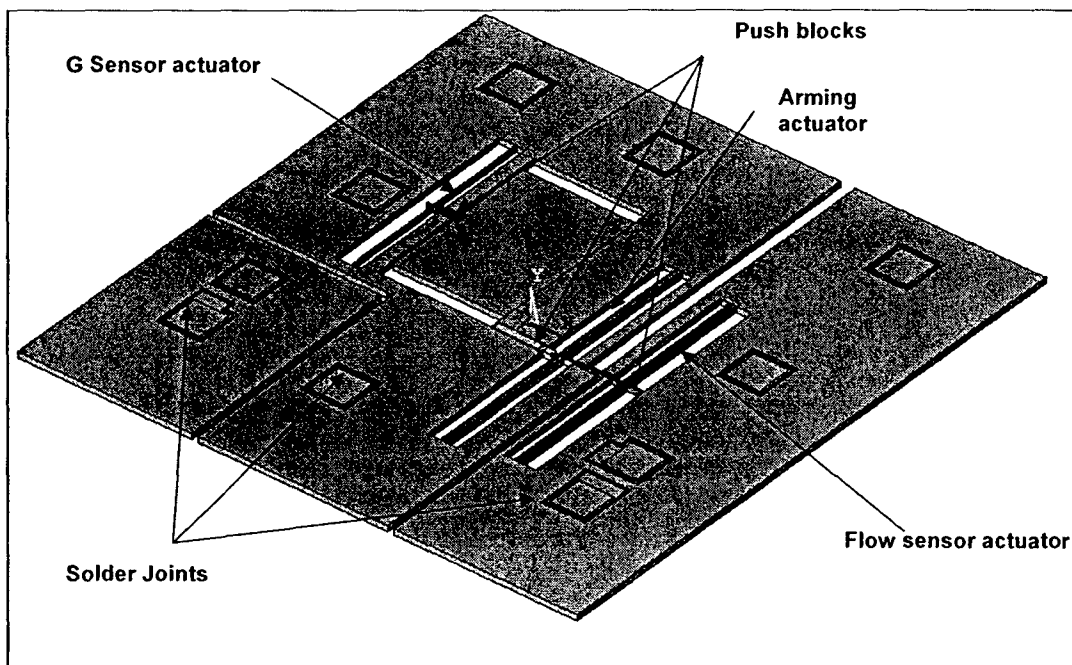
Fig. 2-8: Device layer of S&A chip with the push blocks

A push block was included in the center of the actuator beams. The heat generation was applied only in the beam portion of the actuator and not in the push blocks. This is because the push block offers very low resistance to the current passing through it compared to the rest of the beam due to the increase in cross-sectional area in that region. This results in very little joule heat generation in the push block. This was

again verified using a simple 3-D model of the actuator alone (beams with the push block) and applying a voltage difference across its ends. The joule heat generation in the push block was negligible. The push blocks in the device layer are shown in Figure 2-8.

The kovar carrier is attached to a circuit card with a thermal pad between these two components. The circuit card is mounted on an aluminum enclosure using the same material. The thermal resistance for the pads and the card are included in the model using a series of contact resistances. The aluminum enclosure is bolted to the torpedo wall (seen in Figure 2-9) which is subjected to a forced convection boundary condition. The geometry of the aluminum enclosure and torpedo wall are not modeled in detail but are approximated in a thermally equivalent manner. In reality, the aluminum fuze body is made up of two parts as shown in Figure 2-10. There is no interface material between the two parts of the fuze body. Due to this reason, the thermal contact conductance between these parts may be very low. Considering only the lower portion of the fuze body gives the worst case condition. The fuze cap in the model is not the same size as in the Pro-E models. Since the convection boundary condition is applied on the outer surface of this fuze cap, the larger area has been simulated by multiplying the heat transfer coefficient by a factor equivalent to the ratio of the actual surface area of the fuze cap to the surface area modeled for the analysis. All of these components have been included in the model to provide a representative boundary condition. The material properties used for the model are shown in Table 2-3 and the dimensions of all the parts of the model are shown in Table 2-4.
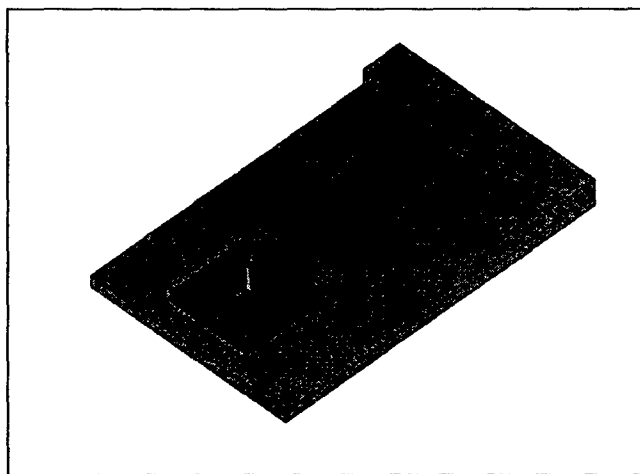
Fig. 2-9: Complete package mounted on simulated aluminum enclosure
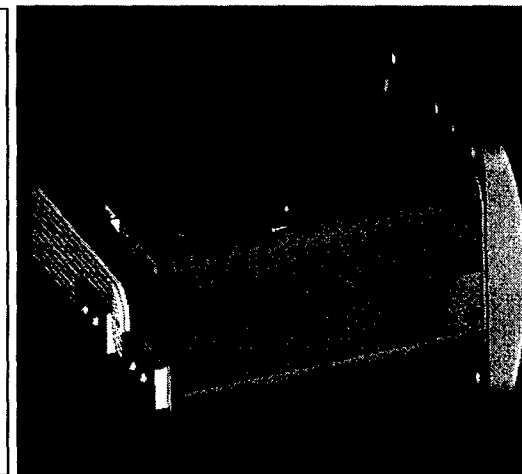
Fig. 2-10: Fuze cap and fuze body models (Pro-E models – IHD)

	Thermal Conductivity (Wm-1K-1)		Specific heat (J kg-1 K-1)	Density (kg m-3)
Silicon	T(K)	k(Wm-1k-1)	729.614	2330
	300	128.20		
	320	117.10		
	340	108.80		
	350	105.90		
	400	89.13		
	500	67.46		
	600	53.73		
	700	44.32		
	800	37.51		
	1000	28.39		
	1200	22.61		
Air	300	0.02624		
	350	0.03003		
	400	0.03365		
	450	0.03707		
	500	0.04038		
	550	0.0436		
	600	0.04659		
	650	0.04953		
	700	0.0523		
	750	0.05509		
	800	0.05779		
100 Indium	83		243	7310
Kovar	16		418	7750
Aluminum (Al6061)	180		898.7	2700
AuSn (Bond)	57		-	-
Glass (Corning7059)	1		-	-
Thermaflo TCP – 8020TPL220 pad	6		-	-

Table 2-3: Material properties of the different parts of the S&A chip package

	Length (mm)	Width (microns)	Height (microns)
Arming actuator	6	20	125
Flow sensor actuator	5.5	20	125
G-sensor actuator	4.5	20	125
	(mm)	(mm)	(microns)
S&A chip – device layer	12	12	125
S&A chip – handle layer	12.35	12.35	400
Top chip	10	10	525
Solder	.75	.75	10
	(mm)	(mm)	(mm)

Kovar carrier–Inner walls	17.7	17.7	3.11
Kovar carrier base	24.4	24.4	2.45
Gold-Tin eutectic	12.35	12.35	25.4

Table 2-4: Dimensions of different parts of the package

Boundary conditions:

The actuators are subjected to a uniform heat generation. As mentioned before, the heat generation is applied only in the beam and not in the push block.

The torpedo wall is subjected to forced convection. The value of the heat transfer coefficient used in the model is 1000 Wm^{-2}. This value was calculated based on the assumption that water flows over the surface of the torpedo wall at a speed of 1m sec^{-1}.

The power input was adjusted to get a maximum temperature of approximately 800K on the beam. This was done in ANSYS by running the analysis at a specific power level and obtaining the maximum beam temperatures. Based on whether the temperature was more than 800 K or less than 800 K, the power to the beams was adjusted accordingly. The power increments/decrements were calculated based on the relative temperature difference $(\pm \frac{800 - T_{max}}{800})$.

Other considerations in the model:

The heat is conducted from the beams and the adjacent chip area to the substrate through the 2 micron stagnant air gap and silicon-dioxide respectively. The conduction takes place not only from the bottom of the beam but also from the sides of the beam to the substrate. To account for the conduction from the sides, the conductivity was multiplied by a shape factor. The shape factors for the air gaps between the beam and the substrate were calculated from a separate 2-D model. This included a rectangular surface generating heat with an isothermal surface beneath it separated by a 2 micron air gap (as shown in Figure 11). The rectangular surface was surrounded by air on the sides also. The ratio of the heat flux from the sides and the bottom surface of the beam to that from just the bottom of the beam was used as the shape factor.
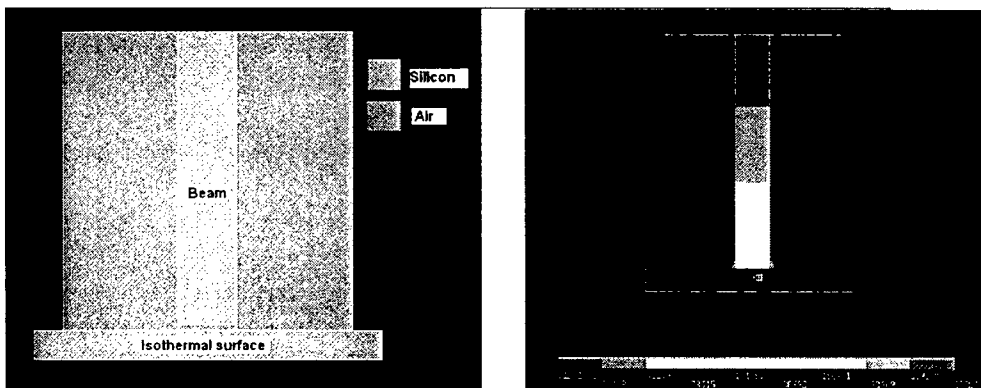

Fig. 11: 2 D model and heat flux variation to determine the shape factor for the conduction through the air gap

This was repeated for different air gaps and the results are shown in Figure 2-12. The height of the beam was considered to be 125 microns and the width was 20 microns.

Shape factor

$y = 1.1683x^{0.3554}$
$R^2 = 0.9953$

Legend:
— From FEA model
— Power (From FEA model)

X-axis: Gap between the beam and isothermal surface (microns)
Y-axis: Shape factor
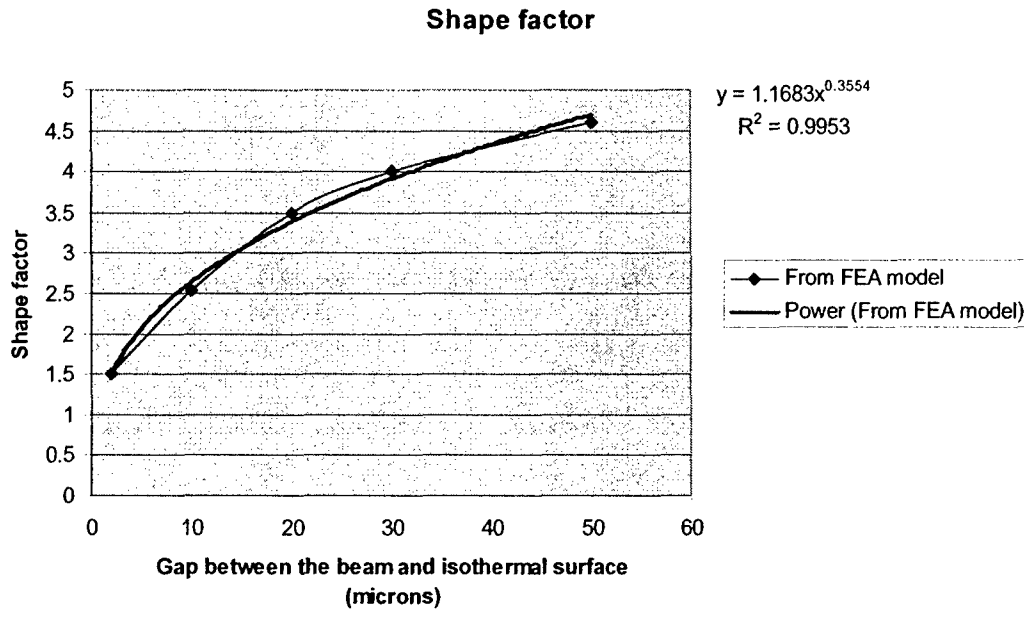
Fig. 2-12: Variation of shape factor with gap thickness between the beam and the isothermal surface

The model does not include radiation effects on the chip since these effects were found to be insignificant (of the order of 0.1 K). This was done by applying surface to surface radiation on the sides of the beam and the adjacent surface of the chip (as shown in Figure 2-13), since this is where the maximum temperature difference exists. The maximum temperature of the beam was reduced by 0.1 K by applying radiation in the above defined manner.

Natural convection has not been included. The Rayleigh number for this model was calculated to be of the order of 10^{-7}. The natural convection, for Rayleigh numbers of this order, is very small and hence neglected.

A mesh convergence study was performed for the S&A chip and other parts of the package including the substrate and the top chip. A close check was maintained on the beam temperatures while varying the mesh of the various parts of the package. Based on the results, an optimal mesh was chosen for the model. The mesh convergence study results can be seen in the Figure 14.

Surface to surface radiation applied on the
sides of the beam and adjacent silicon
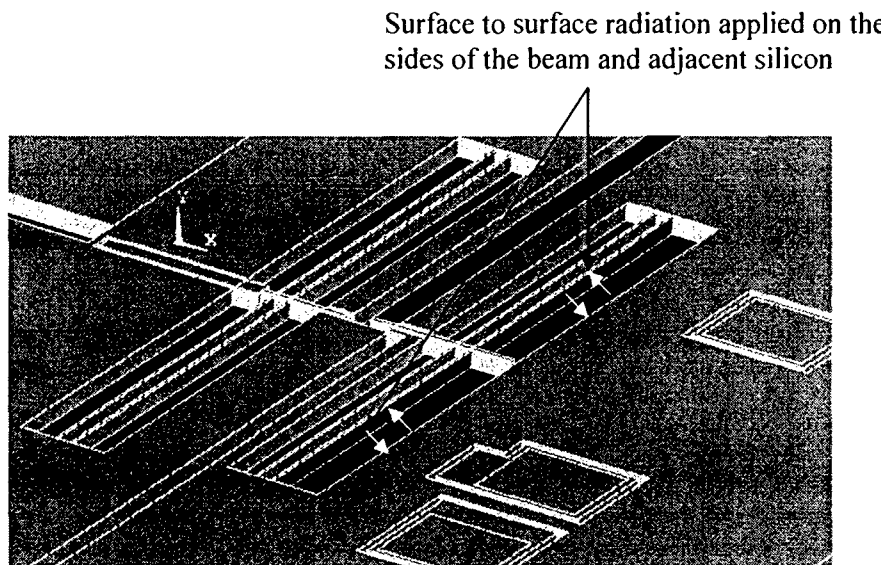
Fig. 2-13: Radiation applied to the surface of the beam and the adjacent silicon surface
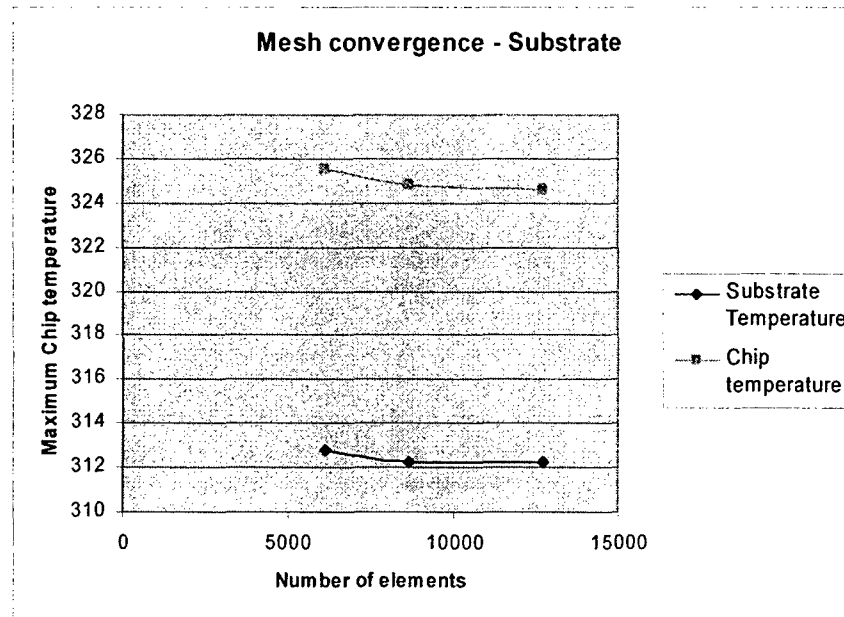
Fig. 2-14: Mesh convergence study of the S&A chip

A transient analysis was performed on the model. An automatic time step was used in ANSYS for the iterations. This means that the time step varied based on the performance of the system. As the system started reaching steady state, the time step increased. The minimum time step used was 1 second. For the current simulation, the areas of the package shown below reach a steady state in approximately 400s (as shown in Figure 2-15). The temperature contours, shown later in the report, are for a steady state condition.

Temperature (K)

Time (seconds)
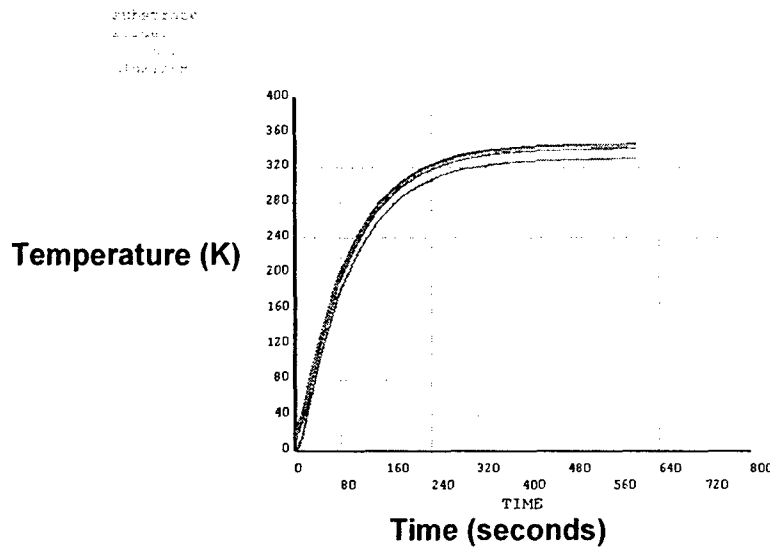
Fig. 2-15: Variation of temperature (different parts of package) with time

The effect of forced convection is significant since the surface area exposed to the water is relatively large. These effects can be seen clearly in Figure 2-16. The convection heat transfer coefficient used in the model is 1000 $Wm^{-2}K^{-1}$. This value is suitable for a water velocity of approximately 1 m sec^{-1}. The temperature of the water was assumed to be 35 degrees C (308 K).
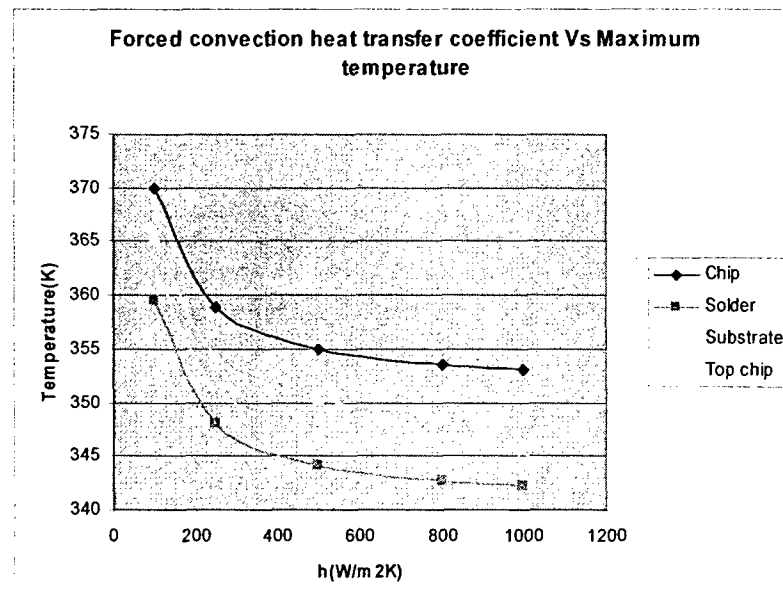
Fig. 16: Effect of forced convection heat transfer coefficient on maximum temperature of S&A package

Temperature contours of the package:

Figure 2-17 shows the temperature contours on the S&A chip. It can clearly be seen that the actuators reach the desired temperature for the chosen power. The maximum temperature occurs not in the center of the beam but between the push block and the end of the beam as seen in an actual powered beam. This is because of the high heat generation in the beams compared to the push block. Also, the push block has more surface area for heat transfer through the stagnant air layer relative to the heat generation, compared to the beam. The maximum temperature as shown in the profile is 801.5 K.
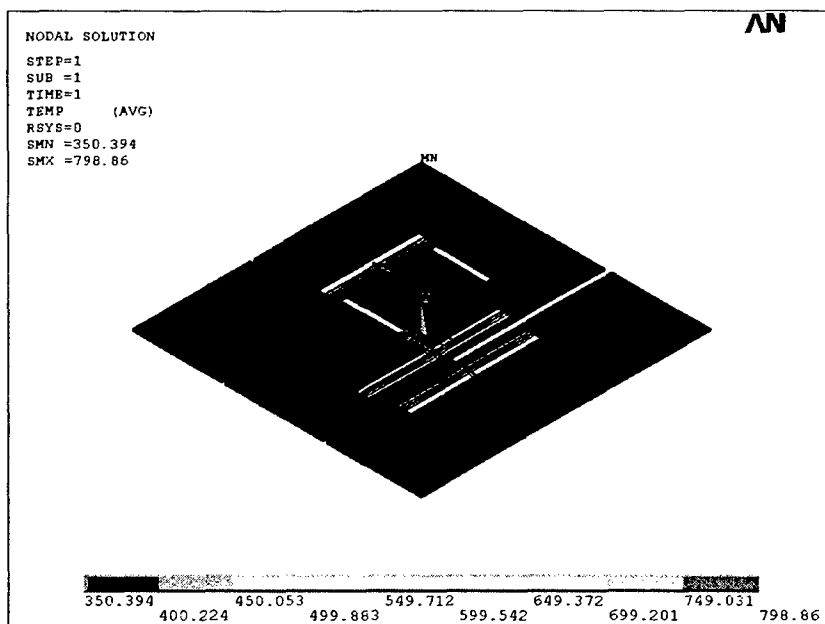
Fig. 2-17: Temperature contours of the S&A chip including the actuators

Figure 2-18 shows the temperature distribution in the remainder of the S&A chip more clearly since the actuators were excluded. The higher temperatures, as expected, are in the portion of the chip surrounding the arming and flow sensor actuators, since the two actuators are adjacent to each other and the power density is higher than for the g-sensor area.
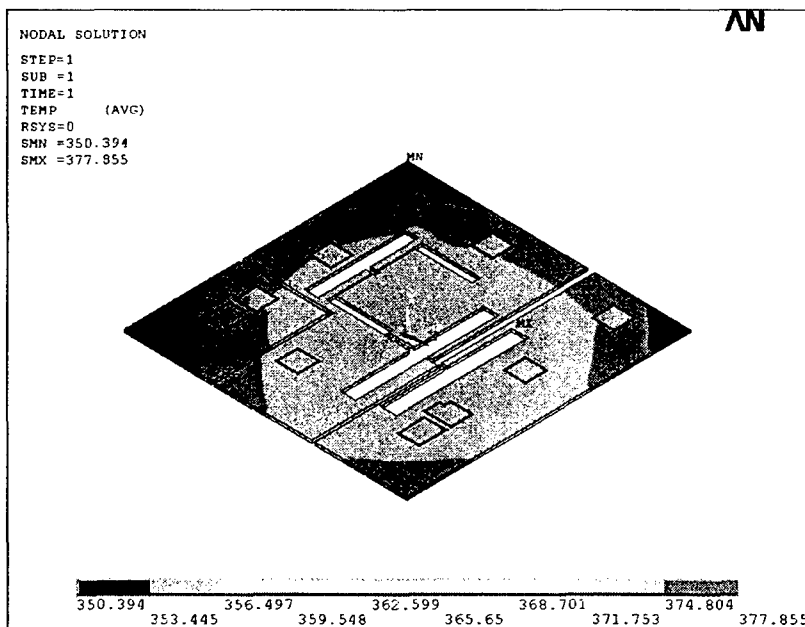
Fig. 2-18: Temperature contours of the S&A chip excluding the actuators

The silicon-dioxide and the air beneath the S&A chip transfers the heat to the substrate. The substrate temperatures rise by approximately 50 degrees. The temperature distribution is similar to that of the S&A chip. This is shown in Figure 2-19. The maximum temperatures occur right below the flow and arming actuators.
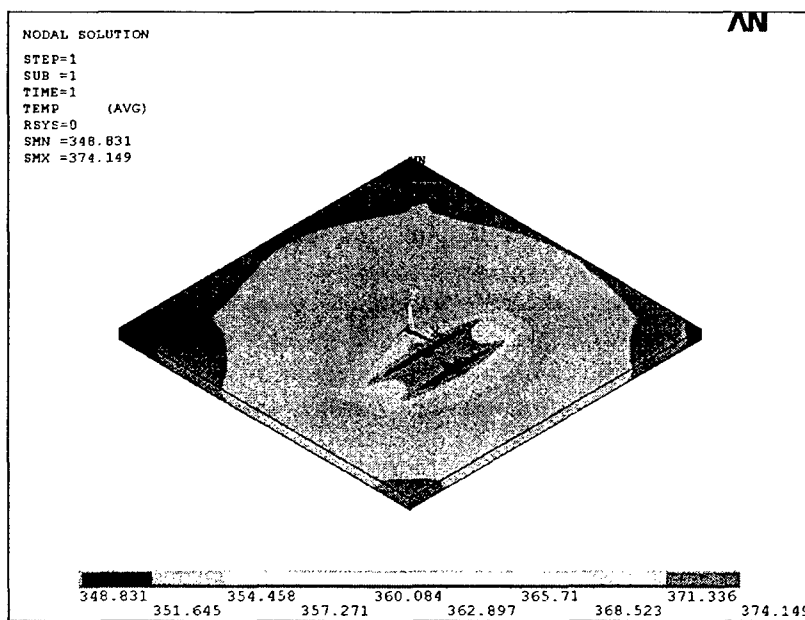
Fig. 2-19: Temperature contours of the substrate

The solder joints near the flow sensor and the arming actuators reach the highest temperatures (shown in Figure 2-20). The maximum temperature of the solder joints is 350 K, i.e. 42 degrees higher than the initial temperature. However, this temperature is not high enough to melt the solder joints (melting point of Indium, 423 K).


```
NODAL SOLUTION                                              AN
STEP=1
SUB =1
TIME=1
TEMP        (AVG)
RSYS=0
SMN =355
SMX =362.856
```
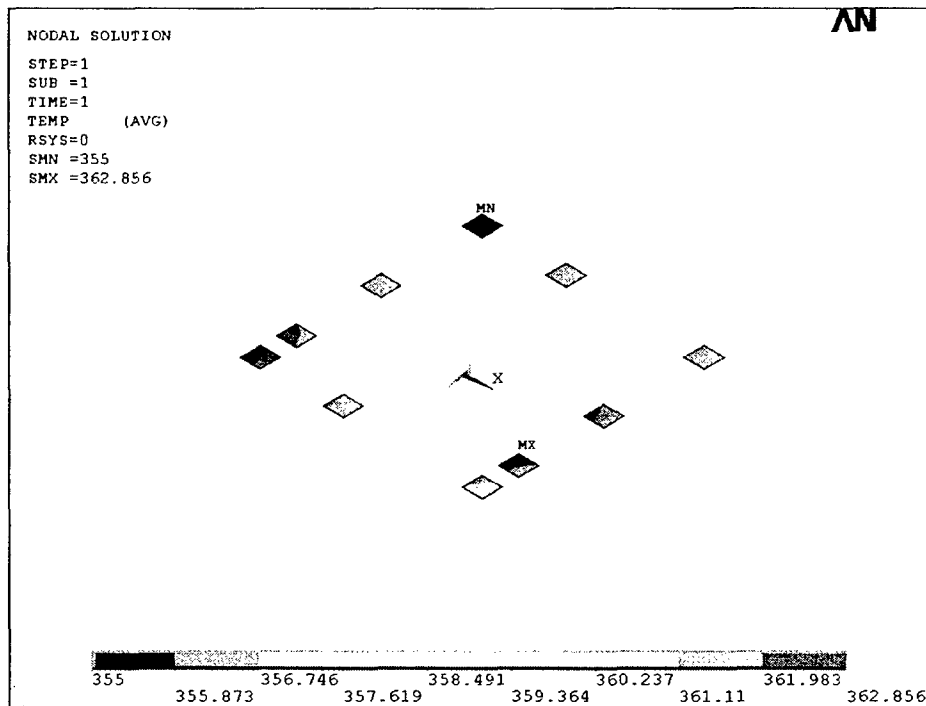
Fig. 2-20: Temperature contours of the solder joints

Figure 2-21 shows the temperature contours of the top chip which is made of silicon in the base case. This is a view of the bottom surface of the top chip which faces the S&A chip and is connected to it through the solder joints. The heat conduction is therefore mainly through the solder. The other form of heat transfer to the top chip is through the air present between the top chip and the device layer of the S&A chip. This distance is the same as the solder height (10 microns). The highest temperatures are therefore in the portion right above the actuator beams. The maximum temperature (353 K) is however less than that of the substrate (357 K). This is because of the presence of a larger air gap (10 microns) between the S&A chip and the top chip compared to the substrate (2 microns).
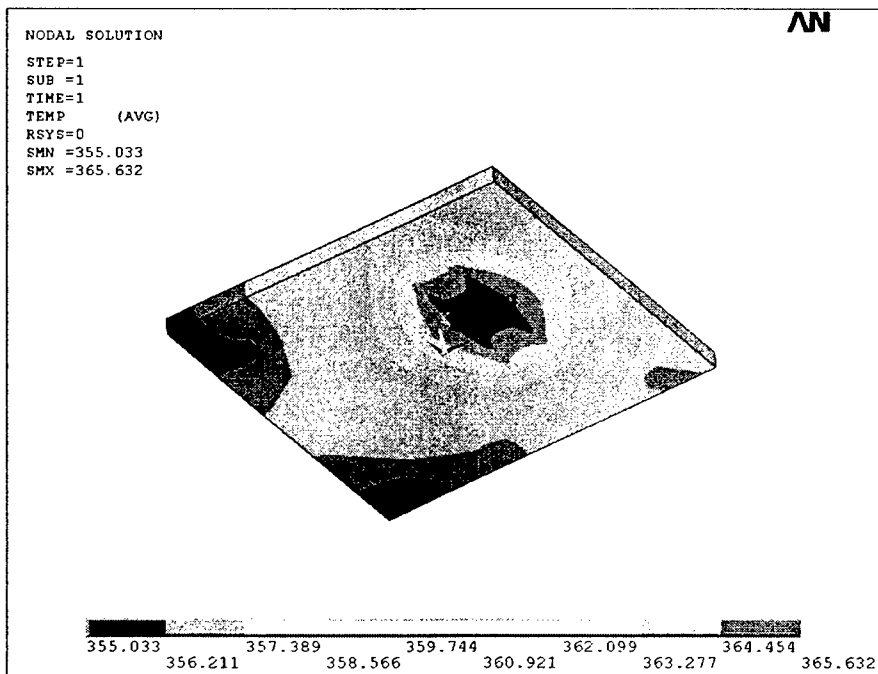
Fig. 2-21: Temperature contours of the top chip

The maximum temperature on the kovar base occurs below the flow and arming actuator. The heat spreading in the base is relatively limited due to the low thermal conductivity of the kovar.
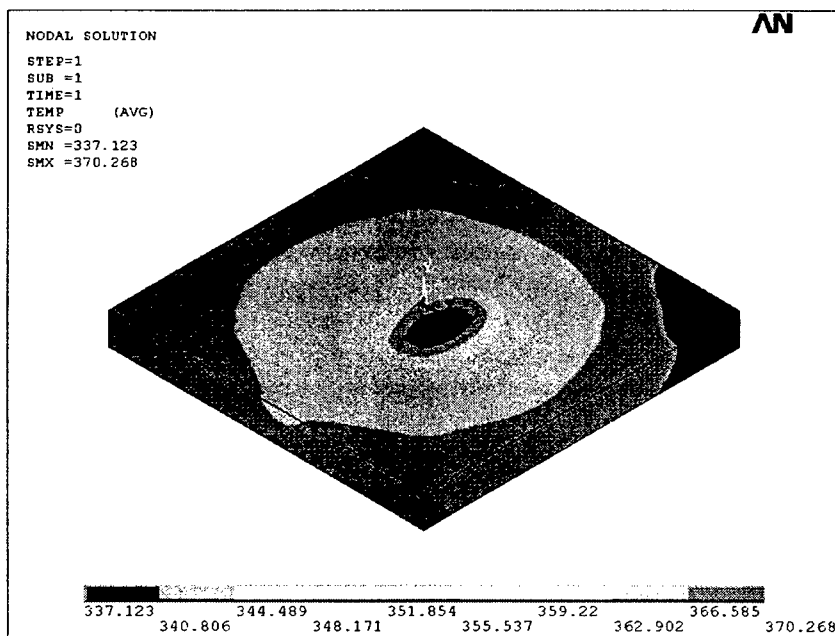
Figure 2-22: Temperature contours of the kovar carrier base

The temperature profile of the aluminum plate/enclosure is shown in Figure 2-23. The end where the S&A package is located is the hottest portion. The forced convection condition is applied on the fuze cap, which is the other end of the plate. The difference in the maximum temperature on the aluminum plate and the kovar carrier is due to the presence of the thermal pads and board zero, which offer considerable resistance to heat flow.
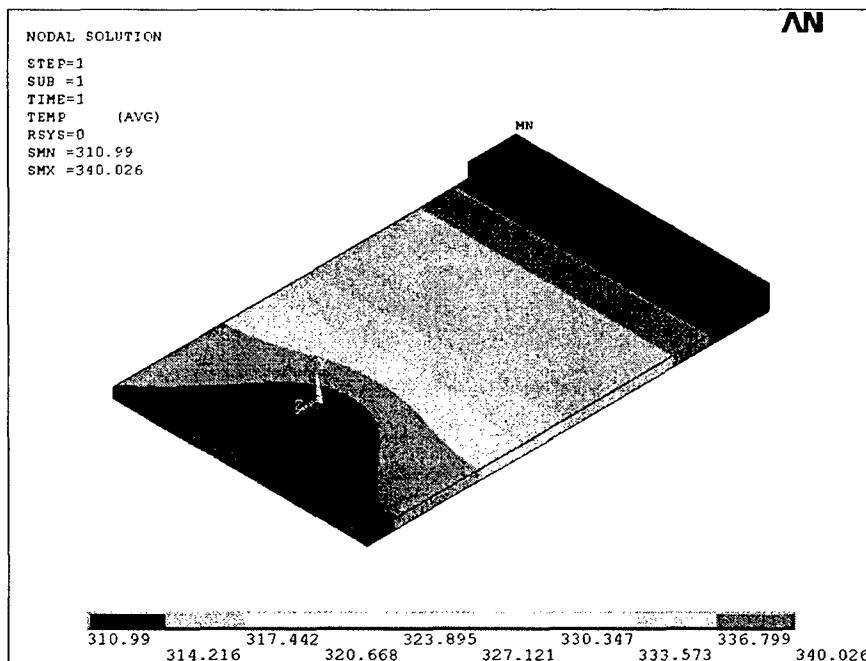

Fig. 2-23: Temperature contours of the aluminum fuze body

2-3. Parametric studies

The S&A chip requires relatively high power for the actuators to achieve the necessary displacement. The objective of the parametric studies was to quantify the power reduction allowed by various design changes while still maintaining a maximum beam temperature of 800 K.

Effect of silicon dioxide thickness:

The main path of heat transfer is from the beam to the substrate. The device layer and the handle layer of the S&A chip are separated by a layer of silicon-dioxide. Changing the thickness of this layer changes the thickness of the stagnant air layer below the beam. The effect of increasing the thickness of the oxide layer is seen in Figure 2-24. The gap between the base of the beam and the substrate was varied from 2 microns (used in base case model) to 4 microns. The results are shown as the power required per beam of the actuator to reach a maximum temperature of 800K as a function of the gap. An increase in the oxide thickness decreased the power by a moderate amount. This decrease is due to

the fact that the main conduction path for the heat from the beam is down through the air gap to the substrate. The shape factors for the respective gap thicknesses have been included in the calculation. The power requirement is reduced considerably (.15 Watts per beam) for an increase of 1 micron in the gap. However the effect tends to reduce as the gap is increased to 4 microns.

Power required per beam of the actuator vs silicon dioxide thickness
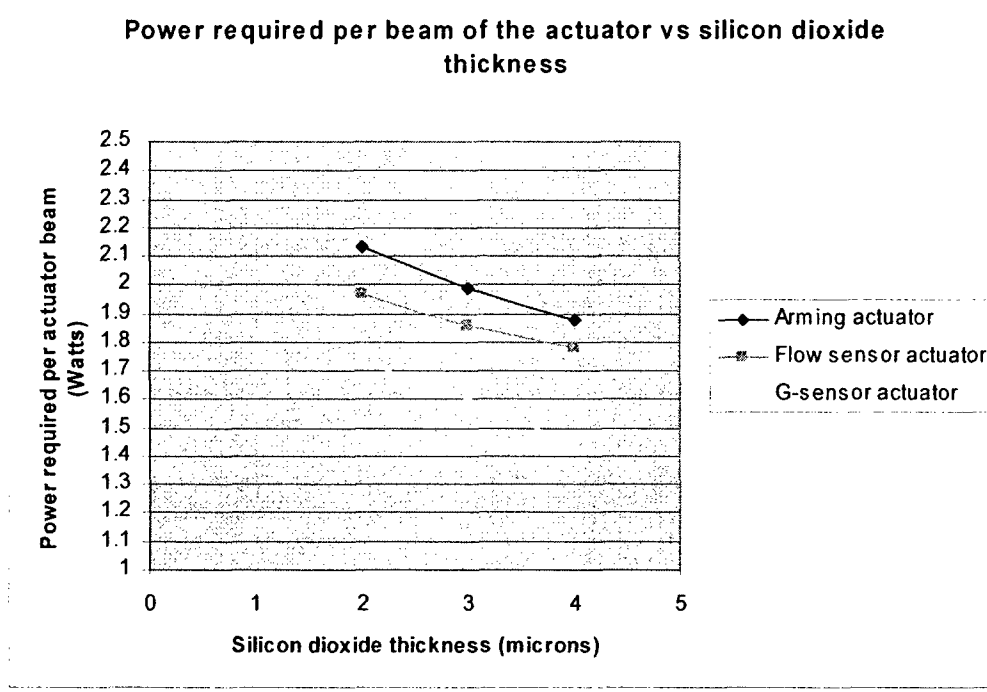
Fig. 2-24: Effect of silicon-dioxide thickness on the actuator power requirements

Effect of top chip material:

The top chip in the base case was considered to be made of silicon. However, by changing the top chip to glass, the power required to reach a maximum beam temperature of 800 K was less than that required for the silicon top chip. The power requirements for the three actuators for both top chip materials are shown in Table 2-5. The conductivity of glass was considered to be 1 W m^{-1} K^{-1}. As the conductivity of the top chip is reduced, less heat is transferred from the S&A chip to the top chip, since it offers a higher resistance. This allows the actuators to reach the desired temperature for a smaller power input. The glass top chip reduces the power requirements per beam of the actuator by 0.1 Watt compared to that required for a silicon top chip.

	Power required per beam of the actuator in Watts		
Type of top chip material	Flow	Arming	G-sensor
Silicon	1.95	2.1	1.71
Glass	1.81	2	1.65

Table 2-5: Power requirements to reach a maximum beam temperature of 800K for top chips made of silicon and glass

The above method was repeated for a range of thermal conductivities to study the relative effect of the top chip material. The results are shown in Figure 2-25. The power requirements do not change considerably for the thermal conductivities in the range $20 - 150$ W m^{-1} K^{-1}. The reduction can be seen only in the range of $1 - 20$ W m^{-1} K^{-1}.
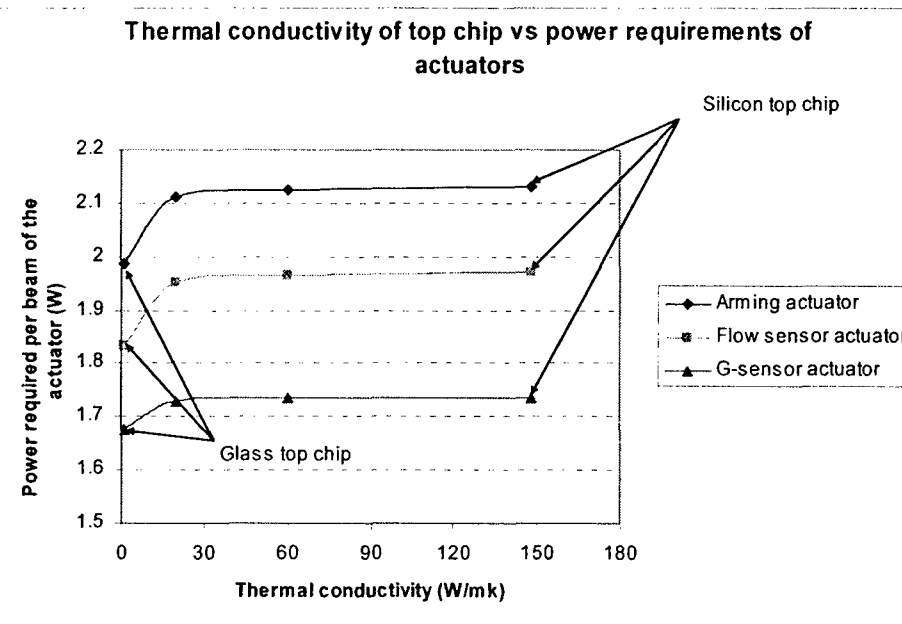
Fig. 2-25: Variation of actuator power requirements with top chip thermal conductivity

Effect of relief cuts in the top chip:

To increase the beam's thermal isolation, relief cuts are being considered in the top chip. The effect of these relief cuts has been modeled based on the dimensions provided by Indian Head (see Figure 2-26). The power required to maintain the beam's maximum temperature at 800K was determined using an algorithm to adjust the power input based on the resulting beam temperature. The power requirements for various relief

cut depths for both silicon and glass top chips are shown in Figure 2-27. The plot shows the relative benefit as the relief cut depth increases.
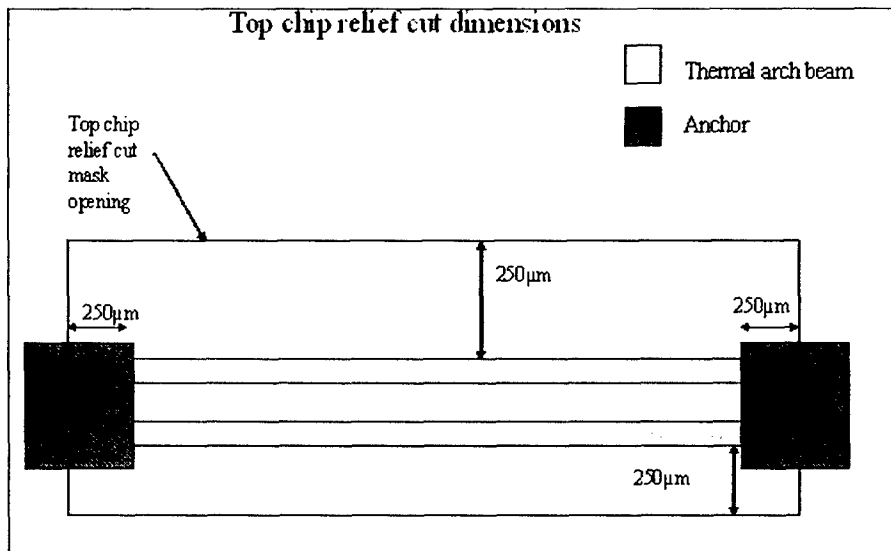
Fig. 2-26: Top chip relief cut dimensions

As the relief cut depth in the top chip increases, the resistance to the heat path through the air gap between the beam and the top chip is increased. The shape factor increases with the air gap, however, the decrease in the conductance is much higher. Hence, less heat is transferred from the beam to the top chip which reduces the power requirements. As the cut depth increases the relative decrease in the power reduces for a given increment.
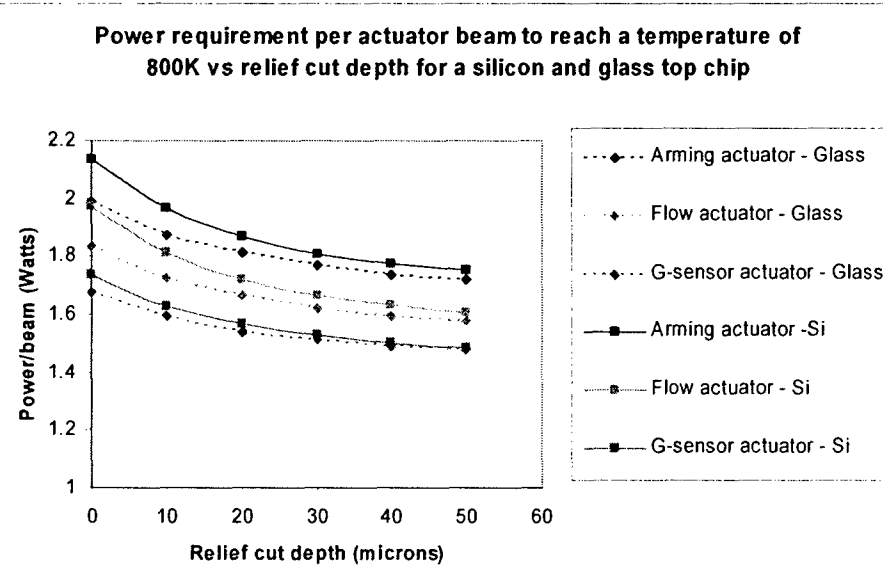
Fig. 27: Power requirement per beam varying with relief cut depth for silicon and glass top chip

Effect of relief cuts in the substrate:

The relief-cut dimensions for the substrate, provided by Indian Head (seen in Figure 2-28), were included in the model and the depth was varied from 10 microns to 50 microns. The base case model assumptions and boundary conditions were used and the relevant shape factors to account for the conduction from the sides of the beam were included. The power input to the actuator beams was adjusted such that a maximum temperature of 800K was attained on the beam. Since the main path of heat loss from the beam is through the air beneath it to the substrate, the cut depth has a large effect on the power required for the beam. This can be seen in Figure 2-29.
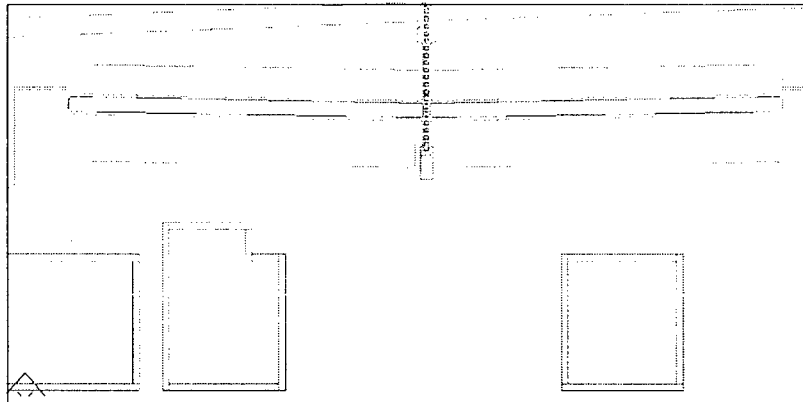
Fig. 2-28: Substrate relief cut dimensions
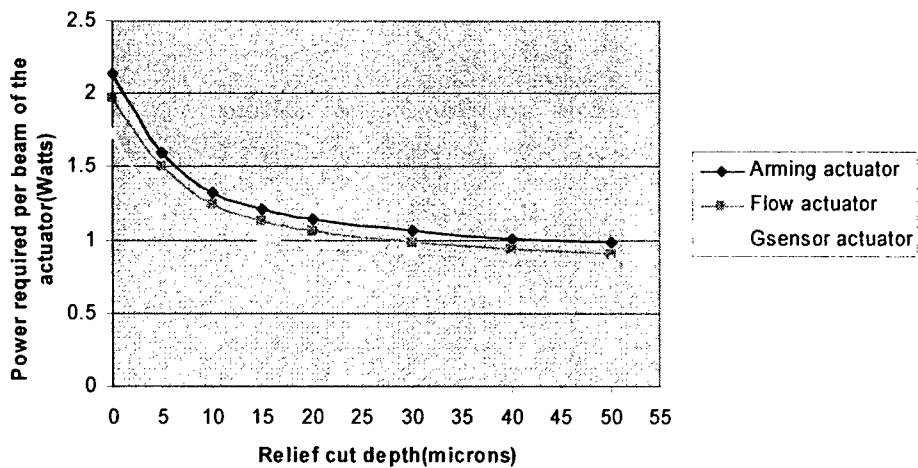
Fig. 2-29: Power requirement per beam varying with relief cut depth in silicon substrate

As the relief cut depth increases, the power required for the actuator beams to maintain 800K reduces. From Figure 2-19 it can be seen that after a relief cut depth of 10 microns, the reduction in the power for a given depth increment decreases. The maximum reduction occurs between no relief cut and a relief cut depth of 5 microns.

**Observations and Conclusions:**

The S&A chip package has been modeled in detail. The temperature distribution for the whole package was obtained. Methods to decrease the power requirements to the actuators have been studied. This included parametric studies of potential design changes to the S&A chip package.

Increasing the silicon dioxide thickness resulted in decreasing the power required to maintain the actuator temperature at 800K. Increasing the gap to 3 microns resulted in a reduction of 0.2 Watts per beam of the actuator and a subsequent increase in the depth by another micron resulted in further reduction of approximately 0.1 Watt.

The glass top chip proved to be better in reducing the power requirements for the actuators when compared to the silicon top chip. The power requirement for the glass top chip was 0.1 Watt less than the silicon top chip per beam of the actuator.

Relief cuts in the top chip and substrate reduced the power requirements for the actuators. As the cut depth increased, the incremental reduction in the power decreased. The relief cuts in the substrate had a larger effect on the power reduction compared to those on the top chip since the heat conduction path to the substrate is a lower resistance path. The power reduction was as high as 1.1 Watts per beam of the actuator when the relief cut in the substrate was 50 microns. In the case of relief cuts in the top chip, the highest reduction in power was approximately 0.3 Watt per beam of the actuator.

2-4 Computational fluid dynamics model

Numerical modeling of the package – description:

A computational fluid dynamics model of the package was prepared to determine the air pressure and temperature inside the package. The CFD model is similar to the finite element thermal model with a few minor changes. The push blocks were not included in the model of the S&A chip. The aluminum block and torpedo wall were not included in the model, but are approximated in a thermally equivalent manner for a static analysis. This was done by adjusting the heat transfer coefficient in such a manner that it includes the resistance to heat conduction through the aluminum plate and the torpedo wall. The model (shown in Figure 2-30) was built using FLUENT 6.1 software. The material properties are the same as used in the finite element thermal model.
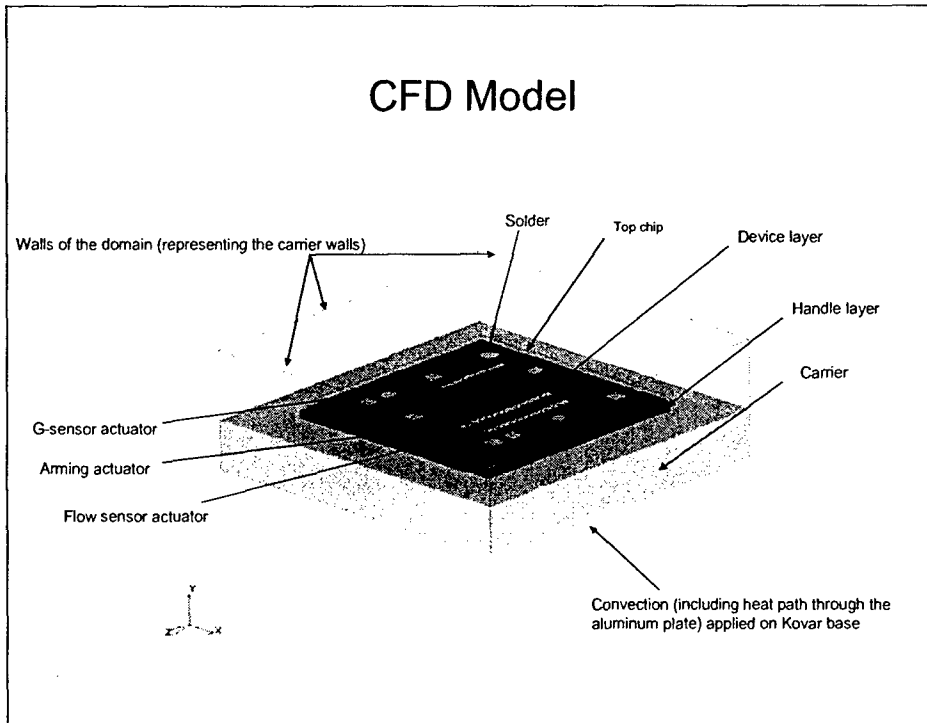
Fig. 2-30: Package model in FLUENT

Temperature of air at the surface of kovar carrier and the lid:

The temperature at the perimeter of the air volume is shown in Figure 2-31. The highest temperature (321 K) of the air on this surface, i.e., in contact with the lid, occurs above the beams. The air temperature averaged over the entire cavity in the package is 317 K.
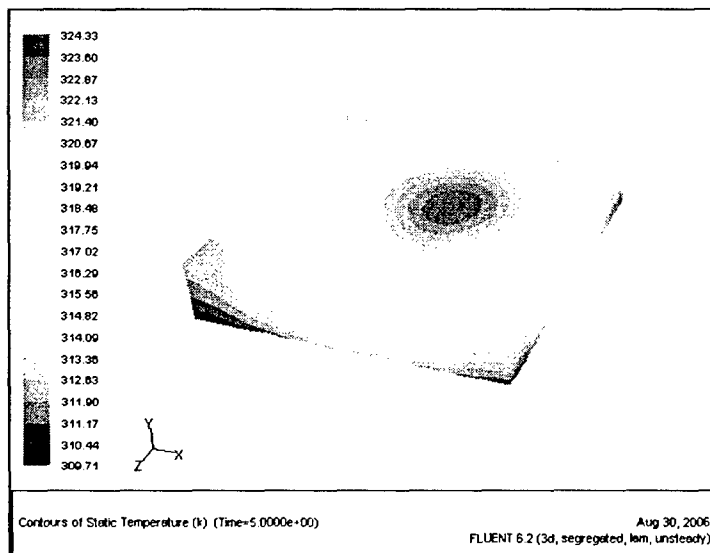
Fig. 2-31: Temperature of the air at the perimeter of the air volume inside the package.

Temperature of air inside the package:

The highest temperature of air inside the package is the same as the temperature of the beam, since this air is adjacent to the beam. The maximum temperature can be seen in Figure 2-32. The average temperature is calculated by FLUENT using a volume–averaged method. The hot air is restricted from reaching the top of the package, since the top chip absorbs the heat from the beams. The conduction path from the top chip through the solder joints to the S&A chip is a lower resistance pathway when compared to the natural convection on the surface of the top chip. Therefore, the upper surface of the air does not reach a high temperature as seen in the previous figure (Figure 31 – 321 K).
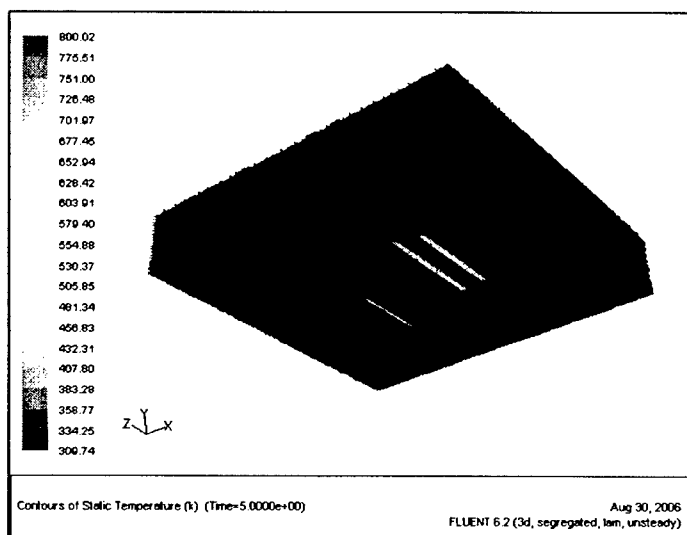
Fig. 2-32: Temperature contours of air inside the package – base of the package.

Pressure of air inside the package:

The pressure of the air inside the package rises gradually as the temperature of air increases with time. The pressure of the air was approximately 3000 Pa (0.03 atm) higher than the initial pressure, when the system reached a steady state condition as seen in Figure 2-33. The analysis was performed with the assumption that the fluid (air) is a compressible ideal gas.

104303.20
104303.20
104303.19
104303.19
104303.18
104303.18
104303.17
104303.17
104303.16
104303.16
104303.16
104303.16
104303.16
104303.15
104303.15
104303.14
104303.14
104303.13
104303.13
104303.13
104303.13
104303.13

Contours of Absolute Pressure (pascal) (Time=5.0000e+00)   Aug 31, 2006
FLUENT 6.2 (3d, segregated, lam, unsteady)
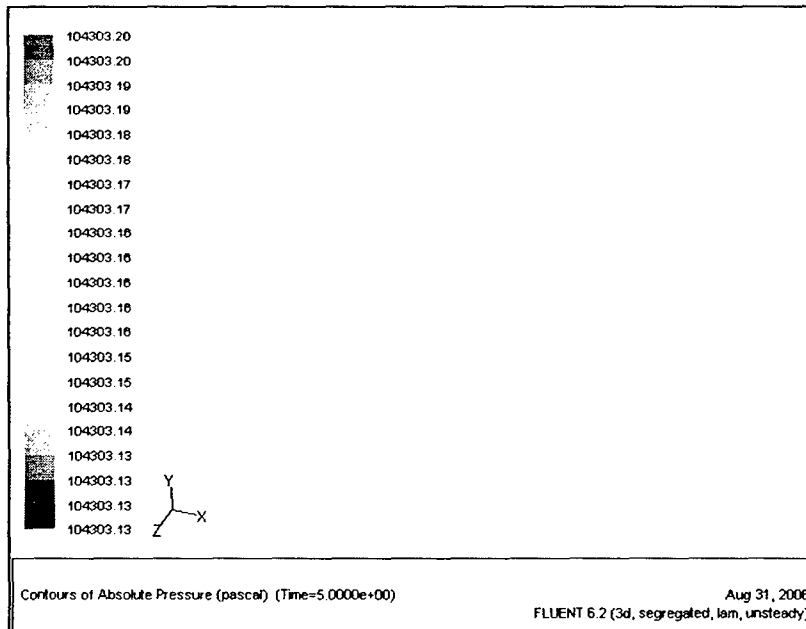
Fig. 2-33: Pressure contours of air inside the package.

Velocity profiles of air inside the package:

The air adjacent to the beams rises when the temperature increases and forms plumes above the beams due to natural convection. The magnitudes of the velocities are small since the space above the beams is very small. The maximum velocities are seen along the edges of the top chip and the S&A chip. The air between the S&A chip and the top chip moves at a very low velocity due to the restriction in space. However, as it reaches the lateral end of the chip, there is much more space for the air plume to spread. The air velocities increase in this region. This can be seen in Figures 34 a, b and c.

Conclusions:

The absolute pressure of the package goes up by approximately 3000 Pa (0.03 atm). This is an overall pressure rise of air inside the package. The pressure value agrees with that which would be calculated by the ideal gas law with the average temperature values obtained from the model.

The average temperature of the air inside the package goes up approximately $9°$. The volume of air is large compared to the localized heating of the air above the beams, which results in a lower average temperature.
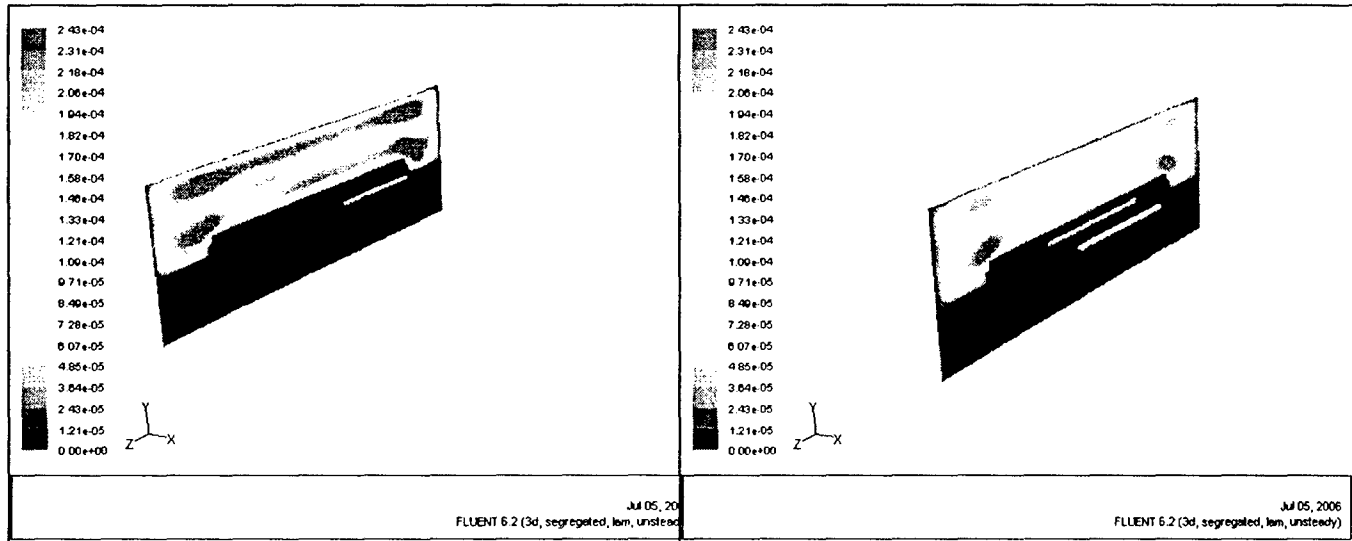
Fig. 34 a: Velocity profile formed at g-sensor actuator   Fig. 34 b: Velocity profile formed at arming actuator
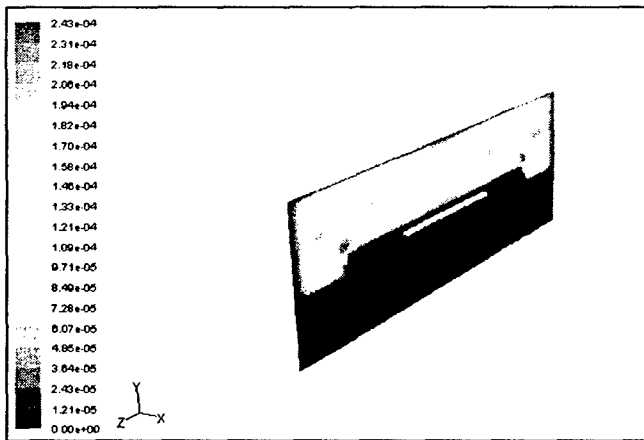
Fig. 34 c: Velocity profile formed at the flow sensor actuator

2-5 Experimental measurements:

The objective of this study was to obtain a temperature profile of the chip and to validate the finite element model.

Procedure

The temperature profile of the S&A chip was captured by the use of an Infrared camera. The emissivity of silicon was given as a constant input to the camera. A telescopic lens was used to capture the image of the S&A chip alone.

Calibration of emissivity of silicon

A silicon chip consisting of only actuators, excluding the package, was heated on a hot plate from room temperature to 200° C. The temperature of the chip was monitored

using a K-type thermocouple attached to the chip. The emissivity of silicon in the camera was adjusted until the temperature matched with the thermocouple reading.

Powering the S&A chip

The wire bonded S&A chip consisting of two flow sensor actuators, two arming actuators and one g-sensor actuator, was powered using a DC power supply. The package was not covered with the lid to facilitate the viewing through the IR camera.

Experimental Setup

The package was placed on a cold plate maintained at 20° C. This was done to maintain an isothermal boundary condition. A thermal paste was applied to increase the uniformity in the thermal resistance between the package and the cold plate as seen in the Figure 2-27.
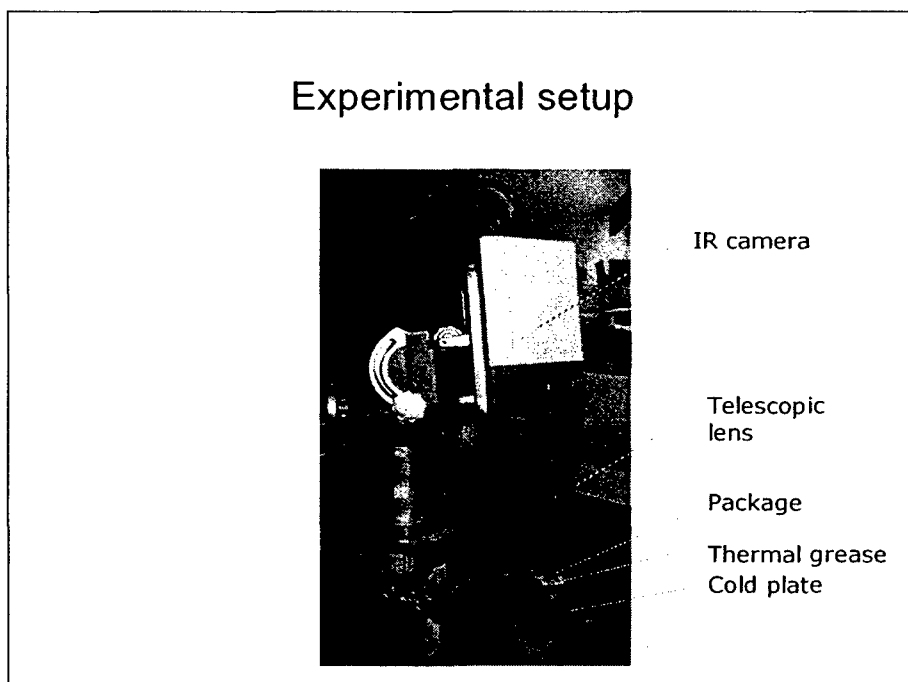
Fig. 2-27: Setup for the experiment

Finite element model

A few changes were made to the base case model based on the experimental setup.

The top chip was not included in the model since the part did not have a top chip. The package was placed on a cold plate. The same was represented in the thermal model by an isothermal boundary condition at the bottom surface of the kovar carrier with a thermal resistance accounting for the thermal paste between the package and the cold plate surface. Natural convection was included in the model on the walls of the carrier and the surface of the device layer of the chip since the experiment was carried out without the lid.

The power in the chip is not applied directly across the ends of the actuator beams in the experiment. The path from the pads to the beams offers a resistance to the current. This allows some of the power to be dissipated in this region. The power dissipated was calculated based on the resistivity values of the silicon determined experimentally. Since the resistivity is temperature dependent, the temperature was chosen based on the approximate temperature reached by the device layer of the chip in the base case model. This amount of power was deducted from the power being supplied to the actuator beams and was supplied to the adjacent area.

Averaging technique

The temperature on the actuator was captured using the "point" option in the IR camera. This option enables the user to pick any point on the screen and displays the temperature of the chosen location (pixel). The pixel size for this case was 50 microns.

The temperature read by the camera is an area-averaged temperature over 5 pixels which is calculated to be an area of 250 x 250 microns. Since the actuator beams are only 20 microns wide, the temperature is averaged with the area surrounding the silicon. The actuator beams are surrounded by air and hence the IR camera reads the temperature of the substrate silicon beneath the device layer.

The same procedure is adopted to calculate an area averaged temperature from the FEA model. The temperatures from both methods for two different power levels and the respective power levels are shown in Table 2-6 and Table 2-7. The 250 x 250 micron area to be considered consists of the actuator beams and the silicon substrate beneath as shown in the Figure 2-28.
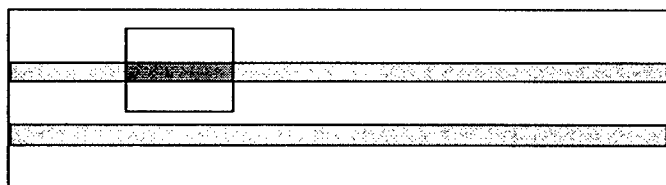
Fig. 2-28: Averaging area around the beam

Power level 1	Arming	Flow	G-sensor
FEA model	367	370	378
IR	356	355	373
Power level 2	Arming	Flow	G-sensor
FEA model	380	370	373
IR	377	355	368

Power level	Arming	Flow	G-sensor
1	1.66	1.4	1.08
2	2.325	1.4	.875

Table 2-6: Averaged temperatures from the FEA model and the IR camera

Table 2-7: Power input to the actuators.

Temperature contours from the IR camera

The temperature contours on the S&A chip can be seen in Figure 29. The picture on the left is the image from the IR camera. The temperature shown is an area averaged temperature as explained in the previous section. The maximum temperature occurs in the portion between the push block and the anchor end of the actuator beam similar to the contour from the FEA model. The push block is at a lower temperature compared to the maximum temperature. The picture on the right is the temperature contour from the FEA model. However the temperatures shown are nodal temperatures. As seen in the picture the rest of the chip is at a lower temperature.
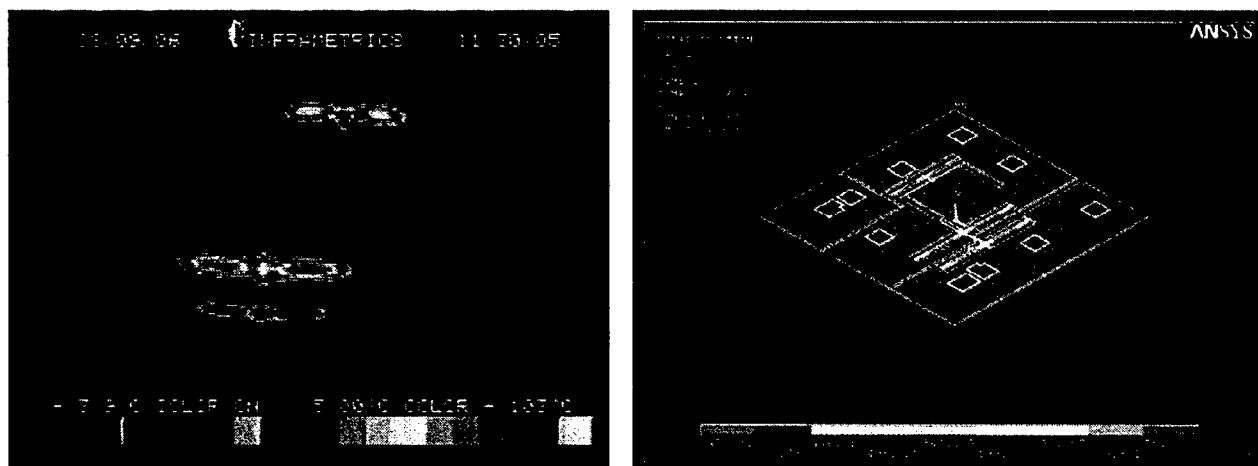
Fig. 2-29: Comparison of temperature contours from the IR camera (left) and the FEA model (right)
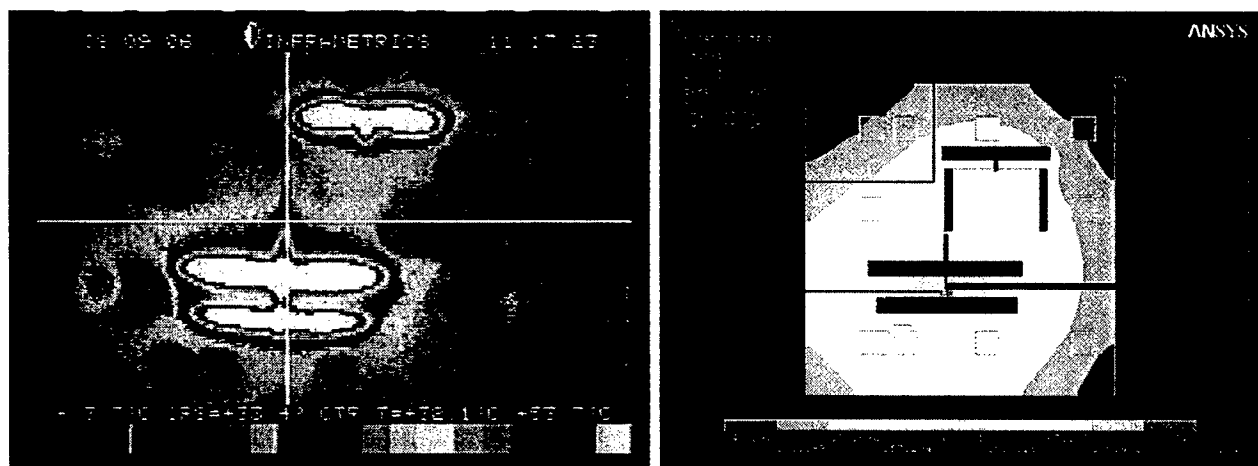
Fig. 2-30: Temperature contours excluding the actuators. IR camera (left) and FEA model (right)

Figure 3-30 shows the temperature contours on the S&A chip excluding the actuators. In the case of the IR camera, this was done by decreasing the range of the temperature such that the maximum temperature (occurring on the beam) falls out of range. This allows for the thermal gradient to be seen in the rest of the chip. The solder joints on the chip in the picture appear to be colder than the rest of the chip. This is due to the fact that the emissivity in the IR camera is calibrated to that of silicon and not indium. Hence the temperature shown by the IR camera for the solder does not reflect the actual temperature.

Conclusions

The following conclusions were drawn based on the results seen from the IR measurements.

o Reasonably good agreement has been obtained between the experimental measurements and the finite element model.

o The temperatures calculated by the averaging technique are quite sensitive to the specific area chosen in the model and are therefore subject to error.

o Good agreement has been obtained for the overall temperature contours.

o These results give confidence in the trends provided by the parametric studies.

2-6 Future work

The power required for the actuators to reach 800 K is still relatively high. Different ways of achieving the purpose of reducing the power requirement can be studied. One of the ways to do this is to alter the shape/contour of the beam to achieve the same displacement at lower temperatures and hence lower power inputs. Better thermal isolation of the beam can also be investigated.

The temperature of the beam is not known accurately. Hence, the thermo-mechanical behavior of the silicon beams is difficult to be verified. Non-contact surface measurements can be investigated further to accurately determine the temperature of the actuator.

Further parametric studies can be carried out for the different parts of the package. These parametric studies can include the dimensions or the material properties of the package.

Sub Task 3: Shock/Vibration Durability

Performer: Mohammad I Younis, James Pitarresi, Dan Jordy
Organization: SUNY Binghamton

3-1 Dynamic Durability Modeling

This report serves to document our progress including the modeling and simulation of the optical fiber, thermal actuator, and G-sensor.

3-1-1 Optical Fiber – Cantilevered Beam

Some approximations have been taken during the analysis of the optical fibers. First, ideal fixed-free boundary conditions were assumed to exist, however in reality that may not be true [1]. Variations in material properties, due to fabrication conditions, have been neglected. The assumed properties are shown in Table 3-1.

Silica (SiO_2)
- Length = 4000 μm [1]
- Diameter = 125 μm [1]
- Density = 2196 kg/m3 [1]
- Modulus of Elasticity =72 GPA [2] [3]
- Poisson's Ratio = 0.16 [2] [3]
- Yield Strength= 8.4 GPA [2] [3]

Table 3-1: Material properties assumed for the optical fibers. These properties can be expected to vary because of process variations.

Lastly, the shock profile has been assumed to be a half-sine shock pulse. This assumption has been made by comparing the time history and response spectrum of both an idealized half-sine and saw-tooth acceleration shock pulse to measured data. The measured pulse is typical to those encountered by dropping an electronic device on a hard surface, as shown in Fig. 3-1. By assuming the half-sine pulse, we are adding a factor of safety to the measured data in the range of resonance. For the optical fiber, we choose half - sine pulses of 1.0 ms and 0.1 ms duration to span the physical range for a mechanical shock.
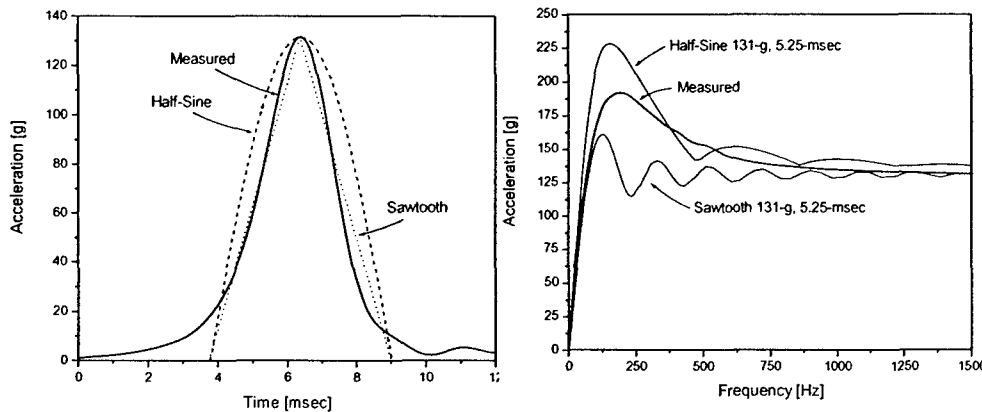
Fig. 3-1: Comparison between idealized shock pulses and measured data.

Results for a Clamped-Free Microbeam

We determined if the fibers partially align under shock loading, and if the fibers break under shock loads. In addition, the shock load necessary to have the fiber contact the substrate was determined. In order to validate the response, several finite element and analytical models were generated. First, we used an Euler-Bernoulli beam theory combined with the shock spectrum of a spring mass model. Second, we modeled the fiber in ANSYS and applied the shock as an applied load. Third, we used an equivalent spring-mass system with base excitation. Lastly, we used the same ANSYS model, but applied the shock as a base excitation. Next, we explain the models used and the results obtained from our analyses.

Distributed parameter model: Euler Bernoulli beam theory and shock amplification factor

A distributed static load will displace the tip of a cantilevered beam in the following manner: $y = \dfrac{2a_g l^4 \rho}{d^2 E}$. For example, a 600 g distributed static load will displace the beam 5.92 μm. For a dynamically loaded beam, the maximum displacement will be larger than the static case.

Comparing the natural period of the beam with the shock application period, a shock amplification factor can be obtained. This allows a static solution to be applied to a dynamic case [4].

For the 1.0 ms shock pulse, the ratio of the shock pulse to the natural period is ~12.5. This ratio is large enough so that we can assume a quasistatic response to the forcing
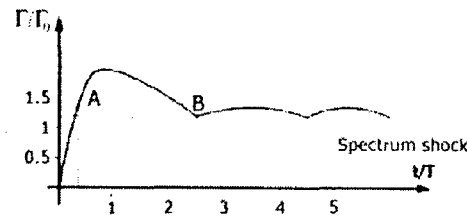
Fig. 3-2: Shock response spectrum for a half-sine base acceleration. [5]

(amplification factor ~1.1, obtained from a shock response spectrum). The 0.1 ms pulse has an amplification factor of ~1.7. This factor, found from Fig. 3-2, is multiplied by the input force to account for the dynamic nature of the problem.

ANSYS - Distributed load via structural acceleration

A finite element simulation program ANSYS was used to model the beam. SOLID95 elements, capable of stress stiffening, large deflection, and large strain effects were used. These elements were swept through the length of the beam to produce a consistent mesh. The acceleration was modeled as a half-sine pulse with a duration of either 1.0 ms or 0.1 ms. The acceleration was applied to all the nodes using the "ACEL" command using discrete data points, solving for the time transient solution. Results from ANSYS are given in Table 12.

Shock Duration	Shock level (g's)	Von Mises (MPa)	Displacement (micrometers)
1.0 ms	7,452.0	126.7	125
0.1 ms	11,363.45	135.2	125

Table 1-2: Shock levels that lead to a 125 μm displacement for both 1.0 ms and 0.1 ms shock pulse. Corresponding von Mises stresses are also shown.

It was found that a displacement of almost 8 mm is needed to **fracture** the beam, neglecting contact with the substrate. This value is unrealistic, and therefore the beam will not fracture under this type of loading. The natural period for the beam is 0.16 ms, which is close to the shock pulse of 0.1 ms. Therefore, the 0.1 ms shock pulse is expected to create a more dynamic response in the fiber than the 1.0 ms shock pulse.

When nonlinear geometry is used in ANSYS, we observed only a small deviation in displacement. The shock level investigated for this deviation was enough to displace the beam ~130 microns. These results are shown in Table 3-3.

NONLINEAR BEHAVIOR	Von Mises Stress (MPa)	Displacement (micrometers)
12000 g's, 1ms		
Nonlinear	130.4	131.6
Linear	142.8	132.0
Difference	9.49%	0.27%
7500 g's 0.1ms		
Nonlinear	115.4	126.7
Linear	127.5	125.8
Difference	10.50%	-0.69%

Table 3-3: Comparison of the results for linear and nonlinear theory for ANSYS structural acceleration. Note the small variation in displacement for a shock level that aligns the fibers.

Response to base excitation

Since the devices are very small, it can be expected that they perceive a shock pulse as a base excitation, rather than as an applied load. The last two models account for this in their approach.

Spring Mass Model

Here we use a simple spring mass model with an equivalent spring and mass. The equation of motion is then integrated to determine its response to a base excitation [6]. Results for this method are presented in 0

Comparison **between results**.

ANSYS modeling

In order to model base excitation in ANSYS, a large mass (m) is added to one end of the beam. This mass is then forced such that the structure experiences an acceleration equivalent to a = F/m. This can be seen in Fig. 3-3.
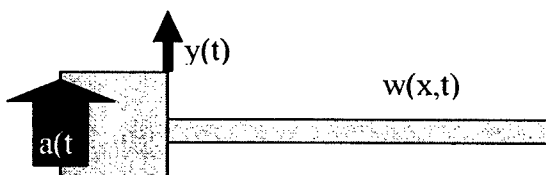
Fig. 3-3: Schematic representation of
ANSYS base excitation model.

When nonlinear geometry is used in ANSYS, we observed only a small deviation in displacement. The shock level investigated for this deviation was enough to displace the beam ~130 microns, which is the largest displacement that the beam can be expected to achieve. These results are shown in Table 3-43-4.

LINEAR VS NONLINEAR COMPARASION

	Von Mises Stress (MPa)	Displacement (micrometers)
12000 g's, 1.0 ms		
Nonlinear (geometry)	141.2	131.7
Linear (geometry)	142.8	132.0
Difference	1.17%	0.24%
7500 g's 0.1ms		
Nonlinear (geometry)	90.0	126.98
Linear (geometry)	90.2	125.98

Table 3-4: Comparison between linear and nonlinear theory for ANSYS base excitation. Note the small variation in displacement, for a shock level that aligns the fibers.

Figure 3-5 shows the maximum displacement of the beam (tip deflection) for both the 0.1 ms and 1.0 ms shock pulse. The 0.1 ms shock pulse creates a larger response in the fiber than the 1.0 ms pulse. This is because the 0.1 ms shock pulse is closer to the natural period of the fiber (0.160 ms).
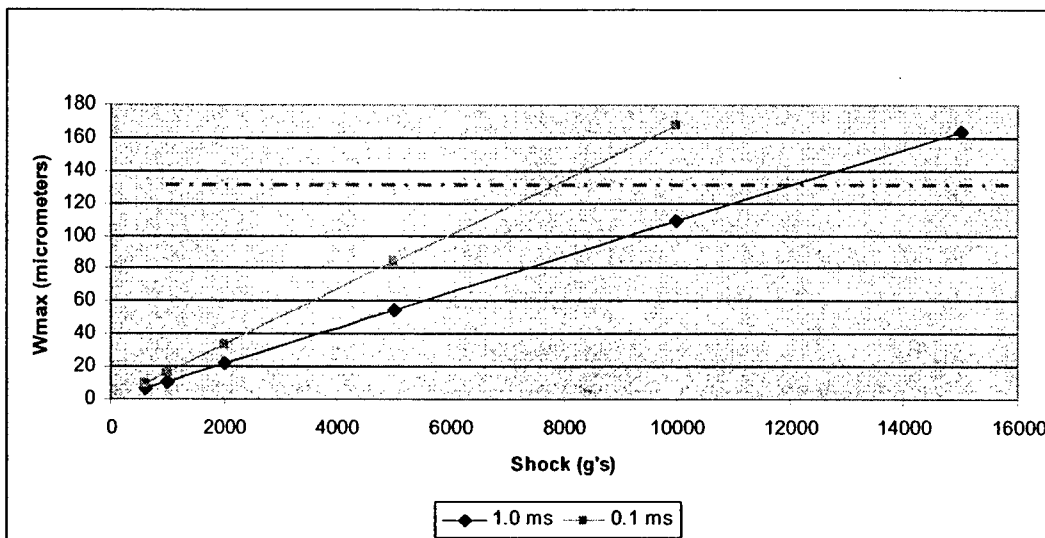
Fig. 3-5: Comparison of maximum displacement for shock durations of 0.1 ms and 1.0 ms. The red horizontal line shows the displacement at which the optical fibers will align.

Figure 3-6 compares the time history response of the beam for the 1.0 and 0.1 ms shock pulses. For the longer shock pulse (1 ms), the beam behaved quasistatically during the shock application, and vibrated freely afterward. For the shorter shock pulse (0.1 ms), the structure responded as if it was subjected to an impulsive force.

Time history for 1 ms shock pulse
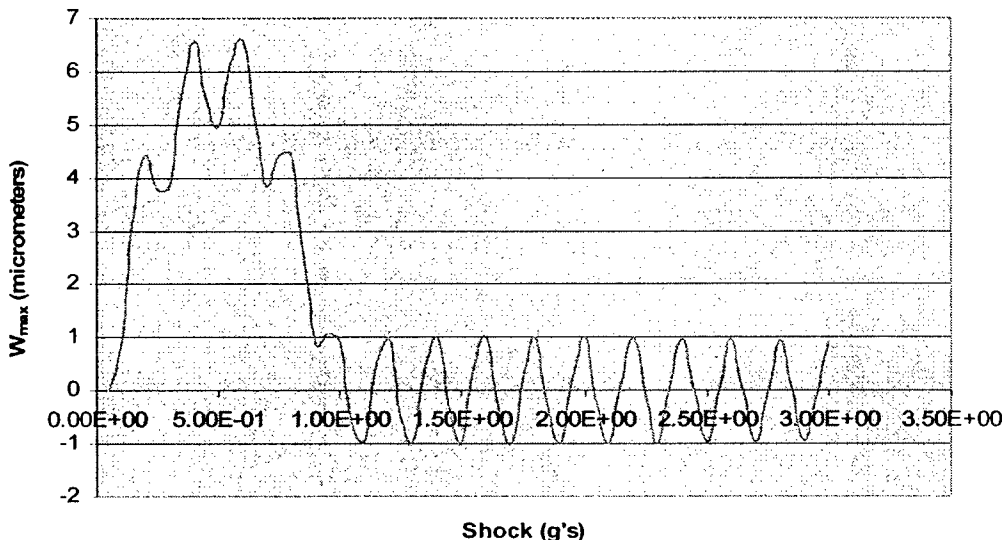
Time history for 0.1 ms shock pulse
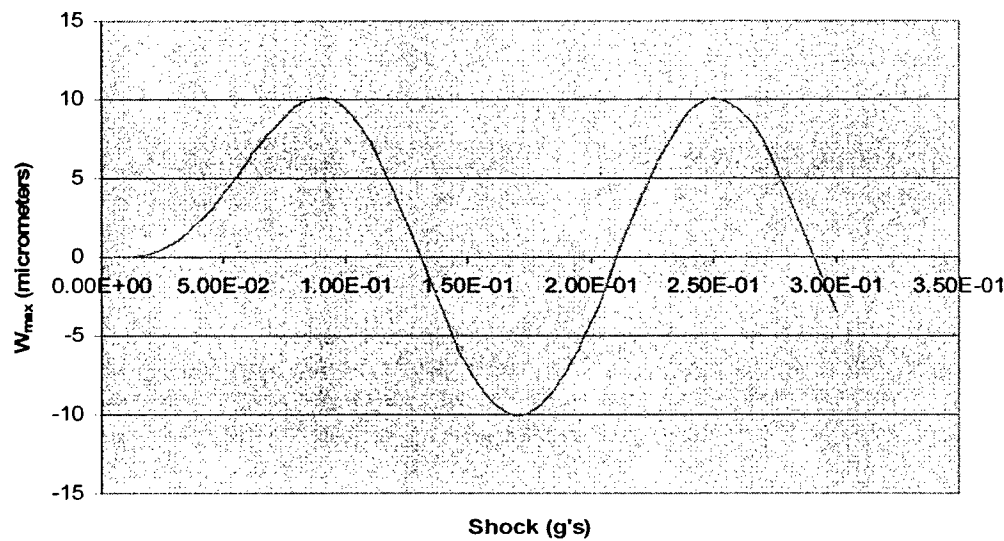
Fig. 3-6: ANSYS results for the two shock cases (1.0 ms and 0.1 ms pulses), applied as a base excitation. The amplitude of the shock level is 600 g's. Notice the quasi-static response for the 1 ms shock pulse and the dynamic response for the 0.1 ms shock pulse.

Comparison between results

Table 3-45,

Table 3-6 and Fig. below show a comparison between the results of the methods used.
Table 3- shows the shock level, for each method used, to displace the fiber tip 125 microns. This distance is enough to align the fibers completely.
Table 3-6 shows the shock level at which the fibers will strike the substrate. Fig. compares the shock load versus tip displacement curves calculated using all the approaches.

	Amplitude of shock (g)	
Model used	0.1 ms Shock duration	1.0 ms Shock duration
Euler Beam	7,507	11,602
ANSYS Distributed Load	7,450	11,363
Spring Mass	8,175	11,752
ANSYS Base excitation	7,466	11,448

Table 3-5: Level of shock (g's) to displace the beam 125 microns, aligning the fibers.

	Amplitude of shock (g)	
Model used	0.1 ms Shock duration	1.0 ms Shock duration
Euler Beam	120.12	185.64
ANSYS Distributed Load	130.51	188.05
Spring Mass	130.8	181.65
ANSYS Base excitation	114.4	183.18

Table 3-6: Level of shock (g's) to displace the beam 2 microns, hitting the substrate.

Comparision Between Results for 1.0 ms shock pulse
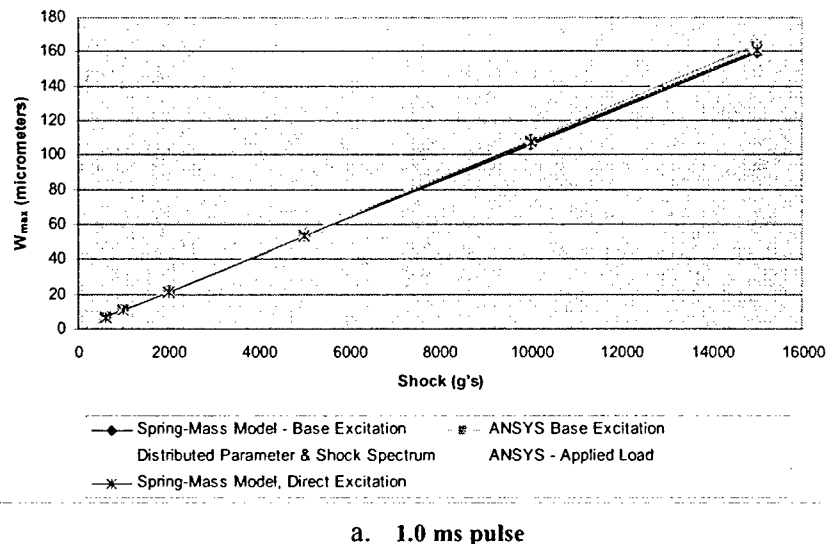
a. 1.0 ms pulse

Comparision Between Results for 1.0 ms shock pulse
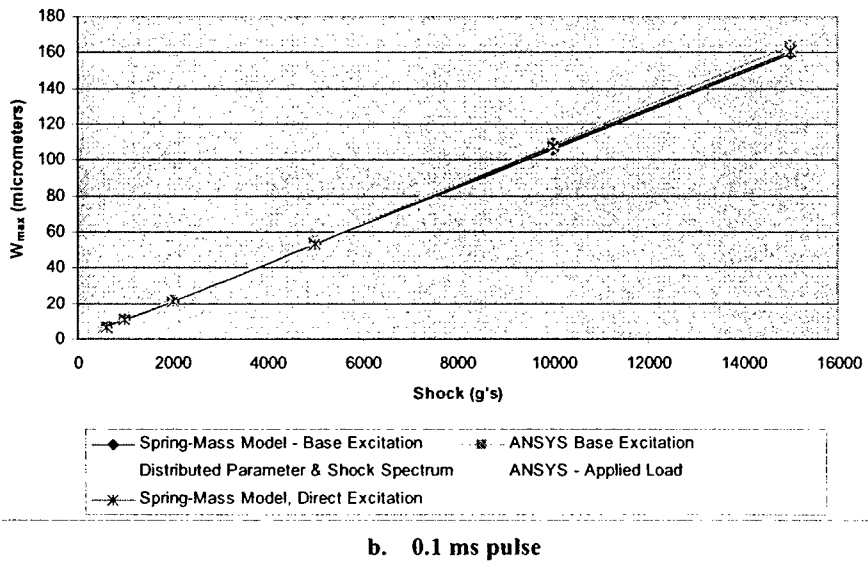
b. 0.1 ms pulse

Fig. 3-7: A comparison among various approaches for the two shock cases (1.0 ms and 0.1 ms pulses). Plotted values are the maximum beam displacement for a given half-sine shock input.

Parametric Studies

For the distributed static load presented in the first method, the equation for the maximum displacement at the free end is $y = \dfrac{2a_g l^4 \rho}{d^2 E}$, where ρ is the density of the beam and a_g is the acceleration applied to the beam in units of length*time^{-2}. This simplistic formula shows the displacement's dependence on both the length and the diameter of the beam. This dependence is validated with ANSYS. Note that for the purposes of this analysis, linear theory was used in ANSYS for the reduced diameter case, where significant tip displacement takes place.

7000 g's, 1 ms shock pulse	Displacement (μm)	
	ANSYS	Static Load
Original	76.43	--
1/2 length	4.46	4.78
1/2 diameter	332.30	305.72
3/4 diameter	145.05	135.87

Table 3-7: Design modifications
Deviations from the expected values occur because the natural frequency of the beam changes as the length and diameter are varied. This changes the dynamic nature of the ANSYS model. The original design has a length of 4000 μm and a diameter of 125 μm.

As the length is increased or the diameter is decreased, the natural period of the structure increases closer to the 1 ms shock pulse. This creates more resonance effects, which makes the observed displacement in ANSYS higher than predicted by the static case, where this phenomenon is not accounted for. The opposite effect can be seen when halving the length. As the natural frequency gets closer to the shock pulse, the shock amplification factor increases, which further creates variations between the predicted static case and the dynamic case. Therefore, the general trend of $y \propto \dfrac{1}{d^2}$ and $y \propto l^4$ from the static case can only be used as a first approximation.

Effect of damping

Damping in the system can be modeled, in the spring mass system, by including a term that is proportional to the velocity of the mass. In Table and Table we show the tip displacement that occurs for varying levels of damping. For the highest damping ratio, it can be seen that the tip displacement for the 0.1 ms shock pulse is lower than that of the 1.0 ms pulse. This is opposite from what is seen when damping is not present. As the damping ratio increases, the shock response spectrum decreases. At a damping ratio of 0.5, the amplification factor is lower in the 0.1 ms case than in the 1.0 ms case.

Maximum Tip Deflection (micrometers) for a shock level of 1500 g's		
	1.0 ms	0.1 ms
Damping Ratio		
0	16.11	23.15
0.05	15.32	21.45
0.5	14.76	12.76

Table 3-8: Effect of damping in a spring mass model with base excitation for 1.0 and 0.1 ms shock pulses, at a shock level of 1500 g's.
Notice that for heavy damping, the response to the 0.1 ms shock duration is lower than the response to the 1.0 ms shock pulse.

Maximum Tip Deflection (micrometers) for a shock level of 5000 g's		
	1.0 ms	0.1 ms
Damping Ratio		
0	53.71	77.18
0.05	51.06	71.49
0.5	49.21	42.53

Table 3-9: Effect of damping in a spring mass model with base excitation for 1.0 and 0.1 ms shock pulses, at a shock level of 5000 g's.
Notice that for heavy damping, the response to the 0.1 ms shock duration is lower than the response to the 1.0 ms shock pulse.

Mechanical Stress

Optical fibers produced from synthetic fused silica have a theoretical strength of ~2,000 kpsi (~13.8 GPa), based upon the Si-O bond strength. The presence of imperfections and flaws in the bulk of the material and on its surface lowers the observed strength to ~700 kpsi (4.8 GPa). Other literature states the fracture strength of silica to be 8.4 GPa [3].

Table 1 shows that the von Mises equivalent stress, at a level capable of aligning the fiber, would not cause the fiber to fracture.

3-1-2 Thermal Actuator Modeling

Some approximations have been taken during the analysis of the thermal actuator. First, ideal clamped-clamped boundary conditions were assumed, however in reality this may not be true [1]. Variations in material properties, due to fabrication conditions, have been neglected. In addition, single crystal silicon behaves anisotropically, and it is therefore difficult to obtain single values for the material properties that are used with

certain models. Literature gives a range of Young's Moduli, including 190 GPa [9], 166 GPa [1], and 150 GPa (υ=0.17) [10]. The properties assumed throughout this analysis are shown in Table .

Silicon (Si)
- Length = 5500 μm [1] [8]
- Thickness = 125 μm [1] [8]
- Width = 20 μm [1] [8]
- Offset = 45 μm [1] [8]
- Density = 2332 kg/m^3 [1] [9]
- Modulus of Elasticity =154 GPa
- Poisson's Ratio = 0.3
- Yield Strength= 7 GPA [9] [3]

Table 3-10: Material properties assumed for the thermal actuator. These properties can be expected to vary because of process and material variations.

Again, a half-sine shock pulse has been used to represent the shock profile (See Fig. 3-1 and Section **Error! Reference source not found.**). We choose sine pulses of 1.0 ms and 0.1 ms duration to span the physical range for a mechanical shock.

Results for a Clamped-Clamped Thermal Actuator

In order to determine its response to shock pulses of 1.0 and 0.1 ms and to minimize computational requirements, we modeled the thermal actuator with half-symmetry. We verify if the thermal actuator is capable of pushing against the optical fiber during shock loads. In addition, we establish the shock load necessary to have the thermal actuator contact the substrate.

Finite-Element Model

We used ANSYS, a finite element simulation program, to simulate the device's response to shock loads. SOLID95 elements were used to model the thermal actuator. These elements are capable of capturing nonlinear behaviors, such as stress stiffening, large deflection, and large strain effects. The elements were swept through segments of the thermal actuator to produce a consistent mesh. The thermal actuator was modeled as a clamped-clamped frame with an offset, with a center section containing regular perforations (25μm x 25μm, with 25 μm spacing between each perforation). The shock was modeled as a half-sine pulse with a duration of either 1.0 ms or 0.1 ms. The shock was applied to all the nodes of the finite element model via the "ACEL" command using discrete data points, solving for the time transient solution. In our first report on the modeling and simulation of the optical fiber, we show that applying a distributed load across a structure is comparable to a base excitation on the structure. Since the small structures are expected to perceive a shock pulse as a base excitation, and we have previously shown that a distributed load across a structure is equivalent to a base

excitation, then we are justified in using such approach here. Fig. through Fig. show the beam without symmetry, and with the length, offset, thickness and width labeled.
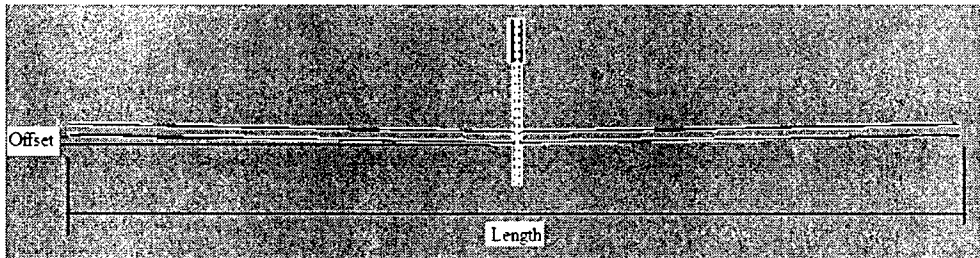

Fig. 3-8: Full model of thermal actuator. Analysis was performed using half-symmetry.
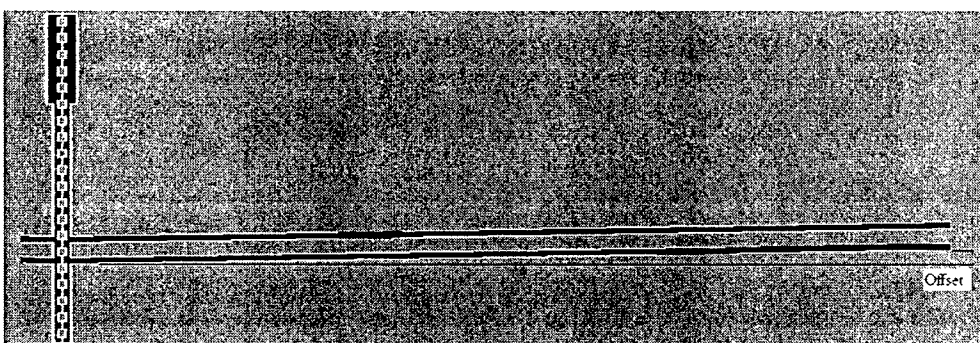

Fig. 3-9: Closer view of offset
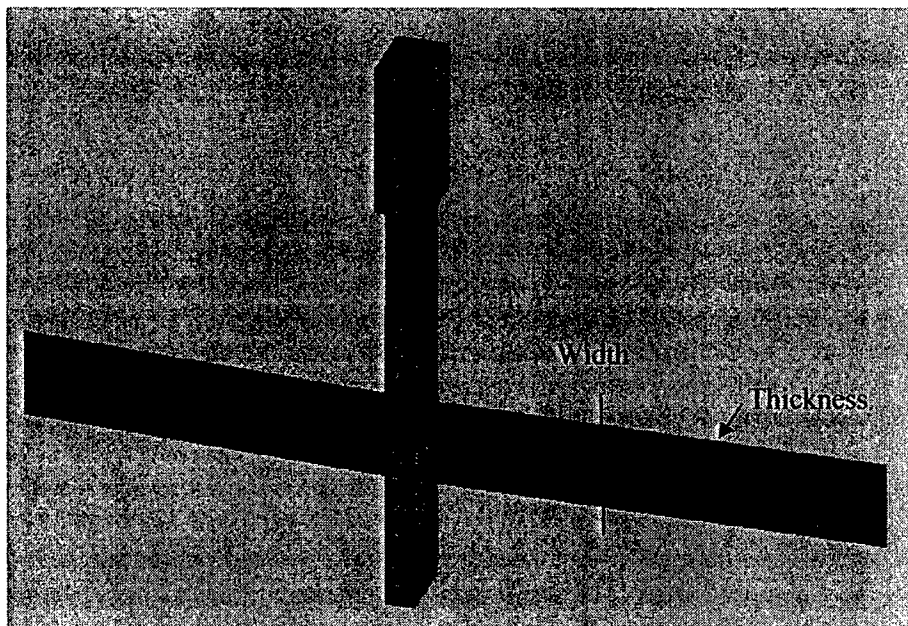
Fig. 3-10: Center section of thermal actuator.

In-Plane Results

We study the response of the thermal actuator to in-plane shock loads of duration 1.0 ms and 0.1 ms. Fig. shows a comparison between the results of linear and nonlinear theories, revealing that geometric nonlinearities are significant even for small shock levels. We conclude that a nonlinear beam theory and analysis has to be used to simulate the mechanical response of the actuator to in-plane loads. It is clear from Fig. that the response due to the 0.1 ms shock load is larger than that of the 1.0 ms shock.
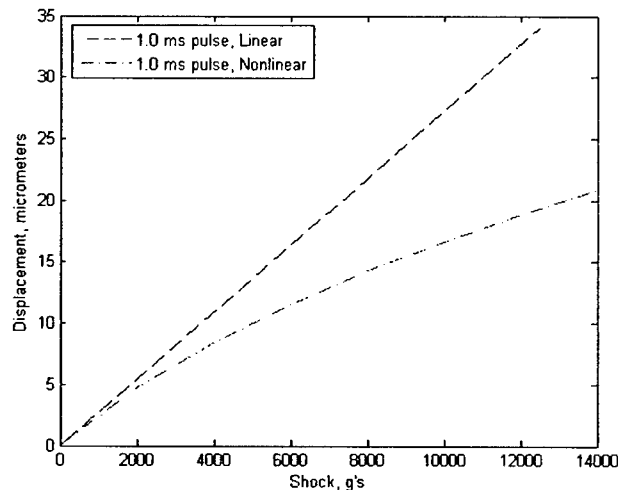
a) 1.0 ms shock pulse
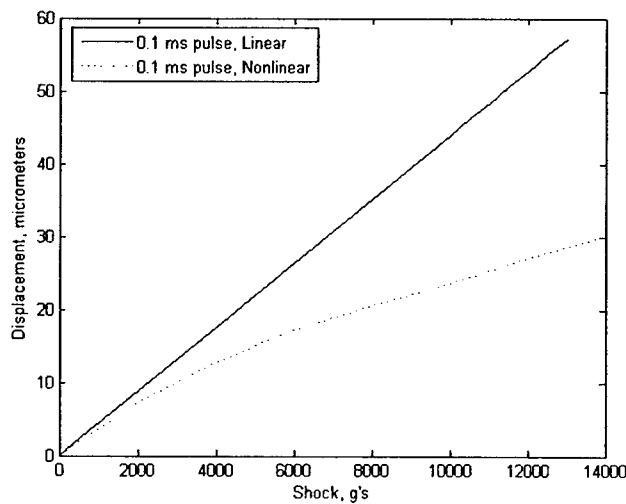
b) 0.1 ms shock pulse

Fig. 3-11: Comparison between linear and nonlinear theory for ANSYS distributed load. Note the variation in displacement between linear theory and nonlinear theory at increasing shock levels.

To justify this, we calculate the natural frequency of the actuator (Table). The natural period for the thermal actuator in the in-plane direction is 0.094 ms, which is close to the shock pulse of 0.1 ms. Therefore, the actuator exhibits a dynamic response to a 0.1 ms shock pulse, and displaces further than when excited by the longer shock pulse of 1.0 ms.

Natural Period (ms)	Description of mode
0.0939	In-plane motion – Looks similar to the response to an in-plane load
0.0605	Twisting about the actuator arms (clamped-clamped beams) – Looks similar to the response to an out-of-plane load.
0.0445	Actuator arm stationary, stacked clamped-clamped beams moving in opposite directions in-plane
0.0362	In-plane motion – Looks similar to the 3rd mode of a clamped-clamped beam
0.0324	Out-of-plane motion – Twists about middle of actuator arm – Center of clamped-clamped beams displaces out-of-plane

Table 3-11: First 5 natural periods for the thermal actuator.
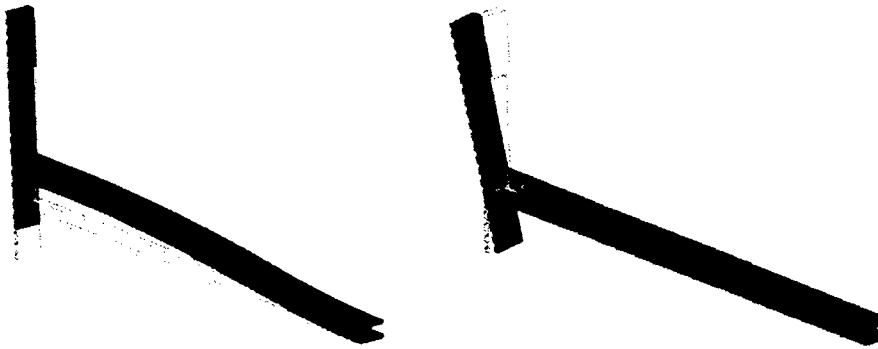
a) First Mode Shape

b) Second Mode Shape
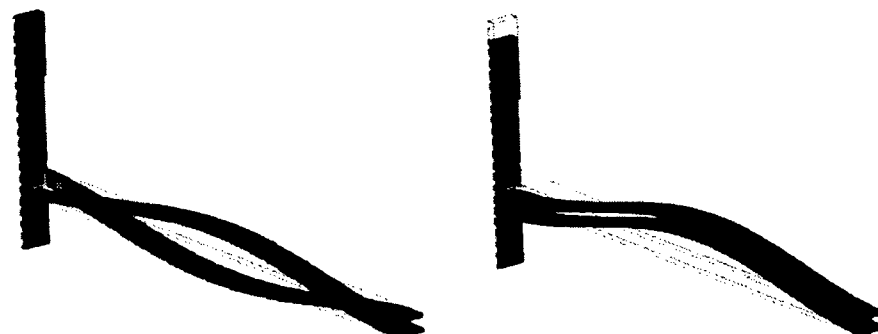
c) Third Mode Shape

d) Fourth Mode Shape
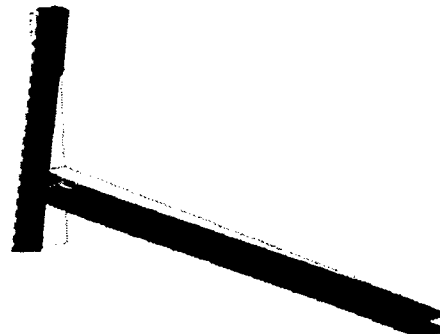
e) Fifth Mode Shape

Fig. 3-12: First 5 mode shapes of the thermal actuator

In Fig. , we compare the response of the thermal actuator to that of the cantilevered optical fiber under the same shock load. We notice that a significant shock load is necessary to force the actuator in the in-plane direction, compared to the optical fiber. Therefore, we conclude that a shock load in the in-plane direction, towards fiber alignment, will not cause the thermal actuator to contact the optical fiber.
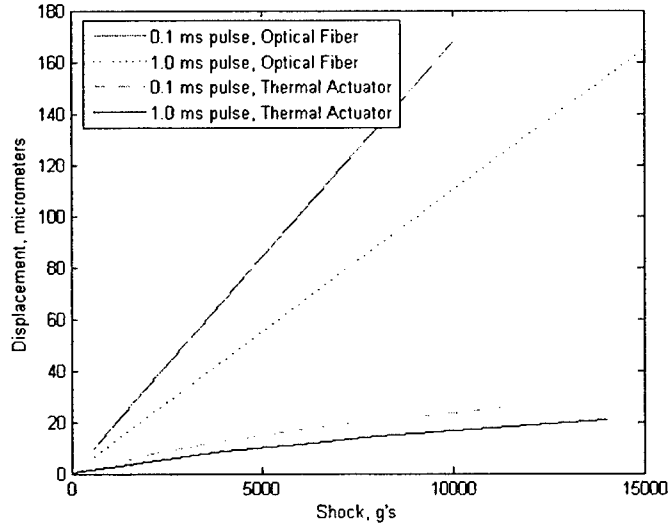
Fig. 3-13: Response of optical fiber and thermal actuator to in-plane shock loads of 0.1 & 1.0 ms durations. The thermal actuators will be incapable of pushing the optical fibers into alignment during shock loads.

Out-of-Plane Results

We investigate the response of the thermal actuator to an out-of-plane shock load. Figure 3-4 shows the response of the thermal actuator to shock loads of durations 0.1 ms and 1.0 ms, calculated using linear and nonlinear theories. We observe that in the out-of-plane direction, a displacement of 4 μm does not cause significant nonlinearities to arise. Hence the thermal actuator behaves linearly in this direction. For a 1.0 ms shock duration, a shock level of approximately 1,500 g's is needed to cause the device to hit the substrate, based on a 2 micrometer gap, and approximately 3000 g's to hit the substrate based on a 4 micrometer gap. For the 0.1 ms shock duration, a shock level of approximately 1200 g's is needed to cause the device to hit the substrate, based on 2 micrometer gap, and approximately 2250 g's to hit the substrate based on a 4 micrometer gap. Figure 3-4 shows that the response to the shorter shock pulse (0.1 ms) is larger than the response to the longer shock pulse (1.0 ms). This can be justified by observing that the second natural period (Table) is close to the 0.1 ms shock duration, and that the second mode shape is similar to the response to an out of plane shock. Similar to the in-plane case, the actuator exhibits a dynamic response to the 0.1 ms shock pulse, and displaces further than when excited by the 1.0 ms shock pulse.

In addition, we find that the tip of the thermal actuator will contact the substrate first. Fig. shows the deformed shape of the actuator when subjected to an out of plane shock of 2000 g's, for a shock duration of 0.1 ms. The maximum displacement in the out of plane direction is approximately 3.6 micrometers in this case. This can be justified by visualizing the thermal actuator as a clamped-clamped beam, with a cantilevered beam attached to its center and extending perpendicularly from it. When both structures are

subjected to a distributed load, the clamped-clamped beam will deflect the greatest distance at its center, where the cantilevered beam is located. The tip of the cantilevered beam will deflect even more. This visualization justifies the observation that the tip of the thermal actuator touches the substrate first.
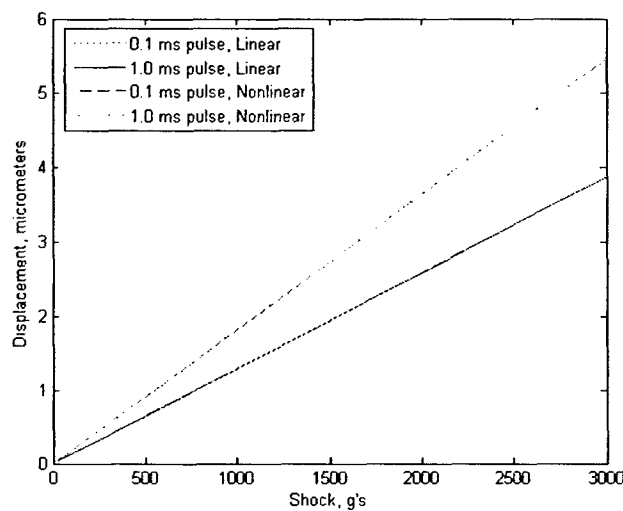

Figure 3-4: Out-of-plane displacement due to shock load.
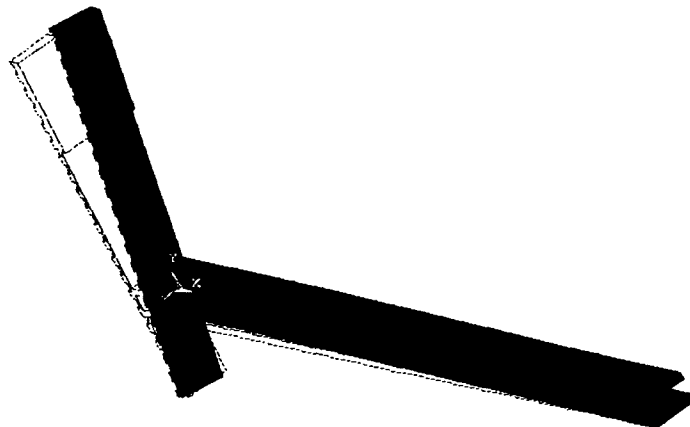
Fig. 3-15 Deformed shape due to out of plane shock of 2000g. Also shown is the outline of the unforced actuator.

Parametric Studies

Several design parameters have been identified that are capable of increasing the thermal actuator's resistance to shock. For an in-plane shock load these include

increasing the width of the thermal actuator beam, and decreasing the length of the beam. For an out-of-plane shock load these include increasing the thickness of the thermal actuator beam and decreasing the length of the beams, as defined in Fig. . Also investigated was the number of clamped-clamped thermal arms attached to the center actuator arm. The offset in the center of the beams has been found to influence the resistance to shock.

Fig. shows that decreasing the length increases the in-plane shock resistance of the microbeam. Fig. shows the response of the beam to out-of-plane shock loads when the length of the thermal actuator is varied.
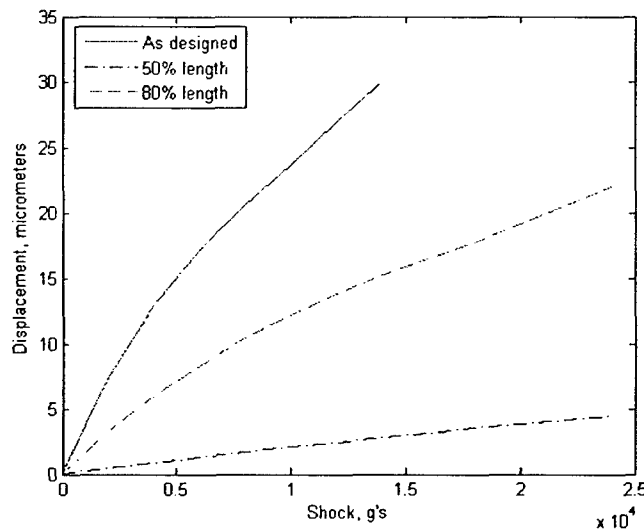
Fig. 3-16: Effect of varying the length of the thermal actuator on the shock resistance of the thermal actuator to in-plane shock loads.
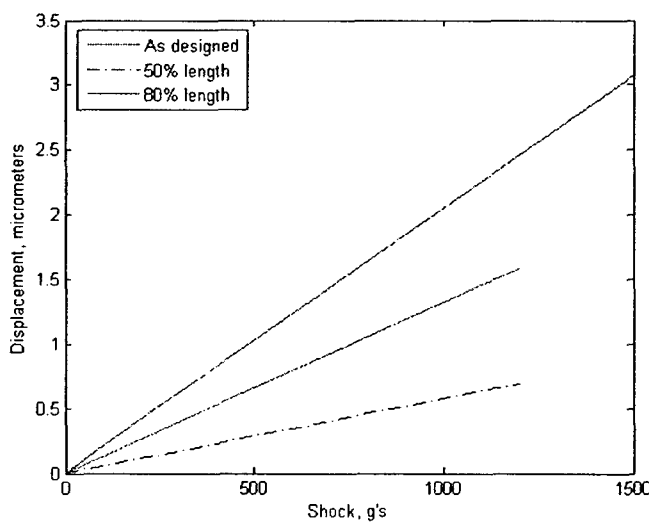
Fig. 3-17: Effect of varying the length of the thermal actuator on the shock resistance of the thermal actuator to out-of-plane shock loads.

The addition of actuator beams (stacking) will decrease the response of the structure to a given shock load. At a shock level of 7000 g's and 0.1 ms shock duration, a thermal actuator with a single clamped-clamped beam will have a displacement of 24 µm. For the same shock load, but with two clamped-clamped beams, the maximum displacement will be 19 µm. Therefore, by increasing the number of clamped-clamped beams, we can increase the robustness of the device to shock and vibration. Fig. shows this effect. It also shows the effect of varying the length of the beam. Additional robustness could be obtained by implementing a "cascading" thermal actuator device [13], however this would necessitate a major redesign of the chip, and no work has been done analyzing this type of arraignment.
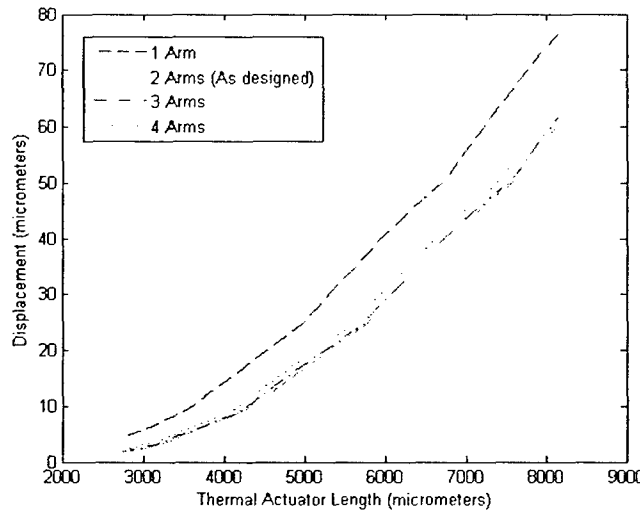
Fig. 3-18: Effect of the addition of actuator beams and their length on the maximum response to an in-plane shock load of 1000 g's and 0.1 ms duration

Fig. shows the effect of the offset on the response of the beam. Here the duration of the shock load is 0.1 ms. This figure illustrates that a larger offset increases the device's resistance to shock in the in-plane and out-of-plane directions. Previous papers [12] have shown that increasing the offset will in turn decrease the tip displacement during thermal actuation. These two effects need to be balanced, such that proper thermal actuation can take place while ensuring vibration and shock robustness.
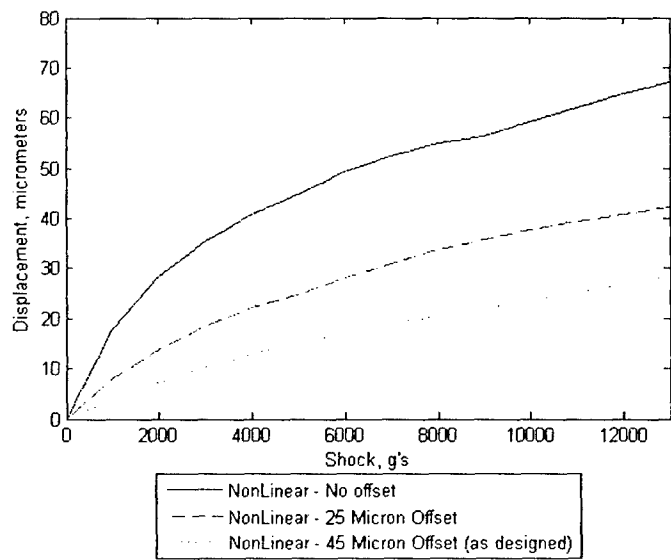
a) In-plane loading
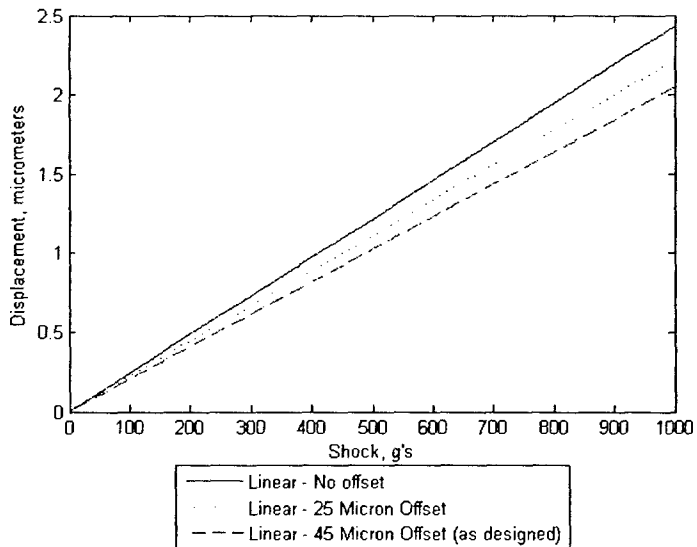
b) Out-of-plane loading

Fig. 3-19: Effect of varying the center offset in the thermal actuator.

Fig. shows the effect of varying the thickness of the thermal actuator on its response to an out of plane shock load. A reference shock amplitude of 10,000 g's was used with a duration of 0.1 ms. This figure shows the dependency of the displacement on the value $\dfrac{1}{thickness^3}$. This dependency can be seen when subjecting a clamped-clamped

beam to an out of plane distributed static load, where the displacement is $y_{max} = \dfrac{-wl^4}{384EI}$,

where $I = \dfrac{1}{12}(width)(thickness)^3$. A shock amplitude of 15,000 g's is needed to displace a 145 μm thick actuator the same distance as a 125 μm at 10,000 g's. Therefore, increasing the thickness 25 μm from the original design will yield an improvement of 50% in shock resistance. Note that this change may not be feasible, as it would entail etching the features of the device further into the substrate, which would change other features on the chip. We have not focused on increasing the shock resistance in the in-plane direction by increasing the width, as the thermal actuator is sufficiently stiff enough not to contact the optical fiber during shock loading.
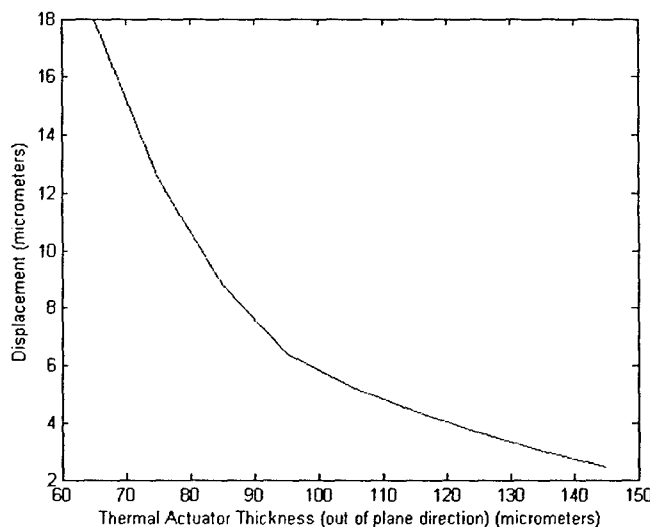
Fig. 3-20: Effect of varying the thickness in the thermal actuator.

Mechanical Stress

The fracture strength of silicon is 7 GPa [9] [3]. In order to examine the stress profile in the thermal actuator, we displaced a node on the tip of the beam 125 μm with ANSYS. In doing so, we find a maximum von Mises stress in the actuator of 2.3 GPa. Furthermore, this stress occurred at the point of application of the displacement, and the stress around this point dropped away quickly. Since the observed stress is much lower than the fracture strength of the silicon, and may have been artificially increased by the presence of the point displacement, we determine that the thermal actuator will not fracture at this displacement.

3-1-3. G-sensor

Here we determine the effect that the squeezed-film damping effect on G-sensor during out of plane motion, and determine the effect of design parameters on the squeeze film damping effect.

Structural Modeling

In order to model the G-sensor's response to shock and squeeze film damping, we first separated the structural and fluidic domains to analyze each separately. For the structural domain, we modeled the G-Sensor in ANSYS using 4-Node Finite Strain Shell elements (SHELL181). This element is suitable for moderately thick shell structures, and is able to model linear, large rotation, and large strain nonlinear problems. This element is also capable of displacements in 3 directions at each node, making it suitable for out of plane displacements. Fig. shows the model, which includes the holes and the springs. The G-sensor is constructed out of silicon, whose properties are listed in Table . This model does not have any restrictions on its movement; the G-sensor is a flexible plate that can deform in any direction.
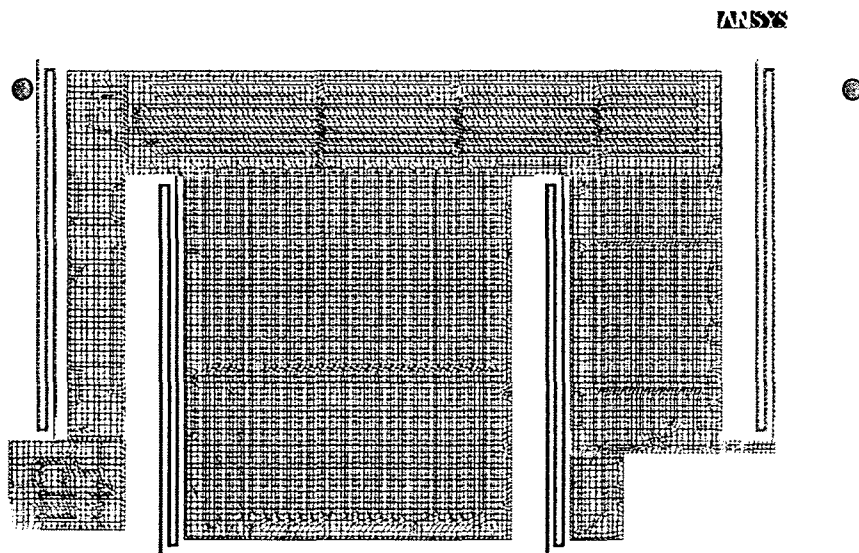
Fig. 3-21: Model of the G-Sensor, structural domain.
The red dots indicate points where the displacement is measured in Fig. and Fig. .

Modal Analysis

We first performed a modal analysis in ANSYS on the G-sensor, to determine its mode shapes and natural frequencies. Fig. shows the first 4 out-of-plane mode, and Table shows their natural periods. This analysis illustrates that there are several natural frequencies within a close range, so it is possible that several modes will be excited as the G-sensor responds to shock loading.

1ˢᵗ mode: 2075.9 Hz – 0.48 ms   2ⁿᵈ Mode: 2381.1 Hz – 0.42 ms

3ʳᵈ Mode: 3248.4 Hz – 0.31 ms   4ᵗʰ Mode: 24807 Hz – 0.04 ms
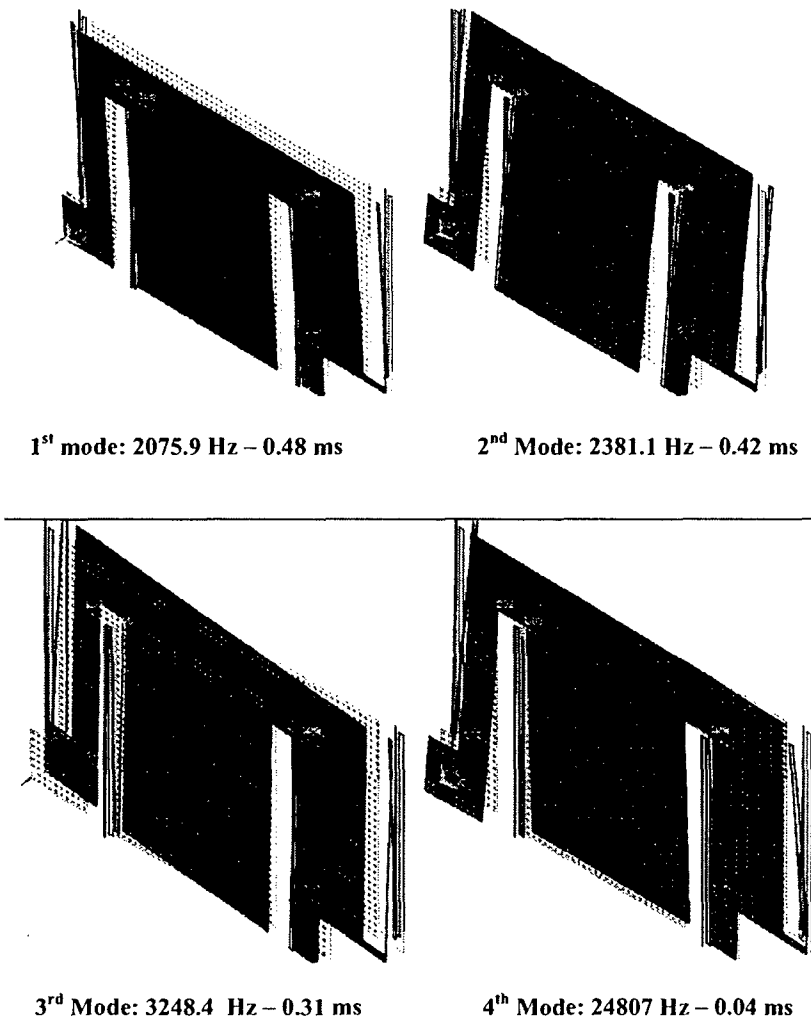
Fig. 3-24: First 4 out-of-plane mode shapes and their corresponding natural frequencies

Mode	Natural Frequency (Hz)	Natural Period (ms)	Shock ratio T_{pulse}/T_{nat}		
			1.0 ms shock	0.1 ms shock	0.5 ms shock
1	2075.9	0.48	4.17	0.42	2.08
2	2381.1	0.42	4.76	0.48	2.38
3	3248.4	0.31	6.45	0.65	3.23
4	24807	0.04	50	5	25

Table 3-12: First 4 out-of-plane natural frequencies and periods.

Mode	Natural Frequency (Hz)	Natural Period (ms)	Shock ratio T_{pulse}/T_{nat}		
			1.0 ms shock	0.1 ms shock	0.5 ms shock
1	214.16	4.669	0.42832	0.042832	0.21416
2	1993.3	0.502	3.9866	0.39866	1.9933
3	2133.4	0.469	4.2668	0.42668	2.1334
4	2477.3	0.404	4.9546	0.49546	2.4773
5	2478.1	0.404	4.9562	0.49562	2.4781
6	2478.6	0.403	4.9572	0.49572	2.4786
7	2489	0.402	4.978	0.4978	2.489
8	6970.8	0.143	13.9416	1.39416	6.9708

Table 3-13: First 8 non- out-of-plane natural frequency and periods.

Undamped Shock Response

In order to characterize the response of the G-sensor to shock loading, we first analyze the device without damping. By neglecting all damping, we are assuming a worst-case scenario. This also provides a baseline to compare to the damped model. As in the previous work, we modeled the shock as a half-sine pulse, applying it at discrete time intervals by using the "ACEL" command in ANSYS. See Fig. 3-1 and Section 0 for an explanation of this assumption.
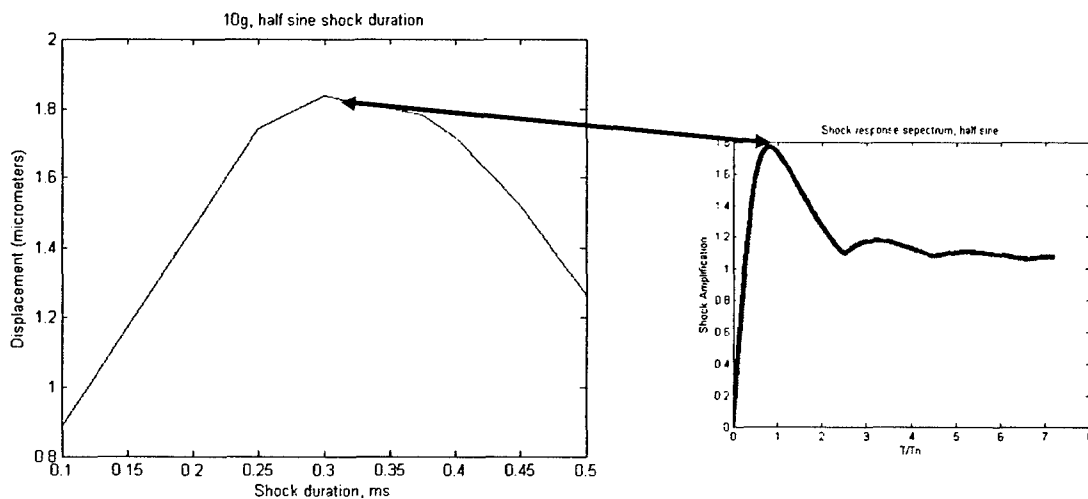
Fig. 3-23: Maximum displacement of the G-sensor to a shock pulse of 10g and varying duration (left). The maximum point corresponds to the peak of the shock spectrum (right).

As before, we needed to choose a shock duration that created a large displacement in the G-Sensor. We found this duration to be approximately 0.3 ms. Fig. shows these results. Fig. shows the shock amplitude needed to cause the G-sensor to contact the substrate for different gap widths. It is clear that without damping, a very low shock level is capable of causing the G-Sensor to contact the substrate.
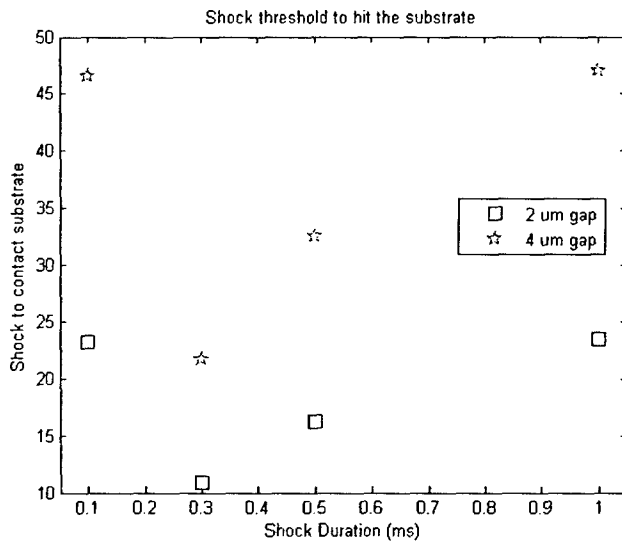
Fig. 3-24: Shock amplitude needed to cause contact with the substrate, for both a 2 μm and 4 μm gap.

Fig. and Fig. show the response at each corner of the G-Sensor to an out-of-plane shock of 10 g's. Here the period of the smaller oscillations is about 0.5ms, which is close to period of the first 3 out-of-plane modes (Table). The larger period seen in Fig. is due to the constructive interference between the first two out of plane modes. The difference between the first two natural frequencies is approximately 200 Hz, which is the same as the outer envelope of the response.
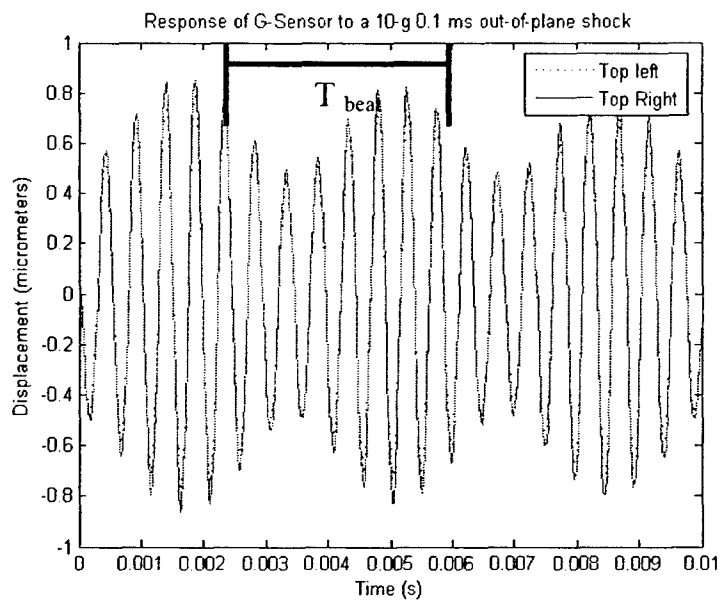
Fig. 3-25: Response of the G-Sensor to an out of plane shock of 10 g's at a duration of 0.1 ms. The maximum displacement is 0.86 µm. See Fig. for the physical locations of the plotted points on the G-Sensor.
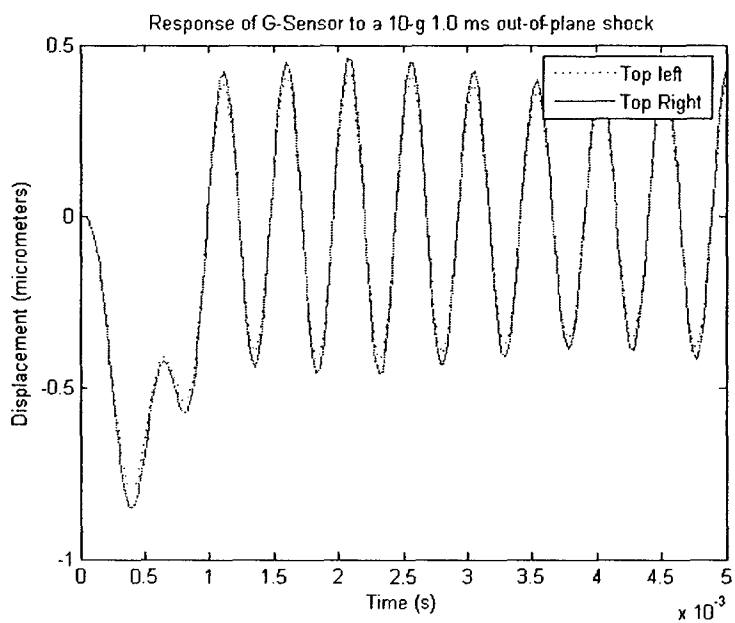
Fig. 3-26: Response of the G-Sensor to an out of plane shock of 10 g's at a duration of 1.0 ms. The maximum displacement is 0.85 µm. See Fig. for the physical locations of the plotted points on the G-Sensor.

Modeling of Squeeze Film Damping

Theory

At the micrometer length scale, the movement of a proof mass normal to a stationary wall squeezes the air gap between the two objects. This causes significant forces from the air gap on the proof mass, affecting its dynamics. This force can have a component in phase with the displacement, and a component in phase with the velocity. The former force leads to a restoring spring force, while the latter creates a damping force. At low frequency movements, the air is able to move out from under the structure, minimizing the spring force and allowing the damping to become the dominant force from the air gap. At higher frequencies, the air is unable to move out from under the device, creating a spring force and lowering the damping. [14] This effect can be seen in Fig. .

Fig. 3-27: Damping and stiffness coefficients from squeeze film damping for varying frequencies.

The shape of the structure influences the effect of squeeze film damping by affecting the venting of the gas from underneath the device. The addition of perforations into the device also affects the squeeze film damping effect by allowing air to move out through the perforations.

Since the G-Sensor is thick and supported by compliant springs, we can model the damping effect by assuming the accelerometer to be a rigid plate moving normal to the substrate. Here the G-Sensor can only move up and down, with no tipping motion allowed. This assumption allows us to decouple the structural and fluidic domains. We modeled the thin fluid domain using 3-D squeeze film fluid elements (FLUID136). This element models the flow of a viscous fluid in small gaps that are bound by a fixed surface and a surface moving perpendicularly to the fixed surface. This element is based on the Reynolds' Equation, and assumes isothermal behavior, small pressure changes compared to the ambient pressure, and small displacements compared to the film thickness. 3-D viscous fluid link elements (FLUID138) were used to model the viscous flow through the perforations in the device.


Fig. 3-28: Schematic used to model squeeze film damping.

Boundary Conditions – Perforations

No Holes

There are three different ways in which ANSYS can model the perforations and their effect on squeeze film damping. First, the perforations can be neglected if they are either very long or very slender. Physically, this means that there is a very large flow resistance through the hole, and consequently

No Pressure Specified

FLUID136

Fig. 3-29: No holes/infinite resistance pressure boundary condition for the holes.

the pressure underneath each perforation is approximately the same value as for the unperforated case. This case is equivalent to having no holes in the G-Sensor. Fig. shows this case.

No Hole Resistance

If the perforations are very thin or very wide, there is little resistance to the flow through a hole. Here, the fluid underneath the perforation has a pressure equal to the ambient pressure. To accomplish this in ANSYS, we set the pressure boundary condition along every hole to be equal to the ambient pressure. Fig. illustrates this case.

Zero Pressure BC

FLUID136
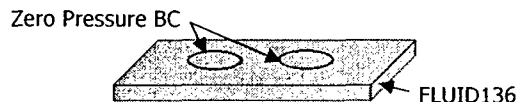
Fig. 3-30: No hole resistance pressure boundary condition for the holes.

Finite Fluid Resistance

A third way to model the squeezed film effect is to include the finite resistance in the perforations. This is the most accurate way to model the perforations, as it accounts for the pressure drop through each perforation. To do this, we introduce a new element, FLUID138, which models the flow through one

Zero Pressure BC

FLUID138

FLUID136

Fig. 3-31: Finite Pressure boundary condition for the holes.

perforation. Here, the pressure at one end of the FLUID138 element is coupled to the surrounding FLUID136 elements, and at the other end the pressure is set to the ambient pressure. Fig. demonstrates this case.

Compressible Fluid Assumption

In order to account for the compressibility of the gas, we subject the fluid to a harmonic fluid velocity. By varying the frequency, we can examine how the fluid will react when the G-sensor vibrates. We notice that the squeeze film damping coefficient does not vary greatly from 0 Hz to 50 000 Hz, while the spring force increases slightly from zero. Since the damping force is greater than the spring force over this frequency range, the fluidic damping can be considered constant, and the compressibility of the fluid can be neglected [15].

Incompressible fluid assumption

By neglecting the compressibility of the fluid, we simplify the problem by neglecting the spring effect from the fluid and considering the damping effect only. To do end, we subject the fluid elements to an arbitrary velocity, which creates a pressure distribution in the fluid. Integrating the pressure distribution over the area determines the damping force, which can be used to determine a damping coefficient by $c = \dfrac{F}{v_z}$ [15].

This damping coefficient is the c value in the single degree-of-freedom equation $m\ddot{x} + c\dot{x} + kx = f(t)$. It can be converted to a damping ratio by the formula, $\zeta = \dfrac{c}{2m\omega_n}$, where ω_n is the first out-of-plane natural frequency in rad/s. This value is a first approximation, since the real structure will not oscillate at its first out of plane natural frequency, like a one degree-of-freedom system. In this application, a low damping ratio is not desirable, as it may allow the g-sensor to contact the substrate during shock loading, which could damage the sensor or render it inoperable due to stiction effects.

Hole Boundary Condition	Damping Ratio
No Holes	309
No Hole Resistance	0.15
Finite Resistance, 25 μm perforations	0.21

Table 3-14: Damping Ratios for different boundary conditions.

Results

For the first case, where the holes are neglected, the damping ratio is found to be 309. Fig. shows the pressure distribution for this case, which is highest in the center and decreases to ambient on the periphery.

In the case of no hole resistance, the damping ratio decreases to 0.1453. Fig. shows the pressure distribution in the G-Sensor for the case of no hole resistance. The holes can be seen to lower the pressure exerted on the G-sensor, thereby decreasing the damping ratio. Including the hole resistance increases the damping ratio slightly to 0.2125.

| 0 | 241.716 | 483.432 | 725.147 | 966.863 | 1209 | 1450 | 1692 | 1934 | 2175 |
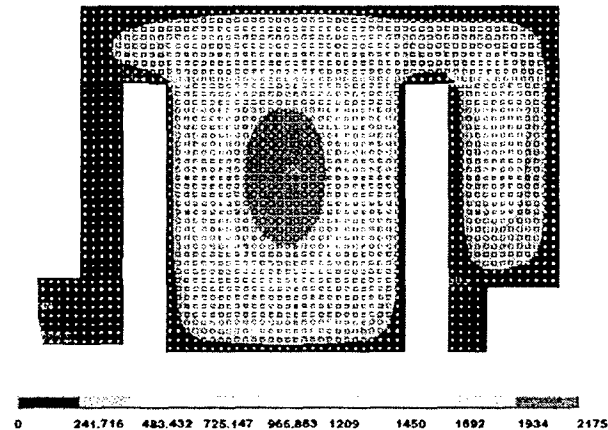
Fig. 3-32: Pressure distribution due to squeeze film damping - no boundary conditions on the perforations. A gap thickness of 2 μm is assumed.

| -.282E-6 | .44E-6 | .908E-6 | .138E-4 | .184E-4 | .231E-4 | .278E-4 | .325E-4 | .372E-4 | .419E-4 |
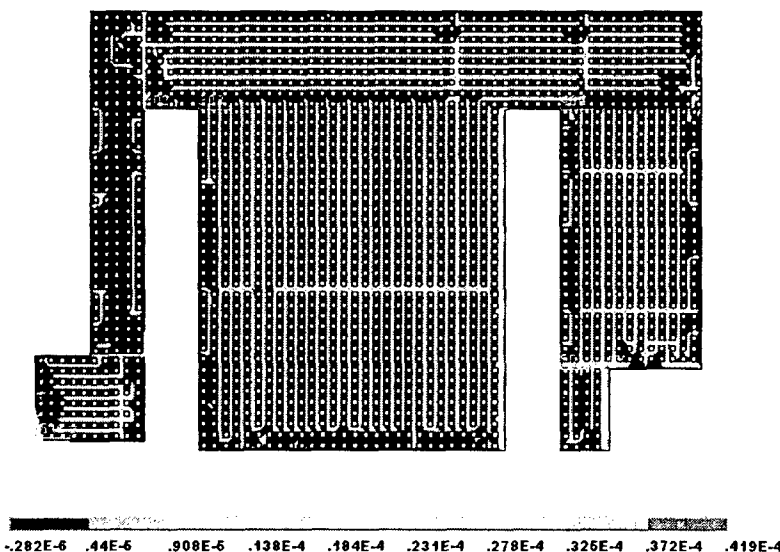
**Fig. 3-33:** Pressure distribution due to squeeze film damping - ambient pressure on the perforations. A gap thickness of 2 μm is assumed. Notice the lower pressures compared to Fig. .

Effect of hole size

The high density of perforations allows the fluid to escape from underneath the G-sensor easily, creating a low damping force. In order to increase the damping in the structure to prevent stiction, we suggest that the area of the perforations in the device be minimized. A hole size of 10 micrometers leads to a damping ratio of 4.2712, which is a significant increase from 0.2125. There are limits to this, as the perforations appear to be needed in order to release the structure from the substrate during fabrication.

		ξ	
	Gap Width	2 µm	4 µm
Hole Size	25 um	0.2178	0.0757
	20 um	0.3182	0.1960
	15 um	0.8884	0.6117
	10 um	4.1877	2.7428
	7 um	13.0767	8.4066

Fig. 3-34: Effect of the hole size on the damping ratio. Decreasing the hole size can be seen to increase damping.

Damped Response

Here we used the results of the previous section to model the effect of the damping on the transient response of the device, when subjected to a half-sine shock pulse. By including damping in the model, we can see that decreasing the size of the hole has a large effect on the maximum deflection of the device.
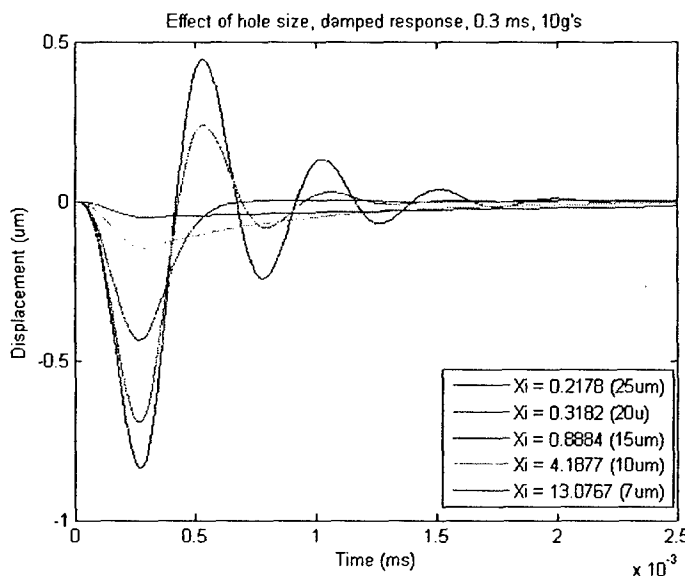
Fig. 3-35: Effect of the hole size on the transient response of the G-Sensor, when subjected to a half sine shock pulse.

We are also interested in determining the shock pulse which will cause the G-sensor to contact the substrate. To this end, we determine the shock level at which the device will touch the substrate.

Table and Fig. show that decreasing the hole size has a significant effect on the shock resistance of the G-Sensor. It also shows that the larger gap size will contact the substrate at a lower

Hole Size	Gap 2 μm	4 μm
25 μm	23.95 g	19.83 g
20 μm	28.86 g	25.15 g
15 μm	45.82 g	42.96 g
10 μm	137.08 g	102.80 g
7 μm	397.61 g	265.25 g

Table 3-15: Shock level that causes the G-sensor to contact the substrate.
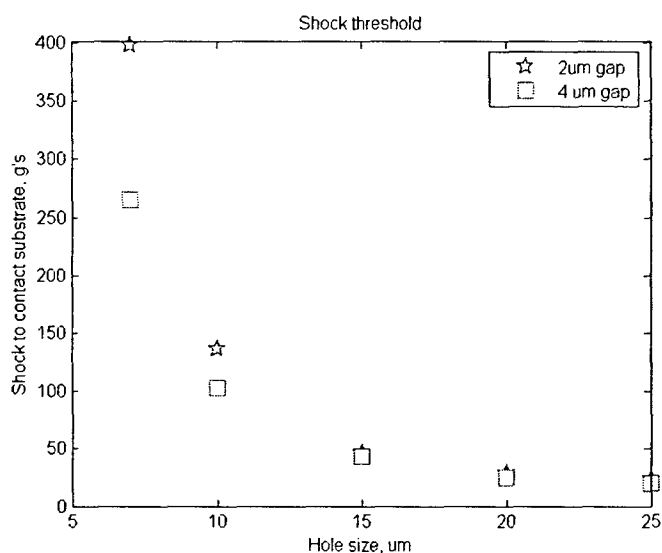
Fig. 3-36: Shock level that causes the G-sensor to contact the substrate.

Recommendations

Since it may not be possible to remove the holes completely, their size should be decreased to as small as technologically possible, with the total number of holes remaining the same. This will allow the device to be released from the substrate and will maximize damping. In addition, the increase in mass that occurs when the hole area is decreased will lead to a more sensitive G-sensor. Adding mechanical stops or surface coatings to prevent stiction are other alternatives; however that is beyond the scope of this work.

References

[1] Cochran, Kevin R., Lawrence Fan, Don L. DeVoe. "High-power optical microswitch based on direct fiber actuation." Sensors and Actuators A 119 (2005) 512–519.

[2] Senturia, Stephen. "Microsystem Design" Kluwer (2000).

[3] Hsu, Tai-Ran "MEMS and Microsystems Design and Manufacture". McGraw-Hill (2001).

[4] Steinberg, David. "Vibration Analysis for Electronic Equipment" John Wiley. & Sons, 3rd ed. (2000).

[5] Barry Controls: Engineered Design Capabilities: Technical References: Vibration Basics   -   Operating   Principles. <http://www.barrycontrols.com/engineereddesigncapabilities/ technicalreferences/vibrationbasicsoperatingprinciples/>, Barry Controls, (2004).

[6] Srikar, V T, and Senturia, Stephen D. "The Reliability of Microelectromechanical Systems (MEMS) in Shock Environments." Journal of Microelectromechanical Systems, 11 (2002), 206-214.

[7] "Polymicro Technologies > Catalog > Mechanical Stress and Fiber Strength" <http://www.polymicro.com/catalog/2_25.htm>

[8] Autocad drawing, "CC Beam - DRIE5_chip_suny_new.dwg", Obtained from ONR.

[9] Kovacs, Gregory T, "Micromachine Transducers Sourcebook". McGraw Hill (1998). Pg 26.

[10]   Van Spengen, W M, Robert Puers, Ingrid De Wolf. "A physical model to predict stiction in MEMS." Journal of Micromechanics and Microengineering 12 (2002) 702-13.

[11]   Hsu, Tai-Ran. "MEMS and Microsystems Design and Manufacture". McGraw-Hill (2001).

[12]   Enikov, Eniko T, Shantanu Kedar, Kalin Lazarov. "Analytical Model for Analysis and Design of V-Shaped Thermal Microactuators." Journal of Microelectromechanical Systems, 14 (2005), 788-798.

[13]   Que, Long, Jae-Sung Park, Yogesh B Gianchandani. "Bent-Beam Electrothermal Actuators – Part I: Single Beam and Cascading Devices." Journal of Microelectromechanical Systems. 10 (2001) 247-54.

[14]   Blech, J.J. "Isothermal Squeeze Films," Journal of Lubrication Technology, Vol. 105, 1983, pp 615-620.

[15]   ANSYS Release 9.0 Documentation – Fluids Guide – Chapter 16. This Film Analysis.

[16]   Homentcovschi, Dorel, R.N. Miles. "Viscous damping of perforated planar micromechanical structures." Sensors & Actuators A 119 (2005) 544-552.

Sub Task 4: Numerical study of stiction phenomenon in MEMS

Performer: Timothy Singler
Organization: SUNY Binghamton

Introduction

Stiction plays an important rule in the manufacturing reliability and the performance of MEMS and NEMS devices. The small characteristic length scales of micro devices emphasize the effect of surface forces over the volume forces which in turn results in stiction problems. Surface forces of various origins can contribute to stiction; these include capillary, Van der Waals, electrostatic and Casmir forces. Capillary forces result from the presence of water traces that appear within the structure during manufacturing processes or as a result of capillary condensation of water from the humid environment. The Van der Waals forces could be attractive or repulsive depending on the separating distances between different surfaces of the structure. When the stiction forces become larger than the actuating force for the structure, adhesion of the surfaces can occur resulting in fabrication failure or mal function of the MEMS device.

Recently, a great deal of research has been directed at understanding the fundamentals of stiction and at constructing models that describe stiction behavior. The stiction energy was first measured by [1], by using an array of cantilevered beams as a test device. [2] studied the stiction of polysilicon microbeams in a controlled humidity environment. They used supercritical CO_2 drying for freeing the beams. They found that the supercritical CO_2 drying is able to free a beam of length up to 2 mm length. Also, they found that the surface interaction energy increases exponentially with the relative humidity. [3] derived a stiction model for suspending polysilicon microbeams that includes the effect of the residual stress gradients and the post release temperature. They used three different materials for the substrate: bare silicon, unmodified smooth polysilicon and grain hole polysilicon. They found that the grain hole polysilicon substrate tends to decrease the effect of the residual stress gradient on stiction as a form of lower surface interaction energy. [4] discussed the theoretical limit on the freestanding length of cantilevered beams, taking into account the acceleration, Casmir and coulomb forces. They tabulated a set of equations to determine the maximum length of the beam

for which no stiction failure could occur. [5] studied the contact deformation of a plate-like clamped/clamped micro beam and derived a relation between the surface interaction energy and the bending moment at the edge of the contact zone. they also found a lower limit for the gap between the micro structure and the substrate and this limit is proportional to the structure length and to the square root of the surface interaction energy. [6] found that for coated hydrophobic beams, adhesion is independent of RH up to a threshold value that depends on the coating used. [7] and [8] introduced a physical model for investigating the sensitivity of microstructures to stiction. The model included the capillary energy, Van Der Waals forces, electrostatic forces and H-bond forces. It also took account of the roughness of the surface by assuming a Gaussian distribution of the separation distance between the two surfaces. [9] studied the effect of the surface tension on the performance of a SOI (silicon on insulator) beam and discovered that the adhesion forces are directly proportional to the surface tension of the last liquid used before drying.

Background

Equilibrium interfaces

Capillarity

Capillarity concerns the motions and shapes of interfaces in response to the presence of surface forces. An equilibrium capillary surface refers to a surface (either liquid-liquid or liquid-gas) whose shape is dictated by the equilibrium between surface and body forces. The formation of equilibrium capillary surfaces requires an amount of free energy that is ultimately stored in the interface itself. Any change in the equilibrium shape will result in a change in the equilibrium free energy of the interface; thus an equal amount of work will be needed to be performed on the interface in order to change its equilibrium free energy by the same amount. The equilibrium shape of the interface is related to the pressure difference ΔP across the interface by the Young-Lap lace equation,

$$\Delta P = \gamma_{lv} \left(\frac{1}{R_1} + \frac{1}{R_2} \right) \tag{1}$$

where R_1 and R_2 are the principal radii of curvature, γ_{lv} is the surface tension of the liquid.

Effect of vapor pressure change on the equilibrium of interfaces

A change in the vapor pressure of the liquid will result in a change in the pressure drop across the interface. This in turn will result in a change of the equilibrium shape of the interface. The relation between the vapor pressure and the equilibrium shape of the interface can be derived from equilibrium thermodynamics and is known as Kelvin's equation:

$$R_g T \ln\left(\frac{P}{P^o}\right) = V_m \gamma_{lv}\left(\frac{1}{R_1} + \frac{1}{R_2}\right) \tag{2}$$

where R_g is the gas constant, P^o is the vapor pressure of the liquid and V_m is the molar volume of the liquid. Kelvin's equation can be used to express the relationship between the relative humidity RH and the change in the equilibrium shape. Since $RH = \dfrac{P}{P^o}$, Kelvin's equation becomes

$$R_g T \ln(RH) = V_m \gamma_{lv}\left(\frac{1}{R_1} + \frac{1}{R_2}\right) \tag{3}$$

This may be specialized to a spherical section of L/V interface by letting $R = R_1 = R_2$ which leads to

$$R_g T \ln(RH) = \frac{2 V_m \gamma_{lv}}{R} \tag{4}$$

Solid liquid vapor interfaces

Consider a static contact line formed by a liquid/vapor/solid triple junction and characterized by a contact angle θ_c. Consider the virtual infinitesimal displacement of that contact line such that liquid displaces vapor and there is an increase ΔA in the solid/liquid (S/L) interfacial area and a commensurate decrease in the solid/vapor (S/V) interfacial area. The associated change ΔG in the Gibbs free energy of the system is then given by

$$\Delta G = \Delta A\left(\gamma_{sl} - \gamma_{sv}\right) + \Delta A \gamma_{lv} \cos\left(\theta_c\right) \tag{5}$$

Since the triple junction region is in equilibrium, ΔG and Young's equation follows:

$$\left(\gamma_{sl} - \gamma_{sv}\right) + \gamma_{lv} \cos\left(\theta_c\right) = 0 \implies \gamma_{sv} - \gamma_{sl} = \gamma_{lv} \cos\left(\theta_c\right) \tag{6}$$

Consider a solid surface of fixed area A_s and assume that an area A_{sl} of A_s is wetted by a liquid. We emphasize here that A_{sl} is capable of variation while A_s is a constant. The total Gibbs free energy G associated with the surface is given by

$$G = \left(A_s - A_{sl}\right)\gamma_{sv} + A_{sl}\gamma_{sl} = A\gamma_{sv} + A_{sl}\left(\gamma_{sl} - \gamma_{sv}\right) = A\gamma_{sv} - A_{sl}\gamma_{lv} \cos\left(\theta_c\right) \tag{7}$$

where use has been made of Young's equation. Assuming that the S/V interfacial energy is constant so that the term $A\gamma_{sv}$ is also constant, the Gibbs free energy of the surface may be written as

$$G = G_o - A_{sl}\gamma_{lv} \cos\left(\theta_c\right) \tag{8}$$

This is because the total energy G can only be defined to within an arbitrary constant, and the constant term $A\gamma_{sv}$ may be absorbed by that constant.

Surface interaction energy measurement

Mastrengelo et. al.[1] proposed a novel technique to measure the surface interaction energy. The measuring technique is applied using an array of cantilevered beams of different length whereby a force is applied to each beam until it contacts the underlying substrate. The bending (elastic) energy U_E of an individual beam can be calculated if the unadhered length s of the beam is known. Minimizing the total energy $U_T = U_E + \Gamma(l - s)$ with respect to s then yields the surface interaction energy density $\Gamma = \dfrac{-1}{w} \dfrac{\partial U_E}{\partial s}$.

Analytical support for the above measurement technique requires solution of the elastic beam equation

$$\frac{\partial^4 u}{\partial x^4} = 0 \tag{9}$$

subject to the boundary conditions

$$u(x = 0) = 0, u'(x = 0) = 0, u(x = s) = -h, u'(x = s) = 0 \qquad (10)$$

here u is the deflection of the beam at the axial position x, h is the seperation distance between the beam base and the substrate, and w is the beam width. The resulting solution for the shape of the deformed beam is

$$u(x) = h\left(\frac{x}{s}\right)^2 \left(3 - 2\frac{x}{s}\right) \qquad (11)$$

The elastic energy may be calculated from the above solution by integrating the deflection equation as follows:

$$U_E = \frac{EI}{2} \int_0^s \left(\frac{\partial^2 u}{dx^2}\right)^2 dx \qquad (12)$$

where E is modulus of elasticity and I is the second moment of inertia.

Another possible configuration for the beam deflection is the arc shape (Fig. 1) in which the beam contacts the substrate only at its tip De Boer et al.[6] investigated both configurations and reached the conclusion that the s-shape beam is sufficient for the study of stiction problem in microbeams.

Surface Evolver

The Surface Evolver is an interactive program for the study of surfaces shaped by interfacial and other energies. A surface is modeled as a union of triangular elements. The program has no user friendly interface, and an initial surface must be defined in a data file. This surface is then evolved towards minimal energy by the method of gradient descent.

Modeling

Stiction during Manufacturing processes

The primary objective of the current work is to study the effect of capillary stiction on the operation of a thermally actuated switch. The switch is actuated by the ohmic heating of a supporting beam, the resulting deformation of which actuates a central

beam element to complete either an electrical or optical coupling. A micrograph of the switch is shown in Fig. 4-1.
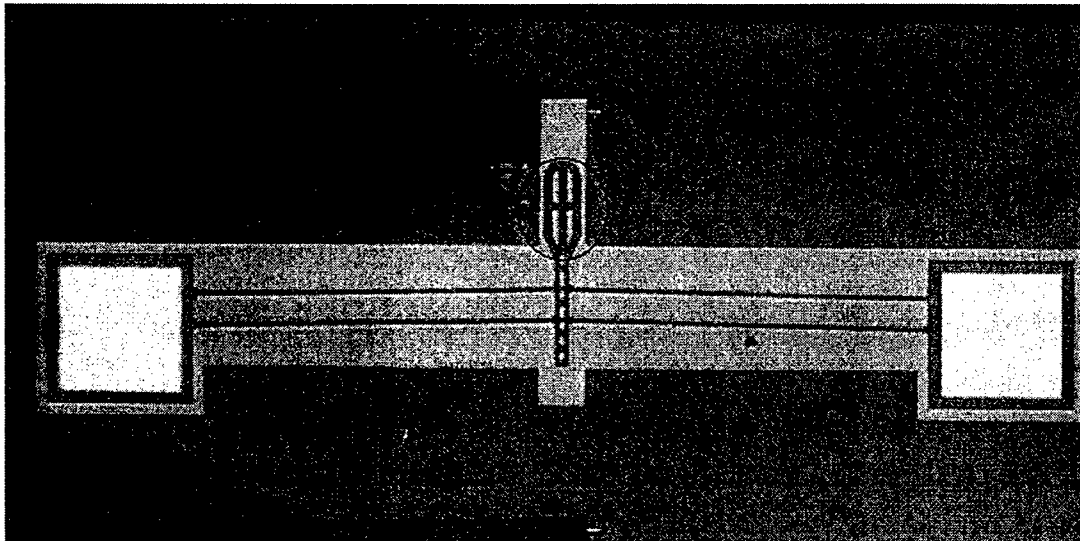

Fig. 4-1. Micrograph of thermally actuated switch.

In principle, stiction could occur between any and all of the beam structures that comprise the switch mechanism. However, due to its complexity, a Surface Evolver model of capillary stiction between all elements of the complete switch and the underlying substrate is formidable. Instead, we focus on a Surface Evolver model of the primary actuation element, the central beam. Two general models of this beam are considered: (1) a rigid beam with either a round or flat tip and which is inclined with respect to the substrate; (2) an elastic beam which deforms due to stiction forces. In both models, the dimensions of the beam can be varied. Surface Evolver models were built for four specific cases of the two general models described above. These are described below.

Case 1

This case (Figure 4-2) is a rigid beam with flat tip. The effects of angle of inclination and beam tip-substrate distance on the stiction force and surface interaction energy were explored.
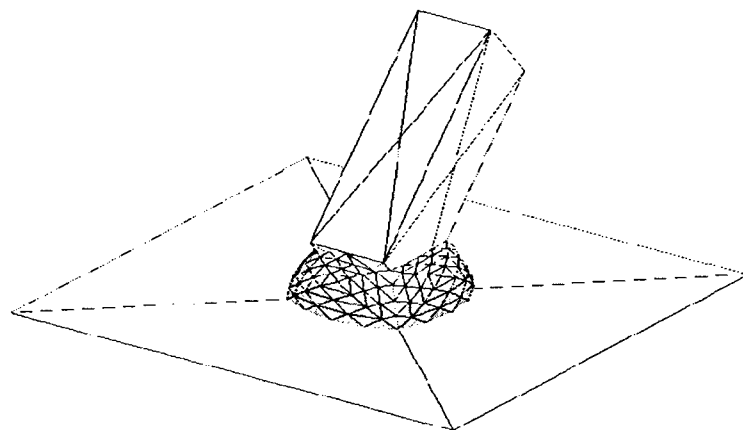
Fig. 4-2. Case 1: Stiction model for an inclined rigid beam with straight tip.

Case 2

This case (Figure 4-3) is a rigid beam with curved tip. The effects of angle of inclination and beam tip-substrate distance on the stiction force and surface interaction energy were explored.
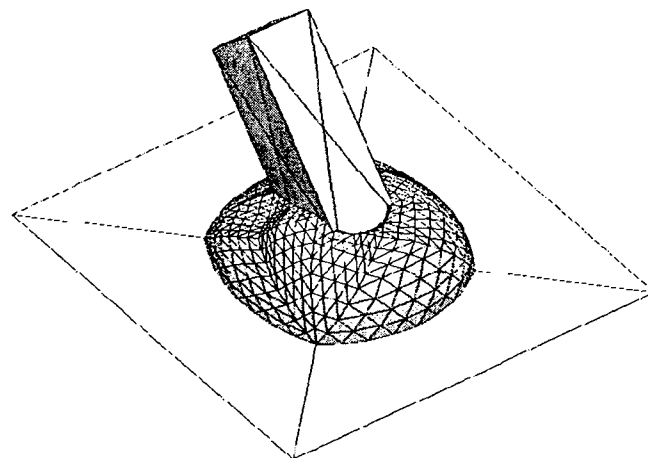

Fig. 4-3. Case 2: Stiction model for an inclined rigid beam with curved tip.

Case 3

This case (Figure 4-4) is a rigid beam with curved tip with zero angle of inclination. Figure 5 shows a schematic drawing for this case. The liquid is pinned along curve 2 and along the sides of the beam; the contact line is free along curve 1. The stiction is characterized by the parameters F_z (force in z-direction), F_y, (force in y-direction) and U_A (surface interaction energy); the horizontal force component F_x is zero by symmetry. The force components are calculated by the method of virtual displacement. The surface interaction energy U_A is defined as the total interfacial energy formed between condensed phases. The liquid/vapor interfacial energy (surface tension) is denoted by γ_{lv} and the liquid volume as V. The contact angles of the liquid on the beam and substrate materials are denoted by θ_b and θ_s, respectively. The geometry of the beam is characterized by its width w and its height h above the substrate.
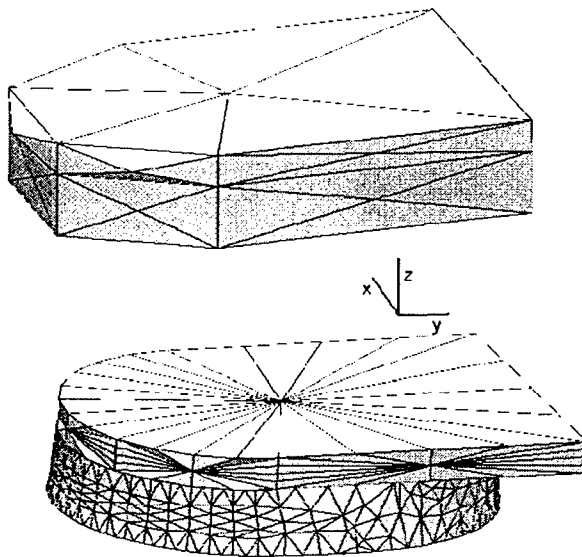

Fig. 4-4. Case 3: Stiction model for a rigid beam with curved tip.

There are three relevant interfacial areas, the solid/liquid interfacial area A_{sl}^B between the beam and liquid, the solid/liquid interfacial area A_{sl}^S between the substrate and liquid and the liquid/vapor interfacial area A_{lv}. The total interfacial energy is the sum of the

liquid/vapor interfacial energy and the interfacial energies of the condensed phases (surface interaction energies). Thus

$$E_T = E_{lv} + E_{sl}^B + E_{sl}^S \qquad (13)$$

Making use of equation (6), this expression may be expressed as

$$E_T = \int_{A_{l_v}} \gamma_{lv} dA_{lv} - \int_{A_{sl}^B} \gamma_{lv} \cos(\theta_b) dA_{sl}^B - \int_{A_{sl}^S} \gamma_{lv} \cos(\theta_s) dA_{sl}^S \qquad (14)$$

where E_T is the total energy of all interfacial regions, E_{lv} is the liquid vapor interfacial energy, E_{sl}^B is the interfacial energy of the beam/liquid interface and E_{sl}^S is the interfacial energy of the substrate/liquid interface. Surface Evolver provides a numerical approximation to (14). Since Surface Evolver provides E_T, the surface interaction energy can be calculated as

$$U_A = E_T - \gamma_{lv} A_{lv} \qquad (15)$$
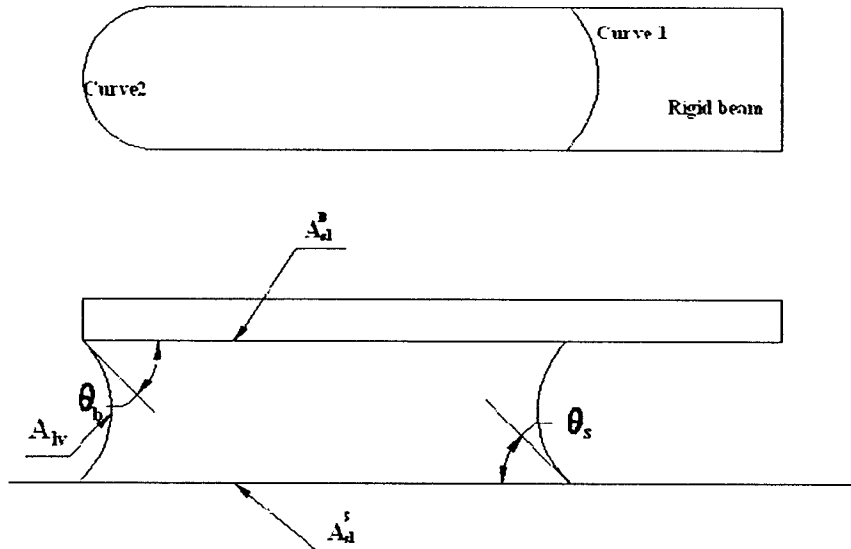
Fig. 4-5. Schematic drawing of case 3

Figures 4-6 ~ 4-8 show the variations of F_z , F_y and U_A for a beam of width 50 μm. F_z may be seen to increase as V increases. This is due to the increase in the length of the contact lines along the straight edges of the beam. F_z also increases as θ_b

increases (with θ_s held fixed) in the range $0 \le \theta_b \le \dfrac{\pi}{2}$. F_y is not affected by the change

in V but decreases as θ_b increases in the range $0 \le \theta_b \le \dfrac{\pi}{2}$. This is because the shape of

the curved interfaces (curves 1 and 2 in Fig. 5) do not change with V provided that V is

sufficiently large. For this reason, F_y is insensitive to changes in V. U_A increases as U_A

increases and decreases as θ_b increases in the range $0 \le \theta_b \le \dfrac{\pi}{2}$; the latter behavior is

expected since $E_{sl}^B = -\int_{A_{sl}^B} \gamma_{lv} \cos(\theta_b) dA_{sl}^B$. The increase in U_A with V is due to the

increase in A_{sl}^B with increasing V.
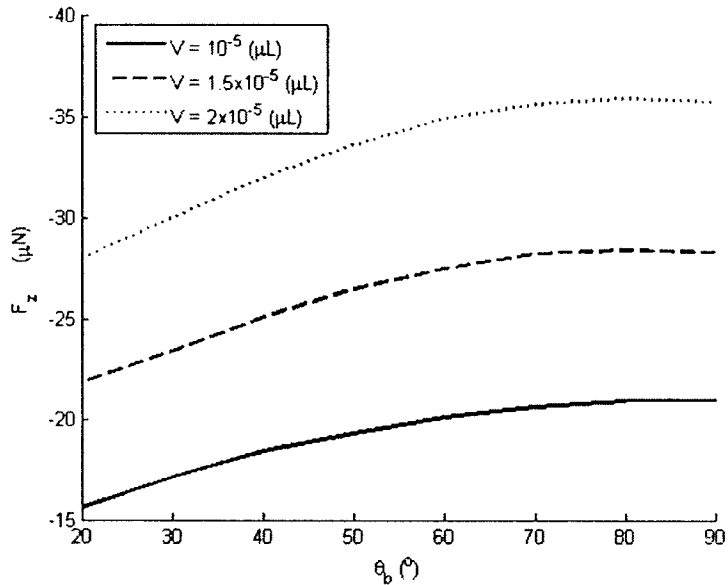
Fig. 4-6. F_z versus θ_b and V for a beam of width 50 μm.
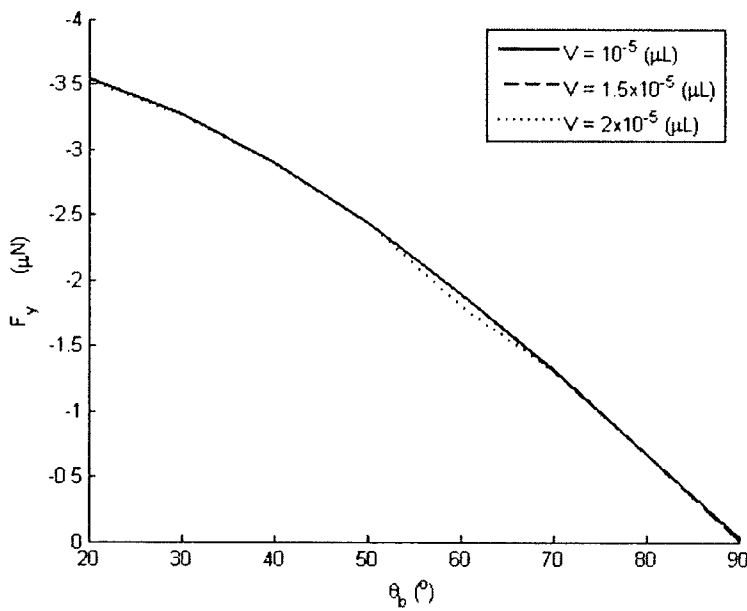
Fig. 4-7. F_y versus θ_b and V for a beam of width 50 μm.
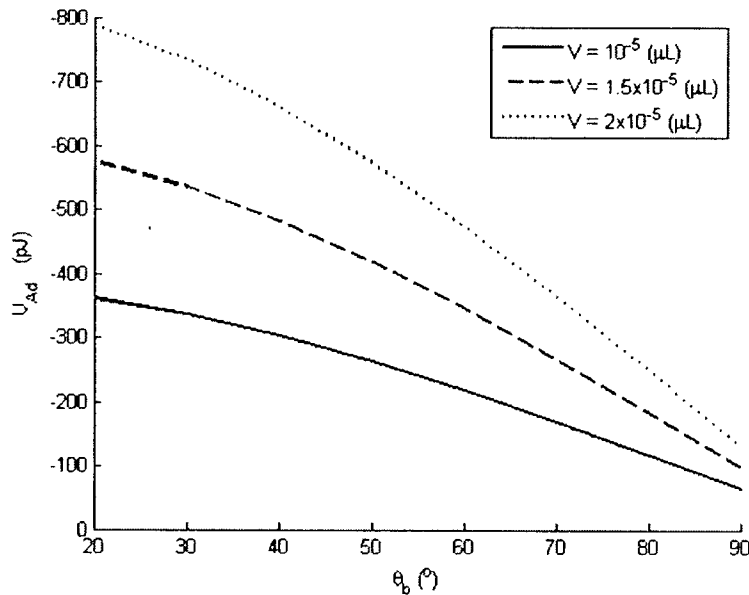
Fig. 4-8. U_A versus θ_b and V for a beam of width 50 μm.

Figures 4-9 ~4-11 show the variations of F_z , F_y and U_A for a beam of width 90 μm. By comparing this set of figures to the previous set, it can be seen that as the width of the

beam increases for a fixed value of V, F_z decreases. This is due to the decrease in the length of the contact lines along the straight edges of the beam. F_y increases as the width of the beam increases. This is due to the increase in the length of the contact lines along curves 1 and 2. U_A increases as the width of the beam increases This is due to the increase in A_{sl}^B.
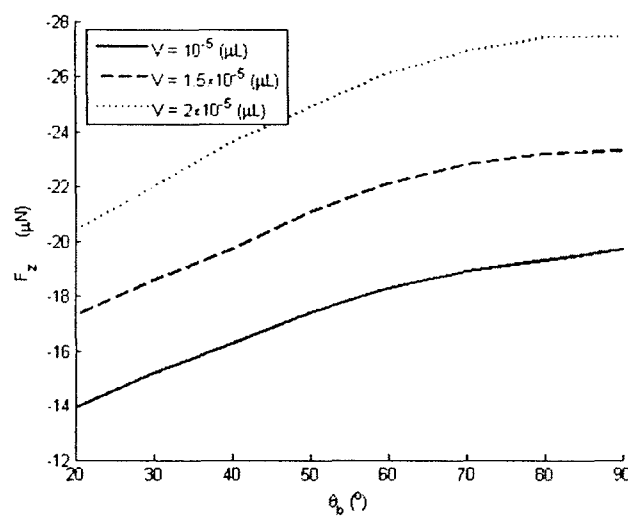

Fig. 4-9. F_z versus θ_b and V for a beam of width 90 μm.
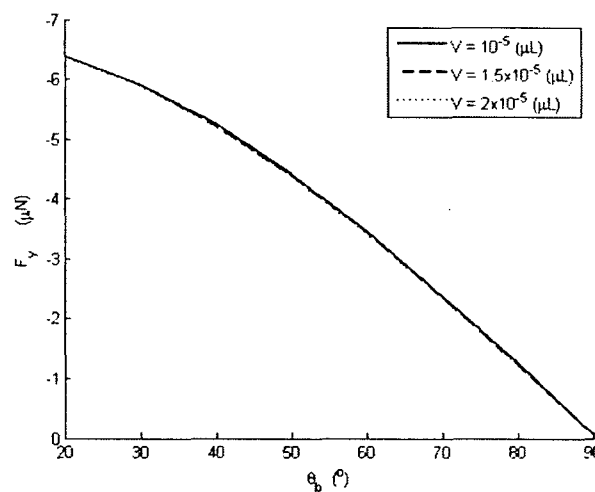
Fig. 4-10. F_y versus θ_b and V for a beam of width 90 μm.
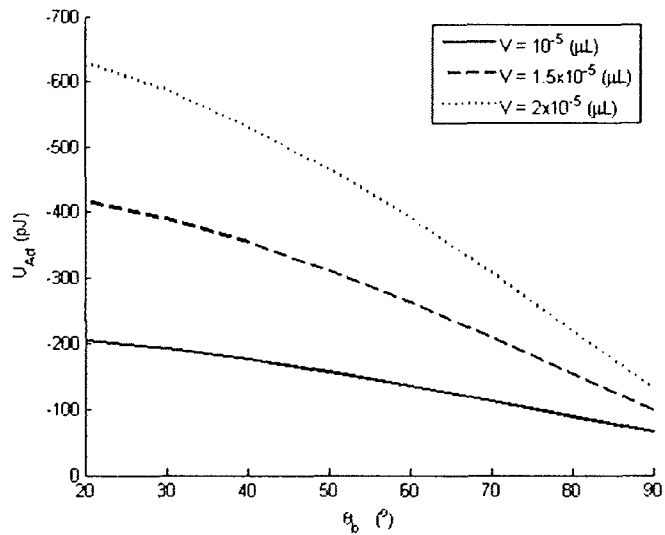
Fig. 4-11. U_A versus θ_b and V for a beam of width 90 μm.

Case 4

Figure 4-12 shows an elastic beam in contact with the underlying substrate due to a capillary bridge. This model has been widely used to investigate the effect of stiction on the performance of MEMS devices. Most of the existing literature relies on crude approximations to the surface interaction energies. We will exploit this model and use Surface Evolver to accurately calculate the forces and surface interaction energies. By including the elastic energy of the beam, we will be able to accurately calculate the total system energy. By minimizing this energy, we will be able to determine the length of contact between the beam and underlying substrate. By determining the critical system parameters that insure that there is no beam/substrate contact, we hope to identify a safe design space to avoid stiction.
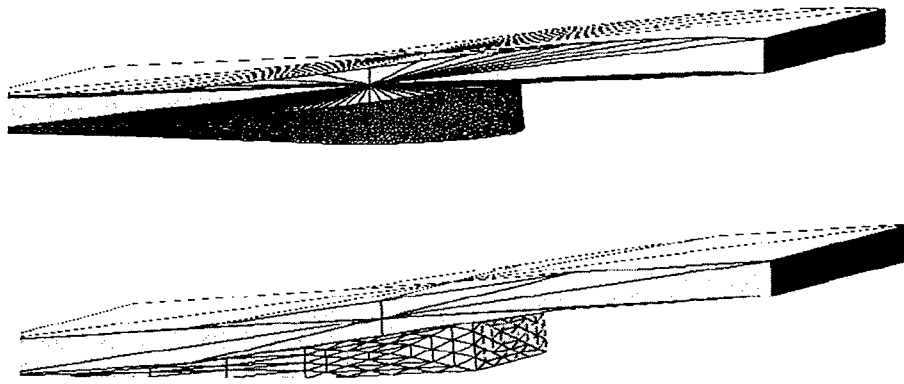
Fig. 4-12. Case 4: Stiction effect on flexible, cantilevered beam.

In Use stiction

Section problem occur in MEMS either during Manufacturing processes or during the operation of MEMS devices. The former is known as in-use stiction. The reliability of MEMS device can be improved making use of anti-stiction coating. Anti-stiction coating usually applied to MEMS surfaces in order to improve the surface characteristic like surface energy, hydrophobiciy and surface roughness. The successful coating can achieve by improving the characteristics in such away the surface will have high contact angle, low Van der Waals interaction energy and acceptably high surface roughness. In the current work, a mathematical model has been built in order to achieve parametric studies of in-use stiction phenomena. In-use stiction occur when the adhesion force is greater than the restoring force of the structure or when the adhesion energy is considerably high. In the current model, stiction phenomena is characterized by the adhesion force and the adhesion energy. The effect of different parameters on stiction likelihood has been studied. The parameters are relative humidity, contact angles, surface roughness, Hamaker constant (associated with Van der Waals interaction), modulus of elasticity and Hardness of MEMS materials.

Mathematical formulation

Surface roughness
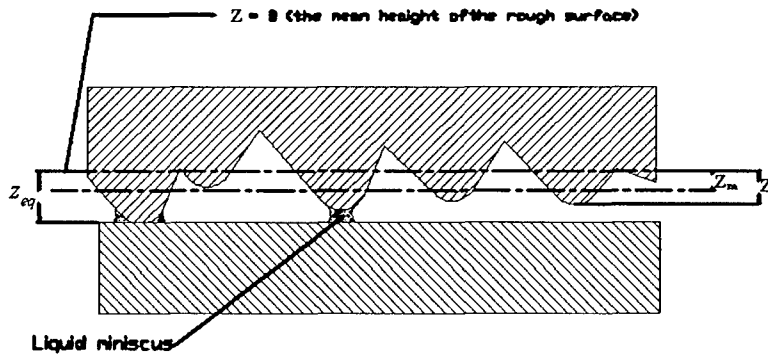
Fig. 4-13. Rough and smooth surfaces in contact

As shown in figure 4-13, Two rough surfaces in contact can be modeled as one surface is rough and elastic and the other surface is rigid and smooth [10]. The surface roughness of the surface is modeled following Greenwood and Williamson model [11], the surface roughness has been modeled assuming that all the asperities have the same radius of curvature and the surface's heights distribution is Gaussian. The properties of the equivalent rough surface are as follows

$$\sigma^2 = \sigma_1^2 + \sigma_2^2 \tag{16}$$

$$\frac{1}{E^*} = \frac{(1-\upsilon_1^2)}{E_1} + \frac{(1-\upsilon_2^2)}{E_2} \tag{17}$$

Where:

σ is the standard deviation of the equivalent rough surface height distribution.

σ_1 is the standard deviation of the first surface height distribution.

σ_2 is the standard deviation of the second surface height distribution.

E^* is the equivalent surface modulus of elasticity.

E_1 is the first surface modulus of elasticity.

E_2 is the second surface modulus of elasticity.

υ is Poisson ratio.

Whitehouse et. al. [12] proposed a probability distribution function for asperity's peak height distribution and they introduce a formula for the statistical property of the asperity peak distribution.

$$\phi(z) = \frac{1}{4\sigma\sqrt{2\pi}} e^{-\left(z^2/2\sigma^2\right)} \left[1 + erf\left(\frac{z}{\sigma\sqrt{2}}\sqrt{\frac{1-\rho}{1+\rho}}\right)\right]^2 \tag{18}$$

Where ρ is function of the sampling interval (l) and the spatial autocorrelation β^*

$$\rho = \exp\left(-\frac{l}{\beta^*}\right) \tag{19}$$

$$\sigma_p = 0.9\sigma \tag{20}$$

$$R = \frac{\beta^{*2}}{20\sigma} \tag{21}$$

$$\sigma_p R \eta = \text{constant} \tag{22}$$

Where: σ_p is the standard deviation of the peak height distribution, R is the mean peak radius, η is the peak density.

McCool et. al. [13] proposed a relation between σ, σ_b, R and η

$$\sigma^2 = \sigma_p^2 + \frac{3.717e^{-4}}{\eta^2 R^2} \tag{23}$$

With $\sigma_p = 0.9\sigma$, one can solve for $\sigma_b R \eta$.

$$\sigma_b R \eta = 40.2e^{-3} \tag{24}$$

Structural forces

When two surfaces have contact their asperities will indent each other which will result in a reaction forces that try to resist the indentation process. Since the asperities peak is assumed to have a constant radius of curvature then Hertzian contact theory can be applied.
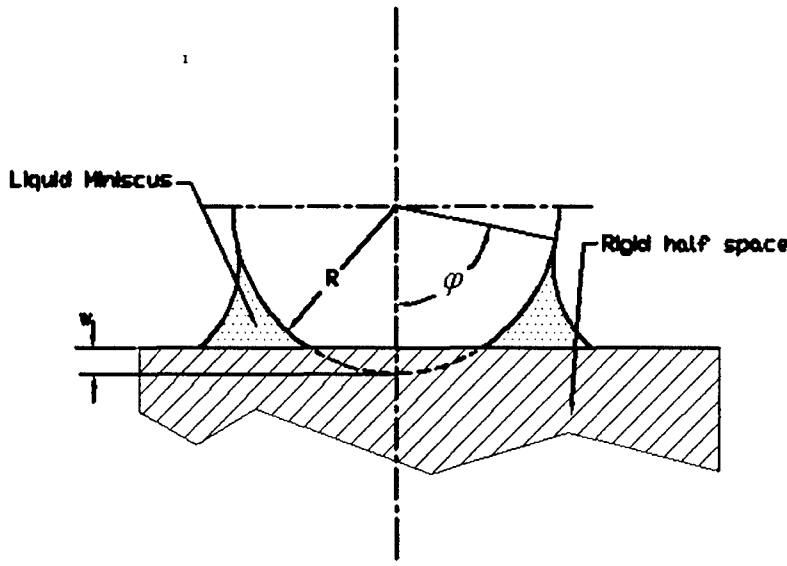
Fig. 4-14. Elastic sphere indenting smooth and rigid surface.

The literature contains empirical formulae for the elastic, elasto-plastic and fully elastic forces of the Hertzian contact [14-15]. The structural force P(z) is

$$P(z) = \begin{cases} \dfrac{4}{3} E\, R^{\frac{1}{2}} (z - z_{eq})^{\frac{3}{2}} & z \leq z_{eq} + w_c \\[2mm] 1.03 \left(\dfrac{z - z_{eq}}{z_c - z_{eq}} \right)^{1.425} P_c & z_{eq} + w_c \prec z \leq z_{eq} + 6w_c \\[2mm] 1.40 \left(\dfrac{z - z_{eq}}{z_c - z_{eq}} \right)^{1.263} P_c & z_{eq} + 6w_c \prec z \leq z_{eq} + 110\, w_c \\[2mm] \dfrac{3}{K} \left(\dfrac{z - z_{eq}}{z_c - z_{eq}} \right) P_c & z \succ z_{eq} + 110\, w_c \end{cases} \qquad (25)$$

Where $P_c = \dfrac{4}{3} E\, R^{\frac{1}{2}} (z_c - z_{eq})^{\frac{3}{2}} r_1$ and K is a function of the Poison ratio and

$$z_c = z + \left(\frac{(\pi K' H)}{(2 E^*)} \right)^2 R \qquad (26)$$

Where H is the hardness of the surface and K' is a constant depends on the Poisson ratio
$K = 0.454 + 0.41\upsilon$.

The total reaction force per nominal surface area applied on the rough surface is

$$F_e(z_{eq}) = \eta \left(\int_{z_{eq}}^{z_{eq}+w_c} \frac{4}{3} E R^{\frac{1}{2}} (z - z_{eq})^{\frac{3}{2}} \phi(z) dz + \int_{z_{eq}+w_c}^{z_{eq}+6w_c} 1.03 \left(\frac{z - z_{eq}}{z_c - z_{eq}} \right)^{1.425} P_c \phi(z) dz + \right.$$

$$\left. \int_{z_{eq}+6w_c}^{z_{eq}+110w_c} 1.40 \left(\frac{z - z_{eq}}{z_c - z_{eq}} \right)^{1.263} P_c \phi(z) dz + \int_{z_{eq}+110w_c}^{\infty} \frac{3}{K} \left(\frac{z - z_{eq}}{z_c - z_{eq}} \right) P_c \phi(z) dz \right)$$

(27)

**Capillary Condensation**
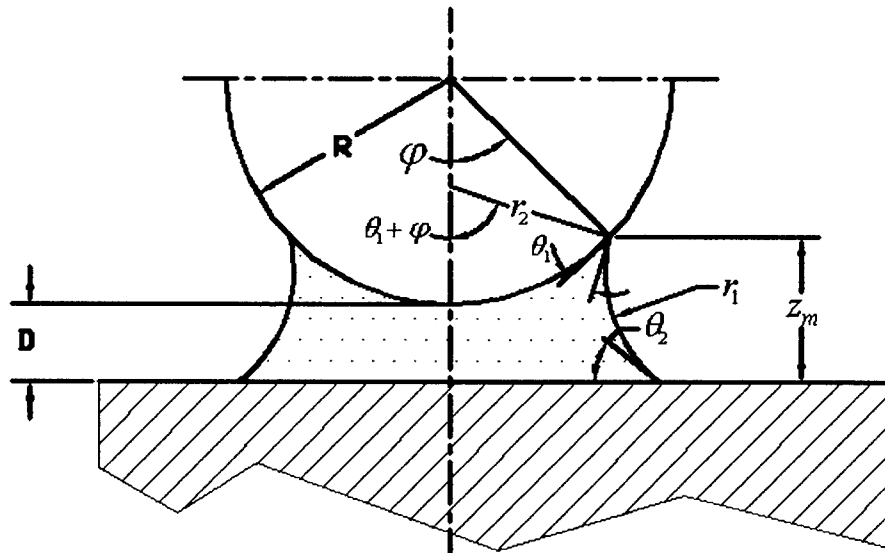
Fig. 4-15. Liquid meniscus between sphere and half space.

Orr at. al. [16] studied a liquid meniscus between sphere and half space where the sphere is just touching the half space without indentation. In the current analysis Orr. at. al. analysis has been generalized to include all possible configurations of the separating distance between the sphere and the half space.

Figure 4-15 shows the geometry of sphere and half space that they have a separation distance D between them. Where $D = z_{eq} - z$, r1 is the meridional radius, r2 is the azimuthal radius, θ_1 is the contact angle between the liquid and the sphere's surface, θ_2 is the contact angle between the liquid and the flat surface, φ is the filling angle of the liquid over the sphere's surface, R is the radius of the sphere and z_m is the maximum height of the liquid meniscus.

By analyzing the geometry of Fig. 4-15, ones can find that The azimuthal and the meridional radii

$$r_1 = -\frac{R(1 - \cos\varphi) + D}{\cos(\theta_1 + \varphi) + \cos(\theta_2)} \tag{28}$$

$$r_2 = \frac{R\sin(\varphi)}{\sin(\theta_1 + \varphi)} \tag{29}$$

Given the contact angles, the separation distance D and the radius of the sphere R, ones can solve for the filling angle making use of the Kelvin's equation [17-18]

$$\frac{R_g T}{V_l} \ln(RH) = \gamma \left(\frac{1}{r_1} + \frac{1}{r_2} \right) \tag{30}$$

Where R_g is the real gas constant, T is the temperature of the air, V_l is the liquid molar volume, RH is the relative humidity of the air and γ is the surface tension of the liquid.

The meniscus forces are consist of the surface tension forces and the Lap lace pressure force.

$$f_c(z) = \begin{cases} 2\pi\gamma_{lv}R\sin(\varphi)\sin(\theta_1 + \varphi) - \pi\dfrac{R_g T}{V_l}\ln(RH)R^2\sin^2(\varphi) & z \leq z_{eq} \\[2mm] 2\pi\gamma_{lv}R\sin(\varphi)\sin(\theta_1 + \varphi) - \pi\dfrac{R_g T}{V_l}\ln(RH)\left((R + D)^2 - R^2\cos^2(\varphi)\right) & z \geq z_{eq} \end{cases} \tag{31}$$

The adhesion energy is defined as the difference between the interfacial energies of the state of contact and the state of infinite separation [19]

$$E_1 = \gamma_{sv1}A_{sv1} + \gamma_{sv2}A_{sv2} + \gamma A_{lv} - \gamma\cos(\theta_1)A_{sl1} - \gamma\cos(\theta_2)A_{sl2} \tag{32}$$

$$E_2 = \gamma_{sv1}A_{sv1} + \gamma_{sv2}A_{sv2} \tag{33}$$

$$e_c(z) = E_2 - E_1 \tag{34}$$

$$e_c(z) = \gamma \cos(\theta_1) A_{sl1} + \gamma \cos(\theta_2) A_{sl2} - \gamma A_{lv} \tag{35}$$

Where γ_{sv1} is the interfacial energy of solid vapor interface of the sphere surface, γ_{sv2} is the interfacial energy of the solid vapor interface of the substrate, A_{sv1} is the total surface area of the sphere, A_{sv2} is the total surface area of the substrate, A_{sl1} is the solid/liquid interface between the liquid and the sphere surface, A_{sl2} is the solid/liquid interface between the liquid and the substrate surface and A_{lv} is the liquid/vapor interfacial energy.

$$A_{sl1} = \begin{cases} 2\pi R^2(1 - \cos(\varphi)) & z \leq z_{eq} \\ 2\pi(R^2(1 - \cos(\varphi)) - R(z - z_{eq})) & z \geq z_{eq} \end{cases} \tag{36}$$

$$A_{sl2} = \begin{cases} \pi(R\sin(\varphi) + r_1\sin(\theta_1 + \varphi) - r_1\sin(\theta_2))^2 & z \leq z_{eq} \\ \pi((R\sin(\varphi) + r_1\sin(\theta_1 + \varphi) - r_1\sin(\theta_2))^2 - R^2 + (R + z_{eq} - z)^2) & z \geq z_{eq} \end{cases} \tag{37}$$

$$A_{lv} = 2\pi \int_{z_{eq}}^{z_{eq} - r_1(\cos(\theta_1) + \cos(\theta_1 + \varphi))} r_1(\sin(\varphi) + \sin(\theta_1 + \varphi)) - \sqrt{r_1^2 - (z - z_{eq} + r_1\cos(\theta_1))} \, dz \tag{38}$$

$$A_{lv} = 2\pi r_1^2 \left[\begin{array}{l} (\cos(\theta_1) + \cos(\theta_1 + \varphi))(\sin(\varphi) + \sin(\theta_1 + \varphi)) + \dfrac{\theta_1 + \theta_2 + \varphi}{2} \\ -\dfrac{1}{4}\sin(2\theta_1 + 2\varphi) - \dfrac{1}{4}\sin(2\theta_2) \end{array} \right] \tag{39}$$

The Capillary force and adhesion energy is follows

$$F_{cap}^*(z_{eq}) = \eta \int_{-\infty}^{\infty} f_c(z)\phi(z) dz \tag{40}$$

$$E_{cap}^*(z_{eq}) = \eta \int_{-\infty}^{\infty} e_c(z)\phi(z) dz \tag{41}$$

F_{cap}^* and E_{cap}^* have values different from zero only when the meniscus is stable. The meniscus is considered instable when

$$r_1\sin(\theta_1 + \varphi) + R\sin(\varphi) \leq r_1 \tag{42}$$

Van der Waals interaction

The derivation of Van der Waals interaction energy of sphere above a half space without the existence of liquid meniscus can be found in [18]. In the current analysis, Van der Waals interaction energies and forces have been derived for the cases of sphere indenting half space without the existence of liquid meniscus, A sphere above half space with existence of liquid meniscus and a sphere indenting a half space with the existence of liquid meniscus.

$$
e_v(z) = \begin{cases}
\dfrac{(A_{ha}-A_{hl})R}{6(y_c+D)}\left[\dfrac{2y_c+D}{y_c+D}+\dfrac{A_{hl}(y_c+D)}{(A_{ha}-A_{hl})D}\right] & z \leq z_{eq}-d_o, \varphi \geq 0 \\[4mm]
\dfrac{(A_{ha}-A_{hl})R}{6(y_c+D)}\left[\dfrac{2y_c+D}{y_c+D}+\dfrac{A_{hl}(y_c+D)(2d_o-D)}{(A_{ha}-A_{hl})d_o^2}\right] & z \geq z_{eq}-d_o, \varphi \geq 0 \\[4mm]
\dfrac{A_{ha}R}{6D} & z \leq z_{eq}-d_o, \varphi = 0 \\[4mm]
\dfrac{A_{ha}R}{6d_o} & z \leq z_{eq}-d_o, \varphi = 0
\end{cases}
\tag{43}
$$

$$
f_v(z) = \begin{cases}
\dfrac{(A_{ha}-A_{hl})R}{6(y_c+D)^2}\left[\dfrac{3y_c+D}{y_c+D}+\dfrac{A_{hl}(y_c+D)^2}{(A_{ha}-A_{hl})D}\right] & z \leq z_{eq}-d_o, \varphi \geq 0 \\[4mm]
\dfrac{(A_{ha}-A_{hl})R}{6(y_c+D)^2}\left[\dfrac{3y_c+D}{y_c+D}+\dfrac{A_{hl}(y_c+D)^2(3d_o-D)}{(A_{ha}-A_{hl})d_o^2}\right] & z \geq z_{eq}-d_o, \varphi \geq 0 \\[4mm]
\dfrac{A_{ha}R}{6D^2} & z \leq z_{eq}-d_o, \varphi = 0 \\[4mm]
\dfrac{A_{ha}R}{6d_o^2} & z \leq z_{eq}-d_o, \varphi = 0
\end{cases}
\tag{44}
$$

Where

$$ y_c = r_1\left(\cos(\theta_1 + \varphi) + \cos(\theta_2)\right) - D \tag{45} $$

$$ D = z_{eq} - D \tag{46} $$

d_o is the cutoff distance of the attractive Van der Waals interaction $d_o = .2$ nm

A_{ha} is the Hamaker media of the materials of the sphere and the half space interaction in air.

A_{hw} is the Hamaker media of the materials of the sphere and the half space interaction in water.

Hamaker constant can be found using Lifshitz theory and the combining relation [19]

$$A_{131} = \frac{3}{4}kT\left(\frac{\varepsilon_1 - \varepsilon_3}{\varepsilon_1 + \varepsilon_3}\right)^2 + \frac{3h\nu_e}{16\sqrt{2}}\frac{\left(n_1^2 - n_3^2\right)^2}{\left(n_1^2 + n_3^2\right)^{3/2}} \tag{47}$$

A_{131} is Hamaker constant of two media of material 1 interacting in medium of material 3, ε_1 is the dielectric constant of material 1, ε_3 is the dielectric constant of the separating media, n_1 is the index of refraction of material 1, n_3 is the index of refraction of material 3, k is the Boltzmann's constant, T is the temperature, h is Blanck's constant, ν_e is the Plasma frequency typically equal to $3e^{15}$ Hz [4]. The values of dielectric constant and index of refraction are shown in table 4-1.

Material	ε	n
air	1	1
Water [4]	80	1.333
Silicon	11.8	3.49
HF	83.6	1.1574
Si_3N_4	4.2	1.11
SiO_2	4.41	1.47

Table 4-1

Table 4-2 shows values of Hamaker constant for different material. Hamaker constants in table 2 can be found in the literature as indicated by the reference number. Also, Equation 47 is used to calculate Hamaker constant when no reference is cited. Hamaker constants in table 3 are found by considering that the energy of adhesion is determined by the properties of the adsorbed film even when it is only monolayer thick[19].

$A_{Si\,HF\,Si}$	625 zJ	$A_{SiO_2\,water\,Si_3N_4}$	19 zJ [20]
$A_{HF\,water\,HF}$	15.9 zJ	$A_{FDTS\,air\,FDTS}$	50 zJ [21]
$A_{Si\,SiO_2\,Si}$	487.75 zJ	$A_{FDTS\,water\,FDTS}$	<4.6 zJ [22]
$A_{SiO_2\,air\,Si_3N_4}$	103.8 zJ [20]	$A_{SiO_2\,water\,SiO_2}$	4.3 zJ [23]
$A_{octadecene\,air\,octadecene}$	50 zJ [19]	$A_{octadecene\,water\,octadecene}$	5 zJ [19]
$A_{OTS\,air\,OTS}$	190 zJ [24]	$A_{Si\,air\,Si}$	690.71 zJ
A_{water}	37 zJ [19]	$A_{SiO_2\,air\,SiO_2}$	64.4 zJ

Table 4-2

Numerical Solution

There are two solution domain, the first domain is the heights of the asperities peak z and the second is the location of the equilibrium plane z_{eq}. To achieve grid independent solution, The node numbers on the z-domain is selected to be 2000 nodes over the range $(-R \leq z \leq 10R)$. The applied forces applied on the rough surface are calculated as in Eqns. (11,25,31). The numerical solution is implanted by solving for the static equilibrium using secant method with a convergence criterion of $\delta \leq 10^{-8}$. The solution procedure is required two initial guesses of z_{eq} in order to start the process of the root finding according the following equation.

$$z_{eq}^{i+1} = z_{eq}^{i} - \frac{G(z_{eq}^{i})(z_{eq}^{i} - z_{eq}^{i-1})}{G(z_{eq}^{i}) - G(z_{eq}^{i-1})} \tag{47}$$

Where:

$$G(z_{eq}) = F_e^{*}(z_{eq}) - F_{cap}^{*}(z_{eq}) - F_{van}^{*}(z_{eq}) \tag{48}$$

$$\delta = \frac{z_{eq}^{i+1} - z_{eq}^{i}}{z_{eq}^{i}} \tag{49}$$

Kelvin's equation Eqn. (30) is needed to be solved in order to find filling angle of the liquid meniscus and the capillary forces. Since Eqn. (30) has multiple roots, it was solved using bisection method. The interesting solution domain of Eqn. (4) is

$0 \le \varphi \le \frac{\pi}{2}$. After solving Kelvin's equation, the applied forces are calculated and then a numerical solution of the static equilibrium plane is found. After that, the energy of adhesion is found.

$$E^*_{adh} = E^*_{cap} + E^*_{van} \tag{50}$$

Results and Discussion

The literatures contain a plenty of papers that study the energy of adhesion experimentally, i.e. (21-24). The experimental method of measuring the energy of adhesion was developed by [26-27]. Table 4-3 shows a comparison between the energy of adhesion as measured experimentally in the literature, dry stiction model of Harriri et. al. [29] and the value of the energy of adhesion from the current model. As a validation for the code the case of oxide coating polysilicon with zero contact angles and 95% relative humidity has been done. In this case, the current model estimated the adhesion energy to be 79.4 mJ/m². The adhesion energy of two smooth surface which have zero contact angles is $2\gamma = 150.4$ mJ/m².

Coating	θ_1 (deg)	θ_2 (deg)	σ_1 nm	σ_2 nm	σ nm	A_{ha} zJ	A_{hl} zJ	E_{adh} Exp $\mu J/m^2$	E_{adh} Ref. 29 $\mu J/m^2$	E_{adh} theo $\mu J/m$
OTS [22]	112	112	12	12	16.97	190	59.3	3	.068	.08
OTS[22]	112	112	3	3	4.24	190	59.3	30	5.44	6.59
FDTS [22]	115	115	12	12	16.97	50	4	2.1	.46	.014
FDTS [22]	115	115	3	3	4.24	50	4	8	6.44	1.36
Octadecene[24]	104	104	5.9	5.9	8.3	50	5	4	1.89	.33
Oxide [23]	0	0	2*	2	2.8	64.43	4.3	8000	------	562.3

* Ref. [23] do not contain the value of the surface roughness of the oxide layer, the value taken from ref. [25].

$A_{ha} = A_{coating\ air\ coating}$ $A_{hl} = A_{coating\ water\ coating}$

Table 4-3

The reason why the current model adhesion energy is less than the theoretical one is due to the surface rough. The liquid can't cover all the surfaces because of the different asperities heights which will result in the existence of liquid/vapor interfaces. The existence of liquid/vapor interfaces decreases the adhesion energy as can be predicted from Eqn (35).

Figures 4-16 and 4-17 show the adhesion energy and the adhesion force as a function of the relative humidity and The Hamaker constant across the air. Other parameters have the following values $A_{hl} = 50$ zJ, $\sigma = 5$ nm, $\beta^* = 500$ nm, $\theta_1 = \theta_2 = 30^\circ$, $V_l = 18.86e^{-6}\ m^3/mol$, $\gamma_{lv} = 75.2e^{-3}\ N/m$, T $= 300$ K, $E^* = 163$ GPa, and H $= 10$ GPa. As seen in Figs(16-17), The Adhesion energy and force decrease as the relative humidity increases in the range of low relative humidity. Since Hamaker constant across liquid is less than Hamaker constant across air, the formation of small volume liquid menisci will result in decreasing the adhesion energy and the adhesion force. At high relative humidity range, Capillary effect dominates other effects. Therefore, the adhesion energy and adhesion force increase as the relative humidity increases in high humidity range.
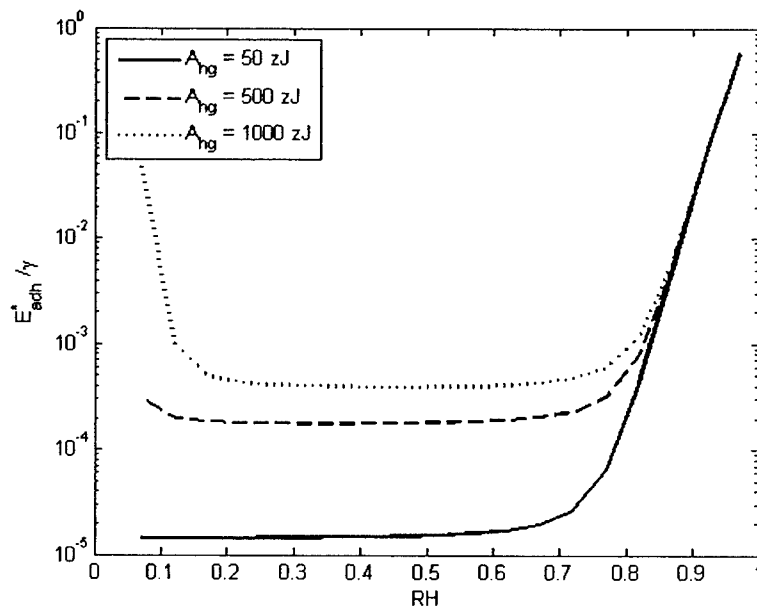

Fig. 4-16. Adhesion energy versus relative humidity for different values of Hamaker constant across air
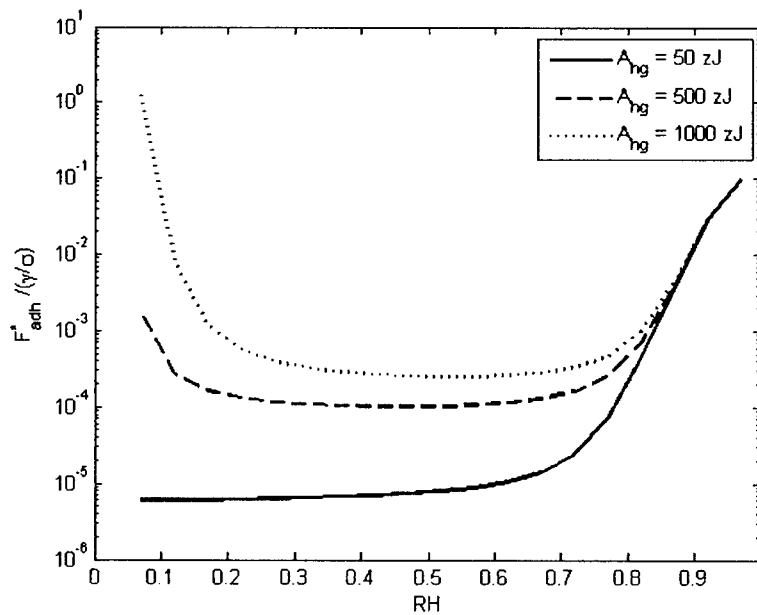
Fig. 4-17. Adhesion force versus relative humidity for different values Hamaker constant across air

Figures 4-18 and 4-19 show the adhesion energy and the adhesion force as a function of the surface roughness and The modulus of elasticity. Other parameters have the following values A_{ha}=500 zJ, A_{hl} = 50 zJ, RH = 70%, β^*=500 nm, $\theta_1=\theta_2$=30°, $V_l = 18.86e^{-6} m^3/mol$, $\gamma_{lv} = 75.2e^{-3} N/m$, T = 300 K and H = 10 GPa. As seen in Figs(18-19), The adhesion energy and the adhesion force decrease as the surface roughness increases. As the surface roughness increases the z-range of the surface heights will increase and so the liquid can't perfectly wet the rough surface even for the case of zero contact angle which tends to decrease the adhesion energy and force of the capillary action. Also, the wide z-range will result in decreasing the effect of Van der Waals interaction. Figs(18-19) also show the effect of the modulus of elasticity on adhesion. As the modulus of elasticity increases the adhesion energy and the adhesion force decrease. The decrease in the adhesion energy and force with increasing modulus of elasticity is due to the increase in the rigidity of the surface. As the rigidity increases, the equilibrium distance between the two surfaces increases due to the increase in the structural forces. Therefore, the adhesion energy and force decrease as the modulus of elasticity increases.
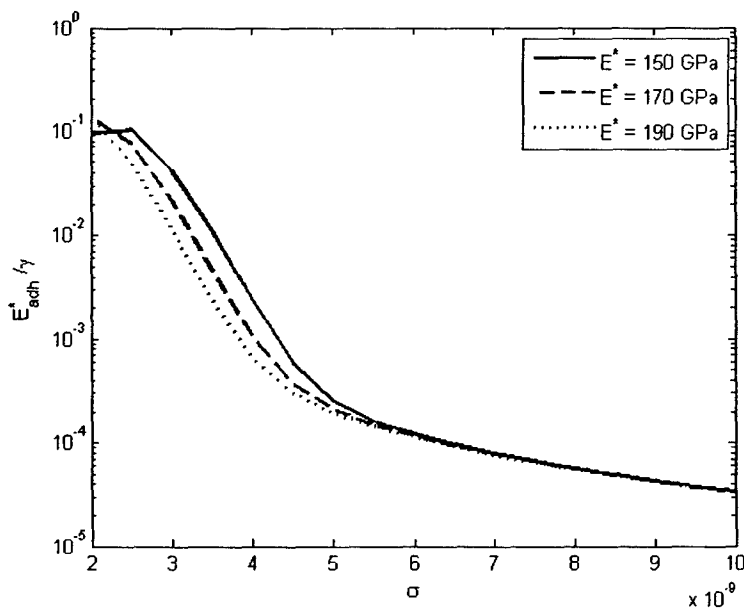
Fig. 4-18. Adhesion energy versus surface roughness for different values of modulus of elasticity
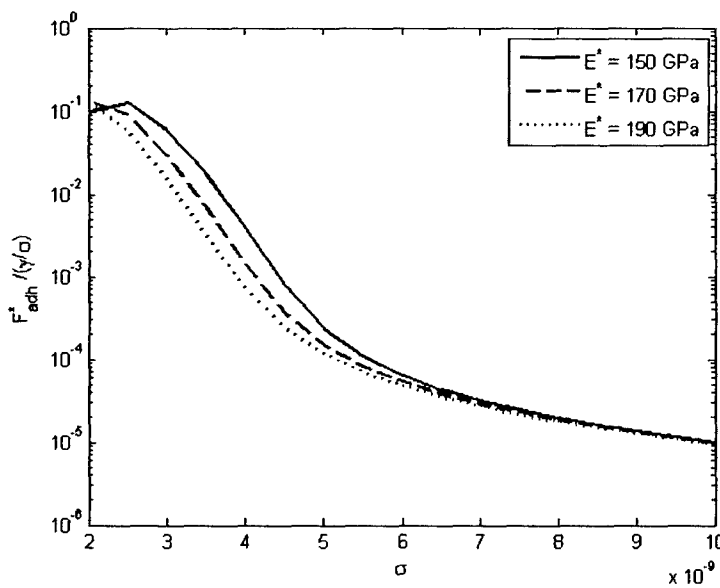

Fig. 4-19. Adhesion force versus surface roughness for different values of modulus of elasticity

Figures 4-20 and 4-21 show the adhesion energy and the adhesion force as a function of the surface roughness and The hardness. Other parameters have the following values A_{ha}=500 zJ, A_{hl} = 50 zJ, RH = 70%, β^*=500 nm, $\theta_1=\theta_2$=30°, $V_l = 18.86e^{-6}\ m^3/mol$, $\gamma_{lv} = 75.2e^{-3}\ N/m$, T = 300 K and E^*= 163 GPa. As seen in Figs (4-20~4-21), as the hardness increases the adhesion energy and the adhesion force increase. This behavior is unpredictable, since as the hardness increases the structural forces increase which will result in decreasing the adhesion energy and the adhesion force. Here, we report this result as it is since we can't know what causes the unpredictable behavior of the adhesion energy and force as function of the hardness.
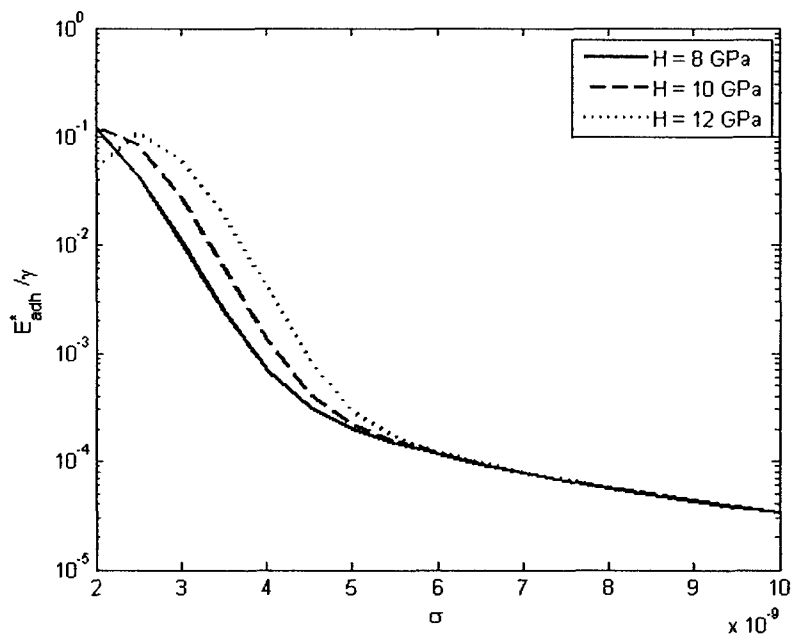

Fig. 4-20. Adhesion energy versus surface roughness for different values of the hardness
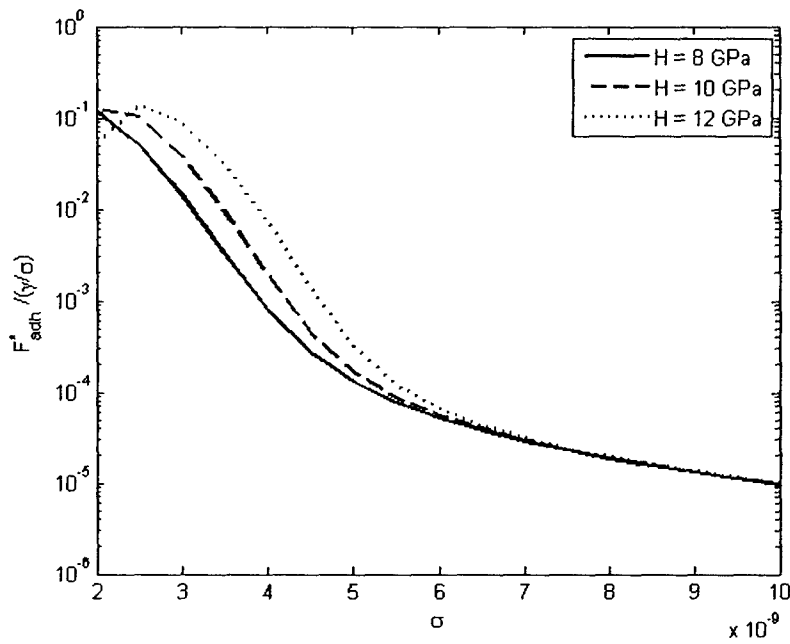
Fig. 4-21. Adhesion force versus surface roughness for different values of the hardness

Figures 4-20 and 4-21 show the adhesion energy and the adhesion force as a function of the contact angles. Other parameters have the following values A_{ha} =500 zJ, A_{hl} = 50 zJ, RH = 70%, β^*=500 nm, σ = 5 nm, $V_l = 18.86e^{-6} \, m^3/mol$, $\gamma_{lv} = 75.2e^{-3} \, N/m$, T = 300 K, E^*= 163 GPa and H = 10 GPa. As seen in Figs(4-20~4-21), as the contact angles decrease the adhesion energy and force increase due to the increase in the wetted area of the surfaces. The adhesion energy and force decrease toward an asymptotic value as the contact angles increase. As the contact angles become larger than $\frac{\pi}{2}$ the surfaces become hydrophobic which will result in an imperfect wetting of the surfaces. Also, as the contact angles the liquid menisci become instable. Consequently, At high contact angles, Only Van der Waals interaction energy and force are exist. Therefore, as the contact angles increase the energy of adhesion and force will decrease asymptotically toward the values of Van der Waals interaction energy and force.
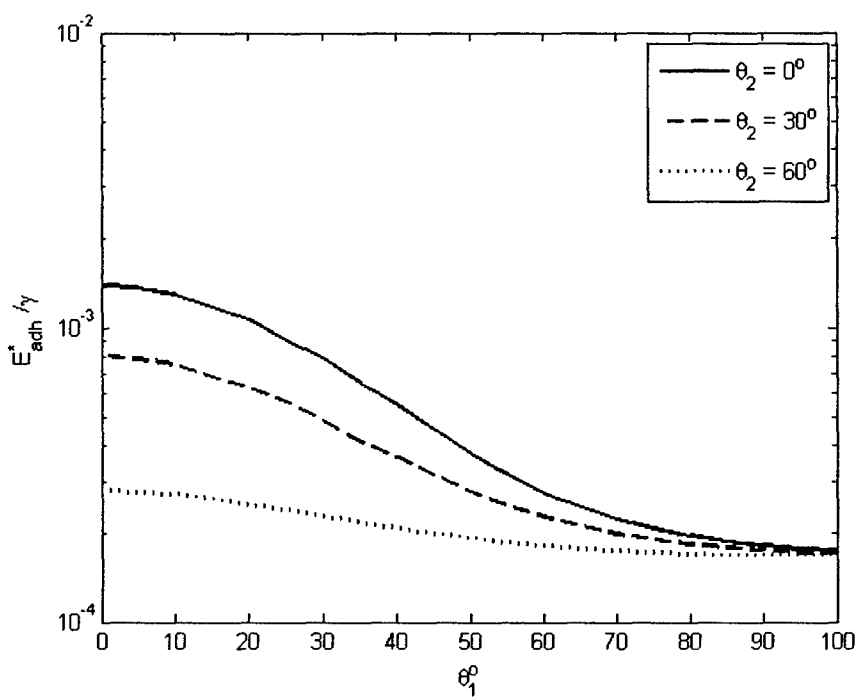
**Fig. 4-22.** Adhesion energy versus contact angles
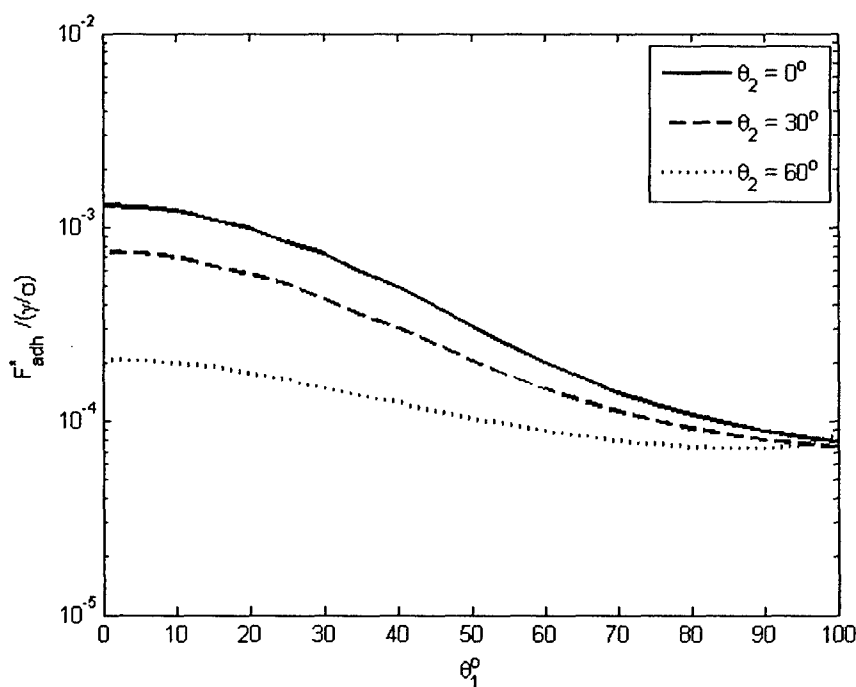
Fig. 4-23. Adhesion force versus contact angles

Conclusions

1. G-W surface roughness model is an efficient model that can be used to model the stiction phenomenon.

2. The advantages of G-W model is that it gives the possibility for a realistic modeling of the capillary condensation and its interaction energies and forces. Also, it makes it possible to study the effect of the liquid meniscus on Van der Waals interaction energies.

3. The Van der Waals interaction is the dominant cause of stiction at low relative humidity while capillary condensation is the dominant cause of stiction at high relative humidity.

4. At low relative humidity the adhesion energy and force decrease as the relative humidity increase due to the formation of liquid menisci.

5. As the Surface roughness increases the adhesion energy and the adhesion force decrease.

6. As the contact angles increase the adhesion energy and the adhesion force decrease.

7. As the modulus of elasticity increases the adhesion energy and the adhesion force decrease.

8.

References

[1] C. H. Mastrangelo and C. H. Hsu, Proc. IEEE solid-state Sensors and Actuator Workshop Hilton Head, 208,1992.

[2] M. P. de Boer, P. J. Clews, B. K. Smith and T. A. Michalske, Mat. Res. Soc. Symp. Proc., 518, 131-136,1998.

[3] Y. Yee, M. Park and K Chun, J. Microelectromechanical Systems, 7, 339, 1998.

[4] R. W. Johnstone and M Parameswaran, J. Micromechanics ans Microengineering, 12, 855, 2002.

[5] F. Yang, J. Micromechanics and Microengineering, 14, 263, 2004.

[6] M. P. de Boer, J. A. Knapp, T. M. Mayer and T. A. Michalske, SPIE/EOS conference on Microsystems Metrology and Inspection, Munich June 15, 1999.

[7] W. M. van Spengen, R. Puers and I. De Wolf, J. Micromechanics and Microengineering, 12, 702, 2002.

[8] W. M. van Spengen, R. Puers and I. De Wolf, J. Adhesion Sci. and Technology, 17, 563, 2003.

[9] O. Raccurt, F. Tradif, F. A. d'Avitaya and T. Vareine, J. Micromechanics and Microengineering,14, 1083, 2004.

[10] B.N.J Persson, "Contact Mechanics for Randomly Rough Surfaces", Sur. Sci, reports, Vol. 61, pp. 201-267, 2006.

[11] J. A. Greenwood and J. B. Williamson, "Contact of Nominally Flat Surfaces", Proc. Roy. Soc. London, Vol. 295, no. 1442, pp. 300-319, 1966.

[12] D. J. Whitehouse and J. F. Archard, "The Properties of Random Surfaces of Significance in their Contact", Proc. Roy. Soc. London, Vol. 316, No. 1524, pp. 97-121, 1970.

[13] McCool

[14] K. L. Johnson, "Contact Mechanics", Cambridge University press, New York, 1985.

[15] L. Kogut and I. Estion, "Elastic-Plastic Contact Analysis of a Sphere and a Rigid Flat", J. App. Mech., Vol. 69, pp. 657-662, 2002.

[16] F. M. Orr and L. E. Scriven, "Pendular Rings between Solids: Meniscus Properties and Capillary Force", J. Fluid Mech., Vol. 67, part 4, pp. 723-742, 1975.

[17] J. S. Rowlinson and B. Widom, "Molecular Theory of Vapillarity", Oxford University Press, New York, 1982.

[18] A. W. Adamson, "Physical Chemistry of Surfaces", 3rd edition , Wiley, New York and London, 1976.

[19] J. N. Israelachvili, "Intermolecular and Surface Forces", 2nd edition, Academic press, London, 1991.

[20] X. Xiao and L. Qian, "Investigation of Humidity-Dependent Capillary Force", Langmuir, Vol. 16, pp. 8153-8158, 2000.

[21] F. W. Delrio, M. P. De Boer, E. D. Reedy Jr and P. J. Clews, " The Role of Van der Waals Forces in Adhesion of Micromachined Surfaces", Nature Material, Vol. 4, pp. 629-634, 2005.

[22] I. M. Tidswell, T. A. Rabedeau and P. S. Pershan, "Wetting Films on Chemically Modified Surfaces: AN X-Ray Study", Phys. Rev. B, Vol. 15, pp. 10896-10879, 1991.

[23] J. M. Fernandez-Varea, R. Garcia-Molina, "Hamaker Constants of Systems Involving Water Obtained from a Dielectric Function That Fulfills the fSum Rule", J. Colloids Interface Sci., Vol. 231, pp. 394-397, 2000.

[24] R Seemann, S. Herminghaus and K. Jacobs, "Gaining Control of Pattern Formation of Dewetting Liquid Films", J. Phys.: cond. Matt. Vol. 13, pp. 4025-4938, 2000.

[25] M. R. Houston, R. T. Howe, R. Maboudian, "Effect of Hydrogen Termination on the Work of Adhesion Between Rough Polycrystaline Surfaces", J. Appl. Phys., Vol. 81, No. 8, pp. 3474-3483, 1997.

[26] U. Srinivasan, M. R. Houston, R. T. Howe and R. Maboudian, "Alkyltrichlorosilane-Based Self-Assembled Monolayer Films for Stiction Reduction in Silicon Micromachines", J. Microelectromechanical Sys, Vol. 7, No. 2, 1998.

[27] W. R. Ashurst, Ch. Yau, C. Carraro, Ch. Lee, G. J. Kluth, R. T. Howe and R. Maboudian, "Alkene Based Monolayer Films as Anti-Stiction Coating for Polysilicon MEMS", Sensors and Actuators A, Vol. 91, pp. 239-248, 2001.

[28] W. R. Ashurt, M. P. de Boer, C. Cararro and R Maboudian, "An investigation of Sidewall Adhesion in MEMS", Appl. Surf. Sci., Vol. 212-213, pp. 735-741, 2003.

[29] A Hariri, J. W. Zu and R. Ben Mrad, "Modeling of dry stiction in micro electro-mechanical systems (MEMS)", J. Micromech. Microeng., Vol. 16, pp. 1195-1206, 2006.

Appendix

Matlab scripts that are used to study the in-use stiction

```
function
[FC1,FE1,FV1,EE1,EC1,EV1]=rough(gama,th1,th2,Ah1,Ahg,est,H,seg1,beta1,R
H,T,V1,n)
% A program for estimating the stiction force taking into account the
% capiilary condensation
%%%%%%%%%%%%%%%%%%%%%%%%%%%%%%%%%%%
% parameters initiation
%%%%%%%%%%%%%%%%%%%%%%%%%%%%%%%%%%%
%Paramters difinition
beta1=beta1/seg1;
R=beta1^2/20;
est=est*seg1/gama;
do=-.17e-9/seg1;
```

```matlab
H = H/gama*seg1;   % hardness
K = .545+.41*.25; % related to poisson ration v=.25
KK=4/3*est/(1-.25^2)/pi^2;
EE=est/(1-.25^2)/2;
zhc=(pi*K*H/2/EE)^2*R;
seg=.9;
Ahg=Ahg/gama/seg1^2;
Ahl=Ahl/gama/seg1^2;
zm=.47; % mean of beak distribution
% R=beta; % mean radius of the curvature of the surface
eigta=41.26e-3/R/seg;
Rg=8.314; % Ideal gas constant
rho=exp(-0.23)
%%% descritizing the z-dimension
% the domain between zhc and do
dz1=(0.1*R+do)/n;
dz2=(110*zhc-do)/n;
dz3=(R-110*zhc)/n;
z(1)=-.1*R;
for i=2:n
    z(i)=z(i-1)+dz1;
end
z(n+1)=do;
for i=n+2:2*n
    z(i)=z(i-1)+dz2;
end
z(2*n+1)=110*zhc;
for i=2*n+2:3*n
    z(i)=z(i-1)+dz3;
end
% break
y=-5*R:(15*R+R)/10/n:15*R;
% break
% z=-R:dz:10*R; % descritization in the z direction
x=z;
dz=0;
zeq1=0;
zeq0=0;
%      zeq0=200e-9;
%      zeq1=zeq0+dz;
%      err=100;
%      kkk=1;
%      k=0;
%%%%%%%%%


%%%%%%%%%%%%%%%%%%%%%%%%%%%%%%%%%%%%%%
%%% initiation
W(1:length(x))=0;
fh(1:length(x))=0;
e(1:length(x))=0;
f(1:length(x))=0;
ps2(1:length(x))=0;
Fc(1:length(z))=0;
Ec(1:length(z))=0;
Fe(1:length(z))=0;
```

```matlab
fc0(1:length(z))=0;
fc1(1:length(z))=0;
%%%%%%%%%%%%%%%%%%%%%%%%%%%%%%%%%%%%%%
% building the probability distribution function
for m=1:length(z)
    phi11(m)=(1/sqrt(2*pi)*exp(-1*(z(m)-zm)^2/2/seg^2))/seg;
%      phi11(m)=(1/sqrt(2*pi)*exp(-1*(z(m)-
zm)^2/2/seg^2))/seg*(1+erf((z(m)-zm)/sqrt(2)/seg))^2/4;
phi11(m)=(1/sqrt(2*pi)*exp(-1*(z(m))^2/2))*(1+erf((z(m)*sqrt((1-
rho)/(1+rho)))/sqrt(2)))^2/4;
end
% break
%%%%%%%%%%%%%%%%%%%%%%%%%%%%%%%%%%%%%%%%
%%%%% Solving for the filling angle
% ps0=fcapz(x,zeq0,R,th1,th2,T,RH,Rg,Vl,gama,seg1);
%%%%%%%%%%%%%%%%%%%%%%%%%%%%%%%%%%%%%%%%%%%%
%%%%%%% finding the elastic force
%      [fe0,ee0] = Felastic(z,zeq0,R,est,seg1,gama);
[fe,ee,feu,zhc] = Felastic(z,zeq1,R,est,H,seg1,gama);
ps1=fcapz(x,zeq1,R,th1,th2,T,RH,Rg,Vl,gama,seg1,zhc,dz);
%%%
%%%%%% finding the capilary force
[fc,ec]=fcapx(x,ps1,z,zeq1,R,gama,th1,th2,RH,Vl,Rg,T,seg1,zhc,dz);
%%%%%%%%%%finding Van der Waal forces
[fv,ev]=fvdw(Ahl,Ahg,z,zeq1,R,x,ps1,th1,th2,seg1,gama,zhc,dz);
%%%%%%%%%%%%%%%%%%%%%%%%%%%%%%%%%%%%%%%%%%%
zeq0=.01;
kkk=1;
fe1=fe;
fc1=fc;
fv1=fv;
ev1=ev;
ec1=ec;
ee1=ee;
% break
for m=1:length(z)
    phi11(m)=(1/sqrt(2*pi)*exp(-1*(z(m)-zm)^2/2/seg^2))/seg;
%      phi11(m)=(1/sqrt(2*pi)*exp(-1*(z(m)-
zm)^2/2/seg^2))/seg*(1+erf((z(m)-zm)/sqrt(2)/seg))^2/4;
phi11(m)=(1/sqrt(2*pi)*exp(-1*(z(m))^2/2))*(1+erf((z(m)*sqrt((1-
rho)/(1+rho)))/sqrt(2)))^2/4;
end
err=100;
% for k=2:length(y)
k=0;
while err > 1e-10
    k=k+1;
z1=z+zeq1;
for m=1:length(z)
    phi1(m)=(1/sqrt(2*pi)*exp(-1*(z(m)-zm)^2/2/seg^2))/seg;
%      phi11(m)=(1/sqrt(2*pi)*exp(-1*(z(m)-
zm)^2/2/seg^2))/seg*(1+erf((z(m)-zm)/sqrt(2)/seg))^2/4;
phi1(m)=(1/sqrt(2*pi)*exp(-1*(z1(m))^2/2))*(1+erf((z1(m)*sqrt((1-
rho)/(1+rho)))/sqrt(2)))^2/4;
end
FC1=integ(phi1.*fc1*eigta,z1);
FE1=integ(phi1.*fe1*eigta,z1);
```

```matlab
FV1=integ(phi1.*fv1*eigta,z1);
%%%%%%%%%%%%%%%%%%%%%%%%%%%%%%%%
z1=z+zeq0;
for m=1:length(z)
    phi1(m)=(1/sqrt(2*pi)*exp(-1*(z(m)-zm)^2/2/seg^2))/seg;
%      phi11(m)=(1/sqrt(2*pi)*exp(-1*(z(m)-
zm)^2/2/seg^2))/seg*(1+erf((z(m)-zm)/sqrt(2)/seg))^2/4;
phi1(m)=(1/sqrt(2*pi)*exp(-1*(z1(m))^2/2))*(1+erf((z1(m)*sqrt((1-
rho)/(1+rho)))/sqrt(2)))^2/4;
end
FC0=integ(phi1.*fc1*eigta,z1);
FE0=integ(phi1.*fe1*eigta,z1);
FV0=integ(phi1.*fv1*eigta,z1);
%%%%%%%%%%%%%%%%%%%%%%%%%%%%%%%%%%%%
G=integ(phi1.*ec1,z1)*eigta+integ(phi1.*ev1,z1)*eigta+integ(phi1.*ee1,z
1)*eigta;
%%%%%%%%%%%%%%%%%%%%%%%%%%%%%%%%%%%%
F0=FE0-FV0-FC0;
F1=FE1-FV1-FC1;
%%%%
FF0(k)=FE1;
FF2(k)=FC1;
FF1(k)=F1;
FF3(k)=FV1;
EE1(k)=integ(phi1.*ec1,z1)*eigta;
EE2(k)=integ(phi1.*ev1,z1)*eigta;
EE3(k)=integ(phi1.*ee1,z1)*eigta;
GG(k)=G;
zz(kkk)=zeq0;
kkk=kkk+1;
%%%%%%%%%%%%%%%%%%%%%%%%%%%%%%%%%%%%
if F1 ~= F0
zeq=zeq1-F1*(zeq1-zeq0)/(F1-F0);
else
    zeq=.75*zeq1
end
err=abs((zeq-zeq1)/zeq)*100
zeq0=zeq1;
zeq1=zeq;
%          zeq1=zeq;

end
% inn=find(FF1 < 0);
% zeq1=y(inn(length(1)));
% k=inn(length(1));
z1=z+zeq1;
for m=1:length(z)
    phi1(m)=(1/sqrt(2*pi)*exp(-1*(z(m)-zm)^2/2/seg^2))/seg;
%      phi11(m)=(1/sqrt(2*pi)*exp(-1*(z(m)-
zm)^2/2/seg^2))/seg*(1+erf((z(m)-zm)/sqrt(2)/seg))^2/4;
phi1(m)=(1/sqrt(2*pi)*exp(-1*(z1(m))^2/2))*(1+erf((z1(m)*sqrt((1-
rho)/(1+rho)))/sqrt(2)))^2/4;
end
FC1=integ(phi1.*fc1,z1)*eigta;
FE1=integ(phi1.*fe1,z1)*eigta;
FV1=integ(phi1.*fv1,z1)*eigta;
G=integ(phi1.*ec1,z1)*eigta+integ(phi1.*ev1,z1)*eigta;
```

```
EC1=-1*integ(phi1.*ec1,z1)*eigta;
EV1=-1*integ(phi1.*ev1,z1)*eigta;
EE1=integ(phi1.*ee1,z1)*eigta;
```

```
function ps2=fcapz(x,zeq,R,th1,th2,T,RH,Rg,Vl,gama,seg,zhc,dz)
ps2(1:length(x))=0;
%%%%%%%%%%%%%%%%%%%%%%%%%%%%%
xc=0;
for i=1:length(x)
    err=100;
    h=zeq-x(i);
if h <= -R
    h=-R;
end
    if h <= 0
        xa=acos(1+h/R);
    else
        xa=0;
    end
    xb=pi/2+.01;
    EPSILON = 1e-8;
    phii0=xa;
    fa = ((-1*(cos(th2)+cos(th1+phii0))/((1-
cos(phii0))+h/R)+1/sin(phii0)))-seg*R*Rg*T*log(RH)/gama/Vl;
    phii0=xb;
    fb = ((-1*(cos(th2)+cos(th1+phii0))/((1-
cos(phii0))+h/R)+1/sin(phii0)))-seg*R*Rg*T*log(RH)/gama/Vl;
    iter=0;
    while ( err > EPSILON )
        iter=iter+1;
        xc = abs( xa + xb ) / 2;
        phii0=xc;
        fc = ((-1*(cos(th2)+cos(th1+phii0))/((1-
cos(phii0))+h/R)+1/sin(phii0)))-seg*R*Rg*T*log(RH)/gama/Vl;

        err= abs ( fc );
        if ( fc == eps )
            xa = xc;
        elseif ( sign(fb) * sign(fc) <= 0 )
            xa = xc;
            fa = fc;
        else
            xb = xc;
            fb = fc;
        end
        if iter > 200
            err=eps;
            if h > 0
                xc=0;
            else
xc=0;
            end
        end
    end
    if xc > pi/2
```

```matlab
        xc=pi/2;
    end
    ps2(i)=xc;
end
```

```matlab
function [fe,ee,feu,zhc] = Felastic(z,zeq,R,est,H,seg,gama)
fe(1:length(z))=0;
ee(1:length(z))=0;
K = .545+.41*.25; % related to poisson ration v=.3
KK=4/3*est/(1-.25^2)/pi^2;
EE=est/(1-.25^2);
zhc=(pi*K*H/2/EE)^2*R;
for k=1:length(z)
    zh=z(k)-zeq;
    if zh > 0
        if zh <=  zhc
            fe(k)=4/3*EE*sqrt(R)*zh^1.5;
feu(k)=2*R*zh*pi*H;
ee(k)=.5*zh*(fe(k)-feu(k));
        elseif zh > zhc & zh <= 6*zhc
            fe(k)=1.03*(zh/zhc)^1.425*4/3*EE*sqrt(R)*zhc^1.5;
%                      ee(k)=1/2*fe(k)*zh;
feu(k)=2*R*zh*pi*H;
ee(k)=.5*zh*(fe(k)-feu(k));
        elseif zh > 6*zhc & zh <= 110*zhc
            %                fe(k)=2*pi*zh*R*H;
            fe(k)=1.4*(zh/zhc)^1.263*4/3*EE*sqrt(R)*zhc^1.5;
            %
ee(k)=2/5*(4/3*EE*sqrt(R)*zhc^1.5)^(5/3)/KK^(2/3)/R^(1/3);
%            ee(k)=1/2*fe(k)*zh;
feu(k)=2*R*zh*pi*H;
ee(k)=.5*zh*(fe(k)-feu(k));

        elseif zh > 110*zhc & zh <= R
                       fe(k)=3/K*(zh/zhc)^1*4/3*EE*sqrt(R)*zhc^1.5;
            feu(k)=2*R*zh*pi*H;
            ee(k)=.5*zh*(fe(k)-feu(k));
%            ee(k)=1/2*fe(k)*zh-1/2*fe(k)*(zh-110*zhc);
            %
ee(k)=2/5*(4/3*EE*sqrt(R)*zhc^1.5)^(5/3)/KK^(2/3)/R^(1/3);
        elseif zh > 110*zhc & zh >= R
    feu(k)=2*R*zh*pi*H;
            fe(k)=3/K*(zh/zhc)^1*4/3*EE*sqrt(R)*zhc^1.5;
            ee(k)=.5*zh*(fe(k)-feu(k));
%             fe(k)=pi*R^2*H;
%             ee(k)=pi*H*(R^3/3-1/3*(R-zh)^3-R^2*zh);
% ee(k)=1/2*fe(k)*zh-1/2*fe(k)*(zh-110*zhc);
        end
    end
end
```

```matlab
function [f,e]=fcapx(z,ps2,x,zeq,R,gama,th1,th2,RH,Vl,Rg,T,seg,zhc,dz)
W(1:length(x))=0;
```

```
fh(1:length(x))=0;
e(1:length(x))=0;
f(1:length(x))=0;
% Finding the capillary force and surface energy as a function of x
%%%%%%%%%%%%%%%%%%%%%%%%%%%%
%%%%%%%%%%%%%%%%%%%%%%%%%%%%%%%%%%%%%%
for k=1:length(x)

    h=zeq-x(k);
    if h <= -R
        h=-R;
    end
    phi=ps2(k);
    %%%%
    %%%%%%%%%%%%%%%%%%%%
    r1=(((R*(1-cos(phi))+h)/(cos(th1+phi)+cos(th2))));
    if phi ~= 0
        fh(k)=2*pi*R*sin(phi)*sin(phi+th1)-(-
1*(cos(th2)+cos(th1+phi))/(R-
R*cos(phi)+h)+sin(th1+phi)/sin(phi)/R)*pi*(R*sin(phi))^2;
        Esls=-1 *pi*cos(th2)*(R*sin(phi)+r1*sin(th1+phi)-
r1*sin(th2))^2;
        Esla=-1*2*pi*R^2*(1-cos(phi))*cos(th1);
        if h < 0
            c=sqrt(R^2-(R+h)^2);
            Esls=Esls+pi*c^2*cos(th2);
            Esla=Esla+pi*2*R*h*-1*cos(th1);

            fh(k)=2*pi*R*sin(phi)*sin(phi+th1)-(-
1*(cos(th2)+cos(th1+phi))/(R-
R*cos(phi)+h)+sin(th1+phi)/sin(phi)/R)*pi*((R*sin(phi))^2-c^2);
        end

Elv=2*pi*((cos(th2)+cos(th1+phi))*(sin(phi)+sin(th1+phi))+(th1+phi+th2)
/2-1/4*sin(2*th1+2*phi)-1/4*sin(2*th2))*r1^2;
        W(k)=Elv+Esls+Esla;
        if h <= -R
            W(k)=W(k-1);
            fh(k)=fh(k-1);
        end
    end
end


f=fh; % force density as function of z
e=W; % energy density as function of z




function [fv,ev]=fvdw(Ahl,Ahg,z,zeq,R,x,ps2,th1,th2,seg,gama,zhc,dz)
do=.17e-9/seg;
fv(1:length(z))=0;
ev(1:length(z))=0;
for i=1:length(z)
    h=zeq-z(i);
if h <= -R
```

```matlab
        h=-R;
end

    D=h;
    phi=ps2(i);

    %%%%
    r1=((((R*(1-cos(phi))+h)/(cos(th1+phi)+cos(th2))))));
    zcc=r1*(cos(phi+th1)+cos(th2))-D;
    if r1 ~= 0  & phi ~= 0 & D ~= 0
        if D >= do
            %
            fv(i)=R*(Ahg-
Ahl)/6/(zcc+D)^2*((3*zcc+D)/(zcc+D)+Ahl*(zcc+D)^2/(Ahg-Ahl)/D^2);
            ev(i)=-1*(Ahg-
Ahl)*R/6/(zcc+D)*((2*zcc+D)/(zcc+D)+Ahl*(zcc+D)/(Ahl-Ahg)/D);
        elseif D < do

            fv(i)=R*(Ahg-
Ahl)/6/(zcc+D)^2*((3*zcc+D)/(zcc+D)+Ahl*(zcc+D)^2*(3*do-2*D)/(Ahg-
Ahl)/D^2);
            ev(i)=-1*(Ahg-Ahl)*R/6/(zcc+D)*((2*zcc+D)/(zcc+D)-
Ahl*(zcc+D)*(2*do+D)/(Ahl-Ahg)/do^2);
        else
            ev(i)=0;
            fv(i)=0;

        end
    end

    if phi == 0 & h >= 0
        fv(i)=Ahg/6*(1/h^2)*R;
        ev(i)=-Ahg/6*(1/h)*R;
    end
    if phi == 0 & h < do
        fv(i)=Ahg/6*(1/(do)^2)*R;
        ev(i)=-Ahg/6*(1/(do))*R;
    end
end
fv=abs(fv);
% plot(fv)
% pause
```

```matlab
function A=integ(F,x)
sum=0;
for i=2:length(x)
    sum=sum+(F(i)+F(i-1))/2*(x(i)-x(i-1));
end
A=sum;
```